



## Funding Note

The industrial research project “Flow Curve JbyF – Standardization of Flow Curve Determination for Joining by Forming” was supervised by the EFB European Research Association for Sheet Metal Working (Europäische Forschungsgesellschaft für Blechverarbeitung e.V.) Hannover and funded through the AIF by the program for “Industrial Research” (IGF) of the Federal Ministry of Economics and Technology Germany as well as the “Agentschap Innoveren & Ondernemen” Belgium.



AGENTSCHAP  
INNOVEREN &  
ONDERNEMEN



Vlaanderen  
is ondernemen



### Persons that contributed to the project:

#### **Fraunhofer Institute for Machine Tools and Forming Technology IWU Dresden (IWU)**

Mathias Jäckel, Sumant Kumar Jaiswal, Christian Kraus, Welf-Guntram Drossel

#### **Katholieke Universiteit Leuven (KUL)**

S. Coppieters, Dimitri Debruyne

#### **Belgisch Instituut voor Lastechniek, Zwijnaarde (BWI)**

N. Vandermeiren

#### **Institute of Engineering, Tokyo University of Agriculture and Technology**

Noa Miyake, Toshihiko Kuwabara

#### **Faurecia Autositze GmbH**

Klaus Unruh

#### **Institute of Forming Technology and Lightweight Components, TU Dortmund**

Heinrich Traphöner, A. Erman Tekkaya

#### **Institute of Forming Technology and Lightweight Components, TU Dortmund**

Heinrich Traphöner, A. Erman Tekkaya

#### **Arts et Metiers Institute of Technology, Université de Lorraine, LCFC, HESAM Université**

Tudor Balan



## Industrial support note

This research project was supported by a German and Belgian industrial user committee which provided materials, joining tools and elements for the experimental investigations, supported the material characterisation. For this, as well as for the constructive discussions during the project meetings, we would like to thank the industrial support group:

### **German**

Audi AG

BMW AG

Eckold GmbH & Co. KG

F&K Werkstoffprüfung und Labor  
GmbH

Henrob GmbH

IMA Dresden

Scale GmbH

Profil Verbindungstechnik GmbH &  
Co. KG

Promess Gesellschaft für  
Montage und Prüfsysteme mbH

Werkzeuggestaltung Schmutzler

Werkzeuggestaltung Ammer

Arnold Umformtechnik GmbH & Co.  
KG

Simufact Engineering

### **Belgium**

Dejond NV

Ocas NV

Plakoni Projects BVBA

Sapa RC profiles NV/SA

Beluma NV/SA

Van Hool



## Abstract

The demands for joining techniques increased significantly in the last decade. Today, structures are highly optimized to meet stringent requirements with respect to a variety of performance metrics such as weight, safety and environmental impact. Given that FE modules dedicated to simulating joining by forming process reached a sufficiently high level of maturity, simulation is increasingly used by SMEs for numerical process development, and, through the increasing digitization, also for datamining.

In important caveat, however, is that the predictive accuracy of these FE simulations strongly depends on, amongst others, the adopted material model. For an accurate calculation of the joint geometry and its mechanical strength, accurate large strain flow curves are required. A myriad of experimental techniques have been developed to determine the large strain flow curve of sheet metal. In this regard, there are two issues. Firstly, these material tests are typically dominated by a certain stress state and yield different results depending on the degree of plastic anisotropy exhibited by the sheet metal. Secondly, due to the small dimensions of the forming tools (e.g. punch or rivet) compared to the nominal sheet thickness, joining by forming processes of sheet metal must be regarded as a bulk forming problem in which the through-thickness stress cannot be ignored. The crux of the problem here is that the plastic material behaviour of sheet metal is conventionally determined using material tests, which are confined to homogeneous plane stress conditions in the plane of the sheet.

Due to a multitude of methods for determining flow curves and the variety of phenomenological hardenings laws models to describe them, problems arise with respect to reproducibility and accuracy in joining by forming simulations. The latter threatens the advantages of numerical process development.

The aim of this research project is to devise a process-informed selection strategy for the selection of flow curves determination methods tailored for FE simulations in mechanical joining. The key point of the method is the identification of the dominating stress state in the joining by forming process at hand, which is then used to select the most appropriate material test to identify the large strain flow curve.

Several material tests are conducted in collaboration with research labs and institutes across the globe. The developed selection strategy is applied to two representative joining by forming techniques, namely clinching and self-pierce riveting. The experimental validation enabled to derive guidelines to identify accurate flow curves for simulating joining by forming processes.

The framework presented in this report enables to arrive at industrial relevant guidelines for the selecting the most appropriate method to identify the large strain flow curve, and, consequently, increase the accuracy of numerical process development in joining by forming.

---

## Table of contents

<b>List of figures</b> .....	<b>IV</b>
<b>List of tables</b> .....	<b>X</b>
<b>1 Introduction</b> .....	<b>10</b>
<b>2 State of the art</b> .....	<b>11</b>
2.1 Self-pierce riveting .....	11
2.2 Clinching .....	12
2.3 Flow curve determination for mechanical joining.....	15
2.4 Large strain flow curve of sheet metal.....	18
<b>3 Problem and research objective</b> .....	<b>26</b>
<b>4 Materials, equipment and tools</b> .....	<b>31</b>
4.1 Investigated materials .....	31
4.2 Joining setup.....	32
4.3 Joining elements and tools.....	33
<b>5 Experimental joint analysis</b> .....	<b>35</b>
5.1 Procedure .....	35
5.2 Self-pierce riveting .....	38
5.3 Clinching .....	42
<b>6 Simulation models of the joining processes</b> .....	<b>46</b>
<b>7 Material testing requirements for joining by forming</b> .....	<b>47</b>
7.1 Plastic anisotropy .....	47
7.2 Large strain flow curve .....	50
7.3 Strain rate effect.....	55
7.4 Conclusions .....	63
<b>8 Material characterization methods</b> .....	<b>64</b>
8.1 Tensile test.....	64
8.2 Extended tensile test.....	66
8.3 Stack compression test (SCT).....	67
8.4 Plane strain compression test (PSCT) .....	69
8.5 In-plane torsion test (IPPT) .....	70
8.6 Hydraulic bulge test (HBT) .....	73

---

<b>9</b>	<b>Numerical stress analysis</b> .....	<b>75</b>
9.1	Stress-state metric.....	75
9.2	Process-informed method selection.....	77
9.3	Clinching.....	79
9.4	Self-pierce riveting.....	83
9.5	Material characterization tests.....	87
9.6	Comparison of joining processes and material tests.....	98
<b>10</b>	<b>Experimental and numerical study of the stack compression test</b> .....	<b>100</b>
10.1	Initial state and parameters of the stack compression test.....	100
10.2	Manufacturing process of the discs.....	101
10.3	Influence and correction of friction.....	102
10.4	Influence of diameter and number of discs.....	104
10.5	Influence of a shift in hydrostatic pressure.....	110
10.6	Round Robin test.....	117
<b>11</b>	<b>Evaluation of flow curves from considered material tests</b> .....	<b>121</b>
11.1	Flow curve extrapolation.....	121
11.2	Flow curve comparison.....	122
<b>12</b>	<b>Determination of flow curves for SPR-ST rivets</b> .....	<b>126</b>
<b>13</b>	<b>Numerical assessment of flow curves</b> .....	<b>129</b>
13.1	Flow curve comparison for self-pierce riveting.....	129
13.2	Flow curve comparison for clinching.....	131
<b>14</b>	<b>Recommendations for flow curve determination for mechanical joining</b> ..	<b>133</b>
<b>15</b>	<b>Summary</b> .....	<b>135</b>
	<b>Dissemination plan</b> .....	<b>136</b>
	<b>List of Literature</b> .....	<b>138</b>
	<b>Attachments</b> .....	<b>144</b>

## List of figures

Figure 1: Process steps of self-pierce riveting (SPR) with semi-tubular rivets [Hah1996]....	11
Figure 2: SPR joint with geometric properties [DVS2014].....	11
Figure 3: Manufacturing sequence of clinching with rectangular tools [Eck1999] .....	12
Figure 4: Schematic drawing rectangular clinched joint [Kul2012].....	13
Figure 5: Scheme of process steps for clinching with rigid (above) and divided (below) die [DVS2012] .....	13
Figure 6: Most important geometric characteristics of a clinching joint [DVS2012].....	14
Figure 7: The effect of plastic anisotropy (Table 1) on the forming of the interlock region under various angles with respect to the Rolling Direction.....	16
Figure 8: Typical strain rates in forming and joining processes. After [HAR17] .....	17
Figure 9: Hardening stages: schematic illustration .....	19
Figure 10: Strain hardening (RD) of a low carbon steel. Voce law fitted in the pre-necking region.....	20
Figure 11: Improved fitting quality by the two-stage Voce model.....	20
Figure 12: Large strain flow curve of low carbon steel sheet. Left: Large strain flow curve obtained by pre-staining wires and subsequent tensile tests [SEV8P]. Right: recent determination of flow curve through the in-plane torsion test [TRA18].....	21
Figure 13: Identification of the large strain flow curve of sheet metal. Homogenous testing, Homogenous testing of pre-strained material and Inverse Identification .....	24
Figure 14: Comparison of aluminum EN AW-6016 flow curves between tensile and upsetting test; left: influence of anisotropy, right: influence of approximation approaches for flow curve extrapolation .....	26
Figure 15: Local and transient stress state for clinched joint EN AW-7021 T4 ( $t = 2.0$ mm) in EN AW-6016 T4 ( $t = 1.2$ mm) .....	27
Figure 16: Simulation results for the self-pierce riveting process with varying material tests and flow curve approximations .....	28
Figure 17: Single-stroke non-cutting round clinched joint. Material DC05, initial thickness 1.15 mm. Left Panel: contour measurement. Right panel: encapsulated cross-section.....	29
Figure 18: Final interface in the interlock region between upper and lower sheet calculated using different strain hardening models .....	29
Figure 19: Left panel: strain hardening models identified using different methods. Right panel: sensitivity of the shear lap simulation with respect to the hardening model .....	29
Figure 20: Mechanical properties for the considered materials.....	31
Figure 21: Test stand for the joining experiments .....	32
Figure 22: Dimensions for tools and rivets used for SPR.....	33
Figure 23: Dimensions for tools used for Clinching.....	34
Figure 24: Automatic (left) and manual (right) contour measurement of a clinched joint.	35
Figure 25: Contour measurement and calibration of an SPR connection. ....	36
Figure 26: Contour measurement and calibration of a clinch connection. ....	37

---

Figure 27: Results of the experimental joining analysis for SPR of EN AW-5182 ( $t = 1,1$ mm) in EN AW-5182 ( $t = 1,1$ mm) .....	38
Figure 28: Results of the experimental joining analysis for SPR of DC04 ( $t = 1,0$ mm) in DC04 ( $t = 1,0$ mm) .....	39
Figure 29: Results of the experimental joining analysis for SPR of CR330Y590T-DP ( $t = 1,0$ mm) in EN AW-5182 ( $t = 1,1$ mm) .....	40
Figure 30: Results of the experimental joining analysis for SPR of EN AW-6082 T6 ( $t = 1,1$ mm) in EN AW-6082 ( $t = 1,1$ mm) .....	41
Figure 31: Results of the experimental joining analysis for clinching of EN AW-5182 ( $t = 1,1$ mm) in EN AW-5182 ( $t = 1,1$ mm) .....	42
Figure 32: Results of the experimental joining analysis for clinching of DC04 ( $t = 1,0$ mm) in DC04 ( $t = 1,0$ mm) .....	43
Figure 33: Results of the experimental joining analysis for clinching of CR330Y590T-DP ( $t = 1,0$ mm) in EN AW-5182 ( $t = 1,1$ mm) .....	44
Figure 34: Results of the experimental joining analysis for clinching of EN AW-6082 T6 ( $t = 1,1$ mm) in EN AW-6082 ( $t = 1,1$ mm) .....	45
Figure 35: Simulation models for SPR and Clinching .....	46
Figure 36: Flow curves obtained a low carbon steel by the tensile test and the stack compression test (left). The effect of differential work hardening on the yield locus after a 0.05 true plastic strain (right) .....	48
Figure 37: Stress state fitting of the von Mises yield criterion .....	49
Figure 38: Flow curves used for assessing differential work hardening in clinch forming .....	49
Figure 39: Effect of differential work hardening in clinch forming. Cross-section (left) and process graph (right) .....	50
Figure 40: Concept of the Virtual Experiment to derive requirements for the large strain flow curve in clinch forming .....	51
Figure 41: Reference strain hardening (Swift) and fitted Voce model using different data sets according to typical material tests to identify the flow curve .....	52
Figure 42: Reference strain hardening (Swift) and fitted Voce model using different data sets according to typical material tests to identify the flow curve: the pre-necking region .....	52
Figure 43: Effect of hardening law selection and strain range used to fit the hardening law .....	53
Figure 44: Ludwik-Holomon hardening fitted to the pre-necking data of the reference strain hardening represented by Swift's hardening law .....	54
Figure 45: Effect of hardening law selection: Ludwik-Holomon fitted to the pre-necking data of the reference material .....	54
Figure 46: Effect of strain rate dependency in clinch forming .....	56
Figure 47: Calibration of the strain rate dependent hardening model .....	57
Figure 48: Effect of strain rate dependency in clinch forming .....	57
Figure 49: Extrapolation of the rate dependent hardening model (calibrated in the pre-necking region) .....	58
Figure 50: Effect of strain rate and thermal softening on the process graph in clinch forming .....	60

---

Figure 51: Left: temperature within the clinched joint just after complete die filling. Right: evolution of temperature in the bottom of the joint. After 1s: tools removed .....	60
Figure 52: Average joint contour (left) and process graph (right) for clinching with different punch speeds of DC04 in DC04 .....	61
Figure 53. Average joint contour (left) and process graph (right) for clinching with different punch speeds of EN AW-5182 in EN AW-5182 .....	62
Figure 54: Material tests available for the characterization of material in sheet metal forming [YIN14].....	64
Figure 55: A typical tensile-test specimen strip (MAR02).....	65
Figure 56: Schematic overview of the Extended Tensile Test .....	67
Figure 57: The schematic experimental set-up for stack compression test [COP10].....	68
Figure 58: The schematic experimental set-up for plane strain compression test [GEL94] .	69
Figure 59: Scaling the PSCT to the UTT in accordance with the work equivalence condition. After [CHE20].....	70
Figure 60: Experimental setup of in-plane torsion test (left) and variation of shear stress along the radial direction for specimen in-plane torsion test (right).....	71
Figure 61: Details of the specimen used in groove in-plane torsion test.....	72
Figure 62: The process limit for in-plane torsion test [TEK82] (right) and Wrinkling effect in DC04 for higher rotation at in-plane torsion test [TRA18] .....	73
Figure 63: The schematic setup for hydraulic bulge test [MIN17] and the experimental set-up for the hydraulic bulge test [COP18] .....	74
Figure 64: Lode angle and triaxiality (after [BAI]) .....	75
Figure 65: The ( $\omega$ - $\eta$ )-diagram (left) with the plane stress path associated with the normalized von Mises yield locus (right).....	76
Figure 66: Stress state analysis linked with the material tests .....	76
Figure 67: Clinch forming: Stage I. Equivalent Plastic Strain (Upper), Triaxiality (Middle), Stress metric $\omega$ (Lower). .....	77
Figure 68: Instantaneous and average values of triaxiality and $\omega$ .....	78
Figure 69: Stress state analysis clinch forming Stage I: Upper Sheet .....	78
Figure 70: Clinch forming: stress state analysis of DC04 ( $t = 1.0$ mm) in DC04 ( $t = 1.0$ mm) after joining completion.....	79
Figure 71: Stress state analysis clinching forming stage IV DC04-DC04: Upper sheet .....	80
Figure 72: Stress state analysis clinching forming stage IV DC04-DC04: Lower sheet .....	80
Figure 73: Clinch forming: stress state analysis of EN AW 6082 ( $t = 1.5$ mm) in EN AW 6082 ( $t = 1.5$ mm) after joining completion.....	81
Figure 74: Stress state analysis clinching forming stage IV EN AW 6082- EN AW 6082: upper sheet.....	81
Figure 75: Stress state analysis clinching forming stage IV EN AW 6082- EN AW 6082: lower sheet .....	81
Figure 76: Clinch forming: stress state analysis of CR330Y590T-DP ( $t = 1$ mm) in EN AW 5182 ( $t = 1$ mm) after joining completion.....	82
Figure 77: Stress state analysis clinching forming stage CR330Y590T-DP EN AW 5182: upper sheet (CR330Y590T-DP).....	82

---

Figure 78: Stress state analysis clinching forming stage IV CR330Y590T-DP - EN AW 5182: lower sheet (EN AW 5182) .....	82
Figure 79: Plastic equivalent strain, triaxiality and omega for the SPR process of EN AW-5182 ( $t = 1.1$ mm) in EN AW-5182 ( $t = 1.1$ mm) .....	83
Figure 80: Diagrams for plastic equivalent strain over omega and omega over triaxiality for all elements the SPR simulation of EN AW-5182 ( $t = 1.1$ mm) in EN AW-5182 ( $t = 1.1$ mm) .....	84
Figure 81: Plastic equivalent strain, triaxiality and omega for the SPR process of DC04 ( $t = 1.1$ mm) in DC04 ( $t = 1.1$ mm) .....	85
Figure 82: Diagrams for plastic equivalent strain over omega and omega over triaxiality for all elements the SPR simulation of DC04 ( $t = 1.0$ mm) in DC04 ( $t = 1.0$ mm) .....	86
Figure 83: Structure of the simulation model analysis of the uniaxial tensile test .....	87
Figure 84: Calculated equivalent plastic strain, stress triaxiality and omega for the tensile test .....	88
Figure 85: Distribution of strain elements in relation to stress triaxiality and omega for the tensile test .....	89
Figure 86: Structure of the simulation model for analysis of the stack compression test .....	90
Figure 87: Calculated equivalent plastic strain, stress triaxiality and omega for the stack compression test .....	91
Figure 88: Calculated distribution of strain elements in relation to stress triaxiality and omega for stack compression test .....	91
Figure 89: Structure of the simulation model for analysis of the plane strain compression test .....	92
Figure 90: Calculated equivalent plastic strain, stress triaxiality and omega for the plane strain compression test .....	93
Figure 91: Calculated distribution of strain elements in relation to stress triaxiality and omega for the plane strain compression test .....	93
Figure 92: Structure of the simulation model for numerical analysis of the in-plane torsion test .....	94
Figure 93: Calculated equivalent plastic strain, stress triaxiality and omega for the in-plane torsion test .....	95
Figure 94: Calculated distribution of strain elements in relation to stress triaxiality and omega for the in-plane torsion test .....	95
Figure 95: Structure of the simulation model for numerical analysis of the hydraulic bulge test .....	96
Figure 96: Calculated equivalent plastic strain, stress triaxiality and omega for the hydraulic bulge test .....	96
Figure 97: Calculated distribution of strain elements in relation to stress triaxiality and omega for the hydraulic bulge test .....	97
Figure 98: Plane stress path with stress state results of different mechanical tests. After [BON18] .....	97
Figure 99: Comparison of the max. plastic strain, stress triaxiality and omega for the considered material tests and joining methods SPR and clinching .....	98

Figure 100: Comparison of simulated max. plastic strain, triaxiality and omega of SPR, clinching and the stack compression test.....	100
Figure 101: Characteristics of the stack compression test.....	100
Figure 102: Influence of disc manufacturing process on flow curve quality form the stack compression test for DC04 and EN AW-5182.....	101
Figure 103: Comparison of eroded (left) and turned (right) discs from EN AW-5182.....	102
Figure 104: SEM image of the edge area of a CR330Y590 disc after eroding .....	102
Figure 105: Comparison of simulated force-displacement curves of the SCT with varied conditions for disc to disc friction .....	103
Figure 106: Comparison of simulated force-displacement curves of the SCT with varied conditions for tool to disc friction and varied disc diameters .....	103
Figure 107: Friction correction of the flow curve from the SCT according to Siebel (left) and friction coefficients for the considered materials .....	104
Figure 108: Influence of disc diameter on triaxiality and omega at the stack compression test of DC04 ( $h_1 = h_0/2$ ).....	105
Figure 109: Influence of starting disc diameter ( $d_0$ ) and number of discs ( $n_d$ ) on calculated average triaxiality at the stack compression test.....	106
Figure 110: Flow curves for CR330Y590T-DP carried out by the SCT with varied disc diameters .....	106
Figure 111: Flow curves for CR330Y590T-DP carried out by the SCT with varied number of discs.....	107
Figure 112: Flow curves for DC04 carried out by the SCT with varied discs diameters.....	107
Figure 113: Flow curves for DC04 carried out by the SCT with varied discs diameters.....	108
Figure 114: Influence of max. strain from the experiment on the Hockett-Sherby extrapolation .....	110
Figure 115: Flow curves obtained through SCT and HBT. Material: CR330Y590T-DP .....	111
Figure 116: Cross-section compressed stack CR330Y590T-DP. Left: experimental. Right panel: FE simulation using HBT-flow curve and $\mu=0.05$ .....	113
Figure 117: Thickness after compression measured at the centre of each individual disc. Material: CR330Y590T-DP .....	114
Figure 118: Flow curves obtained through SCT (with and without correction for friction) and HBT. Material: CR330Y590T-DP .....	114
Figure 119: Pressure dependency as a function of the plastic equivalent strain (CR330Y590T-DP) .....	117
Figure 120: Force –displacement curves stack compression test for CR330Y590-DP (3 discs, diameter 10 mm).....	118
Figure 121: Disc localization CR330Y590-DP (3 discs, diameter 10 mm) .....	118
Figure 122: Lubricant Depletion CR330Y590-DP (3 discs, diameter 10 mm) .....	118
Figure 123: Cross section CR330Y590-DP (3 discs, diameter 10 mm) after interrupted SCT .....	119
Figure 124: Interrupted SCT CR330Y590-DP (3 discs, diameter 10 mm) .....	119
Figure 125: Influence of the lubricant CR330Y590-DP (3 discs, diameter 10 mm).....	120
Figure 127: Extrapolation of SCT Data using commonly adopted hardening laws .....	122

---

Figure 128: Normalized yield stress $\sigma_b/\sigma_0$ as a function of the equivalent plastic work for EN AW-5182, DC04 and CR330590T-DP .....	123
Figure 129: Flow curves from considered material tests for DC04 .....	124
Figure 130: Flow curves from considered material tests for CR330Y590-DP .....	124
Figure 131: Flow curves from considered material tests for EN AW-5182 .....	125
Figure 132: Flow curves from considered material tests for EN AW-6082 T6 .....	125
Figure 133: Plastic equivalent strain and triaxiality of the rivet at the end of the SPR process .....	126
Figure 134: Characterization methods for rivet material .....	127
Figure 135: Flow curves (not corrected) from ring compression test with different ring heights of the rivet material with hardness class H4 .....	127
Figure 136: Comparison of the flow curves from the bar tensile test of the base material and the ring compression test for the rivet material for hardness class 4 .....	128
Figure 137: Comparison of simulation results with different flow curves for SPR of DC04 ( $t = 1.0$ mm) in DC04 ( $t = 1.0$ mm) .....	129
Figure 138: Comparison of simulation results with different flow curves for SPR of EN AW-5182 ( $t = 1.1$ mm) in EN AW-5182 ( $t = 1.1$ mm) .....	130
Figure 139: Comparison of simulation results with different flow curves for Clinching of DC04 ( $t = 1.0$ mm) in DC04 ( $t = 1.0$ mm) .....	131
Figure 140: Comparison of simulation results with different flow curves for Clinching of EN AW-5182 ( $t = 1.1$ mm) in EN AW-5182 ( $t = 1.1$ mm) .....	132
Figure 141. Flowchart process -and material-informed material test selection for flow curve determination in joining by forming. ....	<b>Fehler! Textmarke nicht definiert.</b>

---

## List of tables

Table 1: Lankford ratio's, coefficient of normal anisotropy and degree of planar anisotropy .	15
Table 2: Characteristics of the plastic deformation imparted by forming processes [SEV80] .....	17
Table 3: Commonly adopted hardening laws for the approximation of flow curves with application range in accordance with [TOM02] .....	22
Table 4: Characteristics of the plastic deformation imparted by the material tests .....	25
Table 5: Considered material combination for each joining method .....	31
Table 6: Used process parameters for SPR .....	33
Table 7: Used process parameters for clinching.....	34
Table 8: JC parameters obtained from [VER11]. .....	59
Table 9: Full thermo-mechanical model: parameters.....	59
Table 10: GrooveDimensions of groove in relation to sheet thickness .....	72
Table 11: Comparison of scattering at SCT with different disc diameter and number of discs for DC04 and EN AW-5182.....	109
Table 12: Hardness table for SPR rivets [DVS/EFB 3410].....	126



# 1 Introduction

Nowadays SMEs increasingly resort to FE simulation for numerical process development. This is further sparked through the increasing digitization, including for datamining purposes. It is well-known that the reliability of a FE simulation for technological processes depends on, among others, the accuracy of the adopted material model. Technological processes – in the context of this project the mechanical joining processes clinching and self-pierce riveting – put specific demands with regard to model performance. Given that the final joint geometry largely determines the mechanical strength of the joint, it is important that the metal flow is accurately simulated. Moreover, when resorting to FE simulation for predicting the mechanical strength the accuracy of the predicted stress and strain state within the joint is equally important.

During joining by forming of sheet metal a multitude of stress states is generated accompanied with large plastic straining of the material. From a simulation point of view, however, plastic anisotropy of the sheet metal can be safely ignored for predicting the metal flow. Indeed, the metal flow is usually strongly constrained by the joining tools preventing plastic anisotropy to manifest itself at the length scale of the joint. Consequently, joining by forming is usually simulated assuming a plastically isotropic material model solely requiring a large strain flow curve to account for strain hardening.

Obviously, standard tensile tests are of limited usefulness because necking limits uniform deformation. Several experimental techniques have been developed to determine the large strain flow curve of sheet metal. Due to the multitude of methods along with the myriad of hardening models to describe flow behaviour, problems arise with respect to the reproducibility and the accuracy in joining by forming simulations.

Furthermore, material tests are typically dominated by a certain stress state and yield different results depending on the degree of plastic anisotropy. In addition, due to the small dimensions of the forming tools (e.g. punch or rivet) compared to the nominal sheet thickness, joining by forming processes of sheet metal must be regarded as a bulk forming problem in which the through-thickness stress cannot be ignored. The crux of the problem here is that the plastic material behaviour of sheet metal is conventionally determined using material tests, which are confined to homogeneous plane stress conditions in the plane of the sheet. Sheet metal itself often exhibits plastic anisotropy. As such, when assuming isotropic plastic material behaviour for simulating joining by forming, it is deemed appropriate to identify the flow curve using a material test which generates a stress state resembling the dominating stress state in the joining process at hand.

The aim of the project is to present a generic methodology to identify the most appropriate material test for acquiring the large strain flow curve enabling to increase accuracy of numerical process development in joining by forming. The key point in the presented methodology lies in determining the dominating stress state during the joining by forming technique at hand. The latter information is then linked to the most appropriate material test. In this project, several materials test are considered in collaboration with other research labs at universities, institutes and companies. The devised process-informed selection strategy is applied to two representative joining by forming techniques, namely clinching and self-pierce riveting. Four industrially relevant joining cases are considered in this project. Experimental validation of the developed strategy is based on the experimentally measured final geometry of the joint and the process graph, i.e. the punch force versus the punch displacement, indirectly yielding information with respect to the stress levels within the joint. The presented framework provides a basis for standardization of determining flow curves tailored for FE simulations in mechanical joining.

## 2 State of the art

### 2.1 Self-pierce riveting

The self-pierce riveting (SPR) process with semi-tubular rivets can be separated in three steps (Figure 1). The work pieces and the rivet are positioned between punch, blank holder and die. Next, the punch presses the rivet into the work pieces. Due the cutting edge of the rivet, a slug will be punched into the punch-sided work piece and enclosed inside the rivet. Following, the shape of the die causes the rivet to expand and creates an interlock. At the end, the cavity of the die is completely filled with material [DVS2014].

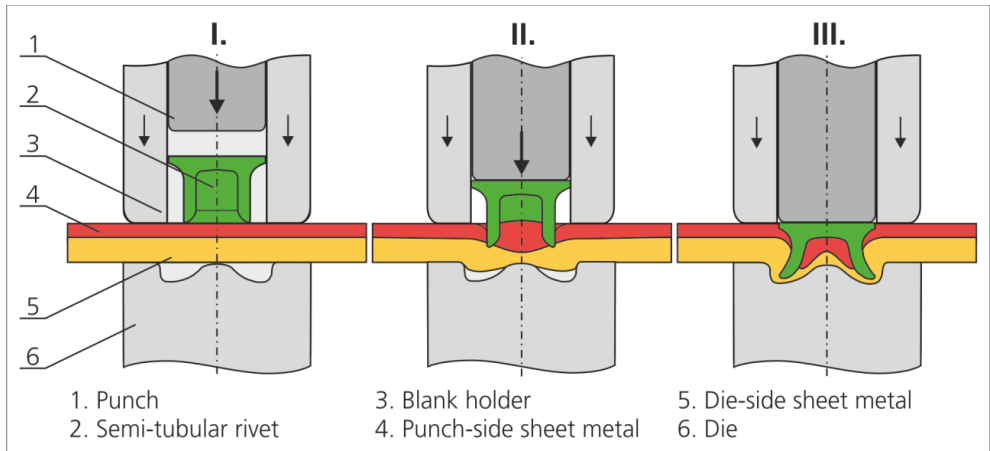


Figure 1: Process steps of self-pierce riveting (SPR) with semi-tubular rivets [Hah1996]

The main application area of self-pierce riveting is joining mixed compounds (e.g. steel and aluminium) and material combinations such as aluminium-aluminium. A two-sided accessibility of the parts to be joined is required. More than two parts can be joined with an overall sheet thickness in the range of 1-9mm [DVS2014].

The form closure between the rivet and the joining parts is determinative for the strength of the joint. The degree of the form closure is evaluated by geometric parameters of the joint formation. These parameters and the requirements used in this project are shown in Figure 2.

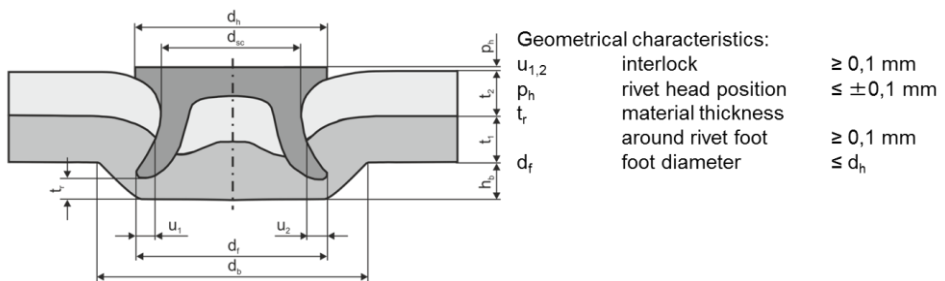


Figure 2: SPR joint with geometric properties [DVS2014]

## 2.2 Clinching

Clinch forming allows assembling thin metal parts by solely relying on local plastic deformation of the base material. Unlike traditional joining techniques, clinching does not use additional consumables (such as rivets). The basic principle of clinch forming processes is to create an interlock between the combining thin metal parts with the aid of relatively simple tools like a punch, a blank holder and a die. The punch locally pushes metal into the die and, depending on the shape of these clinching tools, the resulting metal flow targets the creation of a mechanical interlock. The shape of clinching tools can be rectangular or round.

Rectangular clinching tools are shown in Figure 3 along with the manufacturing sequence. It can be inferred from Figure 3 that this method shears the sheets in such a way that the upper sheet is forced through the slits in the lower sheet. The technique shown in Figure 3 relies on a die with deflecting spring plates which allow for the creation of an interlock. If one joining partner exhibits limited ductility and corrosion is no issue, than rectangular clinching tools enable to establish a clinched connection.

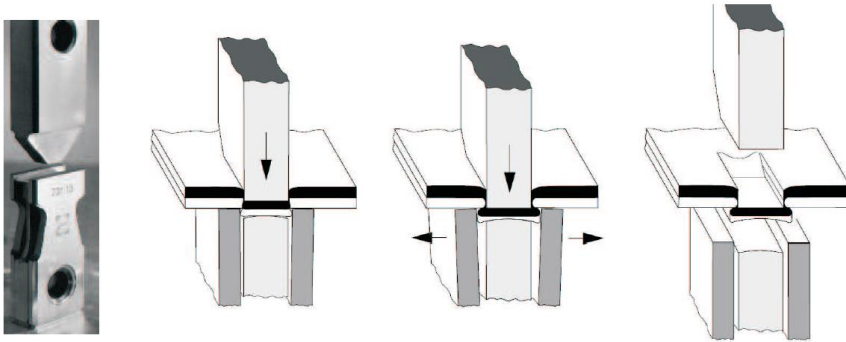


Figure 3: Manufacturing sequence of clinching with rectangular tools [Eck1999]

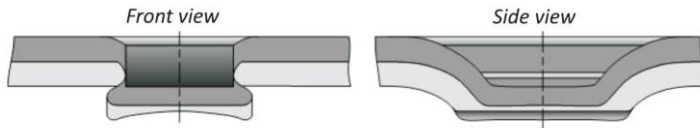


Figure 4: Schematic drawing rectangular clinched joint [Kul2012]

Conventional clinching tools, however, are round yielding symmetrical load-bearing joints with superior fatigue strength. In the here described project clinching with rigid die as well as clinching with divided die is considered. The process steps of these two methods are shown in Figure 5.

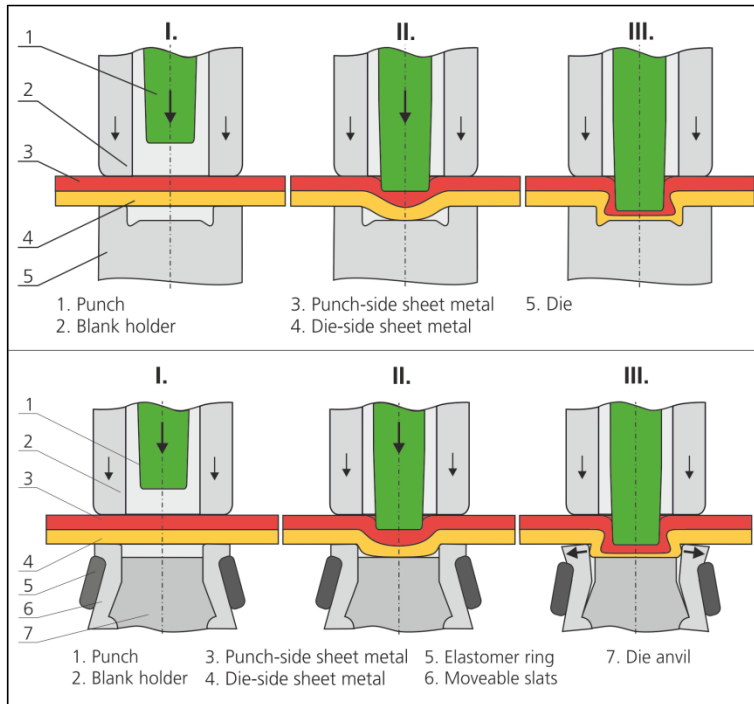


Figure 5: Scheme of process steps for clinching with rigid (above) and divided (below) die [DVS2012]

The mechanical strength of the clinched joint strongly depends on the final geometry of the joint. The most important geometric characteristics of a clinching joint are shown in Figure 6.

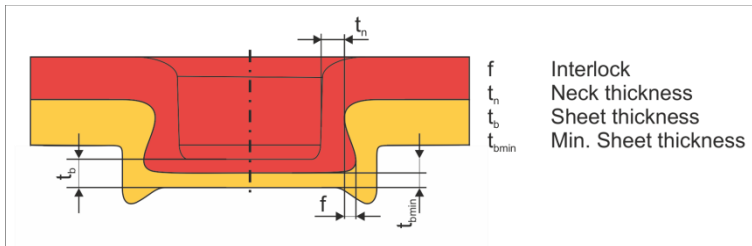


Figure 6: Most important geometric characteristics of a clinching joint [DVS2012]

## 2.3 Flow curve determination for mechanical joining

The numerical modelling of the clinching and SPR process has been considered in a large number of publications. In the majority of the research work, for example [Bus11] for clinching and [Hah01] for SPR, the flow curves required for the simulation were determined from the tensile test and extrapolated using a phenomenological hardening law. To mitigate the uncertainty associated with extrapolating the experimental data to larger strains, some researchers adopted other material tests, e.g. Coppieters [COP12] and Behrens et al. [BEH16] used the stack compression test and the hydraulic bulge test to acquire large strain flow curve, respectively. Different approaches to flow curve determination for rivets have also been published. [ECK09] chose the method of the tensile test of the rivet's starting material and [HÖN19] the compression test of a ring made from the rivet.

Previous studies and research projects on mechanical joining dealing with simulation tasks are confined to presenting the adopted flow curves and the associated simulation accuracy. However, an error analysis with respect to the adopted flow curves is often lacking in the previous research efforts. The issue of flow curve accuracy for self-pierce riveting simulation is studied by [ECK09]. Drossel and Israel [DRO13] and Coppieters [COP12] used different approaches to determine the large strain flow curve showing the influence on formation a clinched joint. However, a consistent study on flow curve determination for simulating joining by forming cannot be found in literature. Before embarking on flow curve determination, the following paragraphs focus on the generic characteristics of the imparted plastic deformation during joining by forming. In addition, the basic theory of work hardening is summarized.

### Plastic anisotropy

During clinch forming and riveting a multitude of stress states is generated accompanied with large plastic straining of the material. From a simulation point of view, however, plastic anisotropy of the sheet metal can be ignored for predicting the metal flow [COP12]. Indeed, the metal flow is strongly constrained by the joining tools preventing plastic anisotropy to manifest itself at the length scale of the joint. As such, joining by forming is usually simulated assuming a von Mises material (i.e. J2 plasticity) solely requiring a large strain flow curve to account for strain hardening. Figure 7 shows the effect of planar anisotropy on the prediction of the interlock in clinching. To this end, the 3D Hill48 yield criterion is adopted using a 3D FE model to simulate the forming process. It can be inferred that relatively strong planar anisotropy (see Table 1) does not affect the metal flow. The interlock region under various angles with respect to the rolling direction is not affected by the plastic anisotropy of the material. The absolute stress levels within the joint, however, are likely affected by the degree of plastic anisotropy. The latter is also the reason that strength predictions are potentially affected by planar anisotropy [SAB08, COP12].

Table 1: Lankford ratio's, coefficient of normal anisotropy and degree if planar anisotropy

$r_0$	$r_{45}$	$r_{90}$	$\bar{r}$	$\Delta r$
1.73	1.85	2.25	1.92	0.14

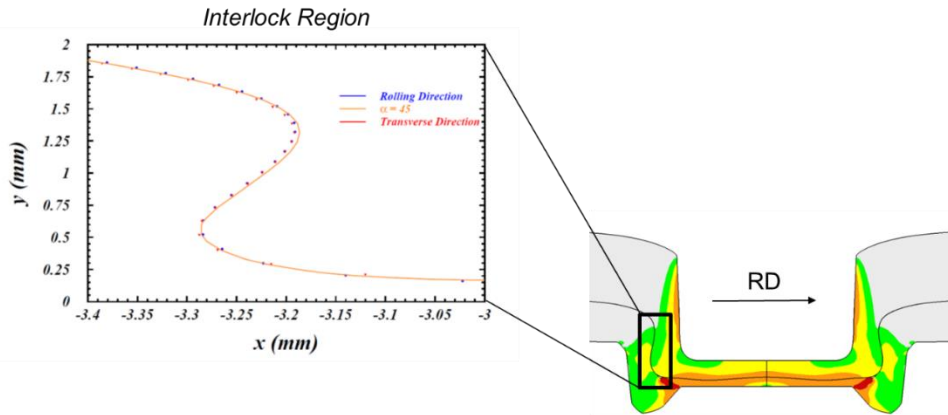


Figure 7: The effect of plastic anisotropy (Table 1) on the forming of the interlock region under various angles with respect to the Rolling Direction

As already stated, joining by forming is usually simulated assuming a von Mises material solely requiring a large strain flow curve to account for strain hardening. Besides the fact that in the majority of the joining by forming processes the plastic anisotropy does not manifest itself at the length scale of the joint, the use of an axisymmetric FE model inherently limits material modelling to J2 plasticity.

#### Magnitude of the imparted strain

The magnitude of the imparted strain in joining by forming can often only be determined by numerical models. Indeed, the deformation cannot be experimentally observed during the process. Typical order of magnitudes for clinching and riveting reported in the literature for both processes are shown in Table 2. It can be inferred that clinching and riveting generate much larger plastic deformations than imparted by conventional sheet forming operations or forging of bulk material.

#### Magnitude of the strain rate

The strain rate is determined by the punch speed in joining processes. As mechanical joining is often characterized by short process times, the sheet metal can be subjected to high strain rates. As a consequence, the temperature of the forming zone could potentially increase significantly because the forming energy is converted into heat. The latter could cause thermal softening of the material. As such, high speed joining by forming involves two potential aspects:

- i) a strain rate effect;
- ii) thermal softening.

These effects can have a concurring effect on the material behaviour. However, the literature on this subject is very limited. Hartel et al. [HAR17] shows that flat-clinching generates locally temperatures up to 226 °C. The authors found that a thermo-mechanically coupled simulation model is required to accurately simulate flat-clinching. Clearly, strain rate effects and potential thermal softening are underexposed topics in research in joining by forming technology. According to Hartel et al. [HAR17], industrial application of clinching and riveting imposes strain rates in the order of 150 to 300  $\frac{1}{s}$ , see Figure 8.

### Predominant deformation mode

Joining by forming processes generate complex deformation modes with substantial compressive and tensile strain components, depending on the particular mechanical joining technique. The mechanical joining techniques considered in this study are mainly applied to shell-like thin-walled metallic products. As opposed to conventional sheet metal forming, joining by forming techniques subject the material a 3D stress state. As a consequence, joining by forming must be regarded as a bulk forming process of shell-like materials.

Table 2: Characteristics of the plastic deformation imparted by forming processes [SEV80]

Process	Predominant deformation mode	Typical order of magnitude of imparted strain	Order of magnitude of strain rate $\dot{\phi}$	Remarks
Forging	Complex modes with substantial compressive strain components	0.5 to 1	10 → 1000	Heterogeneous deformation occurs
Sheet forming	Biaxial expansion or plane strain elongation	0.6	0.1 → 100	Approx. homogeneous through-thickness strain. Very heterogeneous strain from point to point in the blank
Clinching	Complex deformation history	2 → 3	1 → 150	Bulk forming of shell-like products
Riveting	Complex deformation history	> 3	1 → 300	Bulk forming of shell-like products

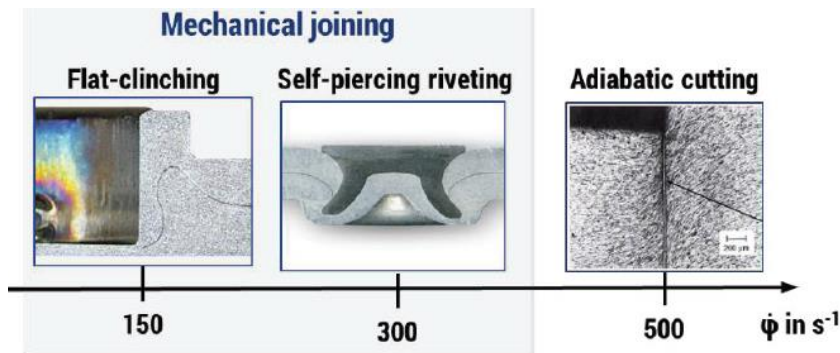


Figure 8: Typical strain rates in forming and joining processes. After [HAR17]

## 2.4 Large strain flow curve of sheet metal

### 2.4.1 Large strain flow curve

Work hardening is a result of dislocation interaction processes and the aim of a work hardening theory is to predict the “flow curve”:

$$\sigma_{eq} = f(\varepsilon_{eq}^{pl}, q_i)$$

The equivalent stress  $\sigma_{eq}$  is a function  $f$  of the equivalent plastic strain  $\varepsilon_{eq}^{pl}$ , and a number of model parameters  $q_i$ . Both  $\sigma_{eq}$  and  $\varepsilon_{eq}^{pl}$  are scalars related the actual tensorial stress and strain states, respectively. The reference datum for strain hardening, i.e. the flow curve, is usually measured in the Rolling Direction (RD) of the metal sheet. The applicability of flow curves presupposes the existence of equivalence criteria for stresses and strain permitting to derive any complex deformation from a unique “equivalent flow curve”, i.e. the function  $f$ .

Obviously, the function  $f$  is linked on micro-mechanical phenomena responsible for work hardening driven by a variety of microstructural parameters such as the dislocation density and grain size. Strain hardening of polycrystals is typically divided into different stages. These stages are schematically shown in Figure 9 by plotting the hardening rate  $\theta$  as a function of the critical resolved shear stress  $\tau$ :

$$\theta = \frac{d\tau}{d\Gamma}$$

With  $\Gamma$  the overall amount of dislocation slip as a representation of the strain. As soon as yielding occurs in polycrystals, stage III hardening starts. For metals, the micro-mechanisms in stage III as well understood and a widely accepted model has been proposed by Kocks [KOC76]. The latter model for stage III hardening reads as:

$$\theta = \theta_0 \left(1 - \frac{\tau}{\tau_{III}}\right)$$

With  $\theta_0$  the hardening rate at  $\tau = 0$  and  $\tau_{III}$  the saturation stress associated with stage III, respectively. This model can be converted using the Taylor factor to a flow curve, i.e. the classical Voce model [VOC48]:

$$\sigma_{eq} = C(1 - m e^{-K\varepsilon_{eq}^{pl}})$$

It must be noted that for stage III hardening, the Voce model is a micro-mechanically based hardening model. The red curve in Figure 10 shows the strain hardening of a low carbon steel sheet in the RD (Rolling Direction) during a tensile test. The blue curve is the Voce model fitted to the available pre-necking hardening data, i.e. the result from the tensile test. It can be inferred that the overall fitting quality is good, but zooming learns that the model does not perfectly captures the strain hardening close to the point of maximum uniform strain.

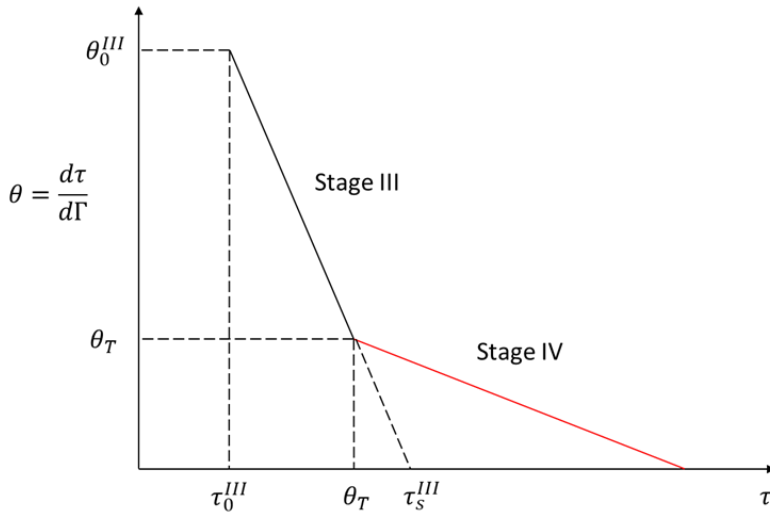


Figure 9: Hardening stages: schematic illustration

This is particularly of relevance when dealing with large deformations. Indeed, one can easily understand that extrapolation into the post-necking region (i.e. beyond maximum uniform strain) using the calibrated Voce law as shown in will yield erroneous post-necking strain hardening behaviour. Voce's model is clearly not "flexible" enough to model this behaviour. A possibility that has been used to deal with this problem is the description of flow curves by more successive equations, for example a two-stage Voce model [COP18]:

$$\tau = \begin{cases} \tau_{sat}^{III} - (\tau_{sat}^{III} - \tau_0) \exp\left(\frac{-\theta_0}{\tau_{sat}^{III} - \tau_0} \gamma\right) & \text{for } \gamma \leq \gamma_T \\ \tau_{sat}^{IV} - (\tau_{sat}^{IV} - \tau_T) \exp\left(\frac{-\theta_T}{\tau_{sat}^{IV} - \tau_T} (\gamma - \gamma_T)\right) & \text{for } \gamma \geq \gamma_T \end{cases}$$

The latter model can be transformed via the Taylor factor to a flow curve. The two-stage strain hardening model is fitted to the same tensile data as shown in Figure 10. Figure 11 shows the result and due to the increased flexibility, the two stage Voce model perfectly captures the strain hardening up to maximum uniform strain. The fitting process yields also a value for the transition point between stage III and stage IV hardening. It must be noted, however, that this value is merely a fitting result and has no physical meaning whatsoever as stage IV hardening is not likely to be probed in a tensile test. As such, the two-stage Voce model is merely used as a phenomenological model giving excellent accuracy for technological applications. As a large strain flow curve is a composite curve with different regions associated with different dominating mechanisms. Other equations can be proposed, see e.g. the p-model [COP14c], provided that they are in agreement with the phenomenology of large strain work hardening.

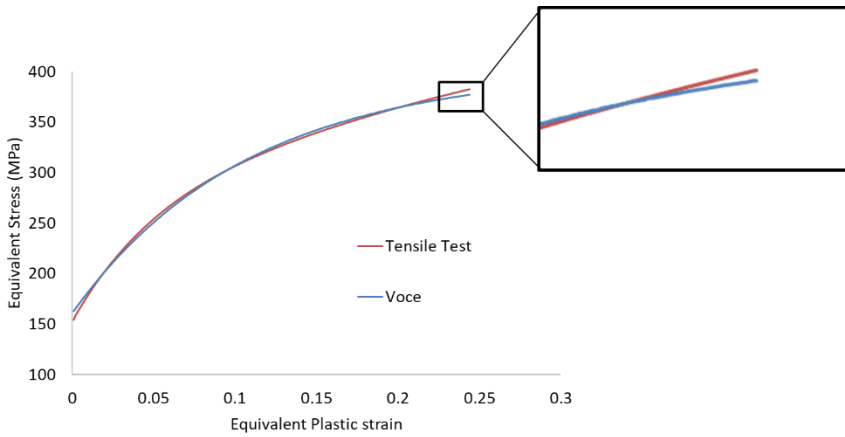


Figure 10: Strain hardening (RD) of a low carbon steel. Voce law fitted in the pre-necking region

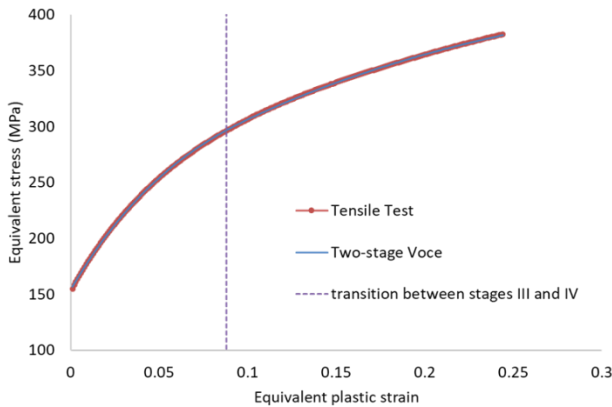


Figure 11: Improved fitting quality by the two-stage Voce model

Although the two-stage Voce model enables to capture the pre-necking strain hardening accurately, one cannot guarantee that the extrapolation of this two-stage Voce model is valid. Moreover, despite the physics behind the Voce-based hardening models, a pure phenomenological model often yields good results. For bcc materials, for example, it well-known that Swift's hardening law yields generally accurate description of the pre-necking strain hardening. A myriad of hardening laws is available in literature. Table 3 summarizes the most commonly adopted ones along with their typical application area. It must be noted that the application area is solely derived from pre-necking strain hardening data. For the post-necking regime one cannot easily assign the most appropriate hardening law for a material without access to experimental data in the post-necking regime. The reason is twofold. First, post-necking data is not widely available as is requires dedicated experiments. Second, the commonly adopted hardening laws were not devised to describe the post-necking regime of sheet metal.

The left panel of the Figure 12 shows a schematic large strain flow curve as deduced from early experiments by Sevillano et al. [SEV80]. The right panel shows a recent determination of the flow curve in the same strain range using the grooved in-plane torsion test on DC04 [TRA18]. It can be inferred that the experimental flow curve exhibits the same flow behaviour

as depicted in the left hand panel. Moreover, the flow behaviour is more complex than the behaviour describe by phenomenological hardening laws listed in Table 3.

Nevertheless, the use of a phenomenological hardening law is commonly adopted when simulating mechanical joining processes. The reason for this is that in the majority of the cases, extrapolation of the strain hardening into the post-necking regime is required. However, the validity of extrapolation may or may not be valid depending on the chosen hardening law. The uncertainty in this regard can only be reduced if larger strains can be probed. In the next section, an overview of the currently available experimental methods to do so is given.

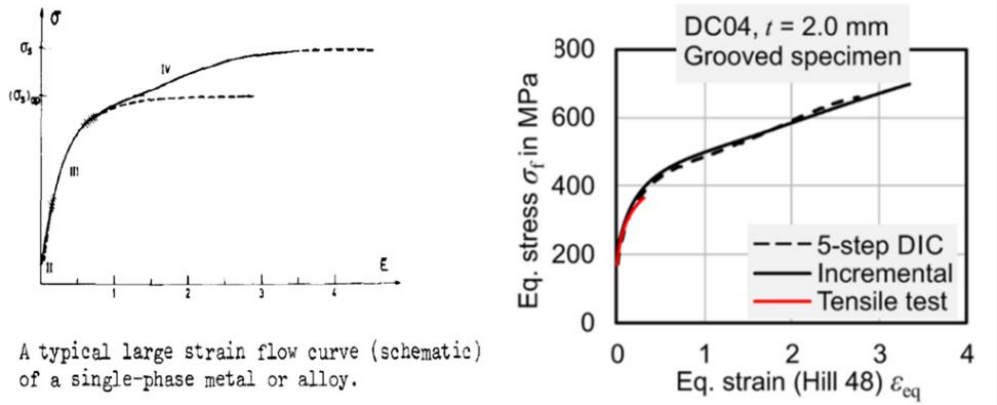


Figure 12: Large strain flow curve of low carbon steel sheet. Left: Large strain flow curve obtained by pre-staining wires and subsequent tensile tests [SEV8P]. Right: recent determination of flow curve through the in-plane torsion test [TRA18]

Table 3: Commonly adopted hardening laws for the approximation of flow curves with application range in accordance with [TOM02]

Source	Functional approach	Application area
<b>Linear approaches</b>		
Lippmann /Marenholtz	$\sigma_F = C_1 + C_2 \cdot \varphi$	
<b>Root function approaches</b>		
Kochendörfer	$\sigma_F = C_1 + C_2 \cdot \sqrt{\varphi}$	Face-centered cubic metals
<b>Potential approaches</b>		
Nadai / Reihle	$\sigma_F = C_1 \cdot \varphi^{C_2}$	
Ludwik / Hollomon	$\sigma_F = C_1 \cdot \varphi^{C_2} + C_3$	Un- and low alloyed steels
Swift / Krupkowski	$\sigma_F = C_1 \cdot (C_2 + \varphi)^{C_3}$	Body-centered cubic metals
Gosh / Reissner	$\sigma_F = C_1 \cdot (C_2 + \varphi)^{C_3} - C_4$	Austenitic steels
Landgraf	$\sigma_F = C_1 \cdot \left[ \frac{C_2}{C_3} \left\{ (C_4 + \varepsilon^{pl})^{C_3} - C_4^{C_3} \right\} + 1 \right]$	
<b>Exponential approaches</b>		
Voce	$\sigma_F = C_1 - (C_1 - C_2) \cdot e^{-C_3 \cdot \varphi}$	
Landgraf	$\sigma_F = C_1 + (C_2 - C_1) \cdot (1 - e^{-C_3 \cdot \varphi})$	
Hockett / Sherby	$\sigma_F = C_1 - (C_1 - C_2) \cdot e^{-C_3 \cdot \varphi^{C_4}}$	Aluminum
Reè	$\sigma_F = C_1 \cdot \varphi + C_2 - C_3 \cdot e^{-C_4 \cdot \varphi} - C_5 \cdot e^{-C_6 \cdot \varphi}$	
<b>Logarithmic approaches</b>		
Orowan / Golongrac	$\sigma_F = C_1 \cdot \ln(\varphi) + C_2$	
<b>Polynomial approaches</b>		
Pries	$\sigma_F = C_k \cdot \varphi^k + \dots + C_2 \cdot \varphi^2 + C_1 \cdot \varphi^1 + C_0$	

## 2.4.2 Identification Methods for acquiring large strain flow curves

The maximum equivalent plastic strain that is generated in mechanical joining is well beyond the maximum uniform strain as measured in a uniaxial tensile test. As a consequence, the uniaxial tensile test is of limited usefulness to acquire the large strain flow curve. As already mentioned, one could opt to extrapolate the pre-necking strain hardening, but this may or may not be valid depending on the chosen hardening law. A better approach is to acquire experimental data at large plastic strains that can be used for improving the fitting quality in the post-necking regime. Several material tests and identification strategies have been proposed to deal with this problem (CHER19; COP11; COP14c; KIM13; KNY17; MER09; MUL15; POU20; TRAP18). The studies on large strain flow curve identification can be divided in three main categories, see Figure 13:

1. Homogenous material testing;
2. Homogenous material testing of pre-strained materials;
3. Heterogeneous material testing using an inverse method.

The first category relies on specimens that deform homogeneously beyond the point of maximum uniform strain. The hydraulic bulge test is a good example: at the top of the dome a balanced biaxial tensile stress state prevails throughout the entire experiment. The homogeneity in such test enables to analytically derive the stress and strain state required for constructing the flow curve. To this end, it is often required to make assumptions regarding the material behaviour (e.g. plastically isotropic material), the level of homogeneity and the boundary conditions. Other examples belonging to this category are: the simple shear test, the in-plane torsion test and the uniaxial tube expansion test. In the latter material tests, the specimens are designed in such a way that a homogeneous deformation occurs in the measurement gauge. The stack compression test and the plane strain compression test are treated as homogenous material tests. However, in these tests, friction cannot be avoided and the question arises whether the deformation is homogenous. This should be carefully checked if these tests are applied. If the homogeneity is not affected, it should be checked if compensation for friction is required. The crux of the problem with compensation, however, is that one has to determine the frictional condition to enable compensation. As opposed to conventional friction testing methods on sheet metal, however, friction in joining by forming is characterized by high contact pressures, small sliding lengths and large plastic deformation of the sheet metal.

The material tests in the second category rely on homogenous testing of pre-stained materials. The early work of Sevilanno et al. [SEV80] exemplifies this approach: the wire drawing process is used to pre-strain the wire to large plastic strain. The standard tensile test is then used to determine the flow behaviour. By conducting several experiments with different amounts of plastic strain, the large strain flow curve can be reconstructed. The major criticism here is the discrepancy between the testing conditions. Indeed, wire drawing used to pre-strain the samples comes with large strain rates, while the standard tensile test is conducted under quasi-static testing conditions. The discrepancy in test conditions is potentially biasing the identified hardening behaviour. The CBT test [POU20] is also recently proposed in this category. Finally, to probe large plastic strains, the last category allows for heterogeneous deformation in the gauge area. The most popular approach here is to extract the information hidden in the diffuse neck of a tensile test. Several techniques exist to do so. For example, the post-necking hardening curve can be extracted from the diffuse neck during a quasi-static uniaxial tensile test as proposed by Coppieters et al. [COP11]. A disadvantage of the inverse approach is that it is confined to the identification of a phenomenological hardening law. Table 4 shows the characteristics of the plastic deformation imparted by the material tests enabling to acquire the strain hardening of sheet metal. Comparing tables 1 and 2 shows that - in terms of magnitude of imparted strain - the in-plane torsion test and the plane strain compression test are comparable with the imparted strains in joining by forming. None of the material tests

listed in Table 3 enables to identify the post-necking strain hardening at a comparable strain rate. In terms of deformation mode, it is clear that each material test comes with a specific deformation mode which is not necessarily representative for the predominant deformation mode in joining by forming. Moreover, conventional sheet metal material testing is confined to plane stress conditions while joining by forming generates a 3D stress state.

In summary, there is a discrepancy between the characteristics of the imparted plastic deformation by joining by forming and conventional sheet metal material tests. If the material can be considered plastically isotropic, it would be sufficient to characterize the flow curve using a material test enabling to probe large plastic strains. However, many shell-like materials exhibit significant plastic anisotropy. Joining by forming simulations are confined to plastically isotropic material models since plastic anisotropy of the sheet metal can be ignored in predicting the metal flow. Plastic anisotropy of the metal, however, cannot be ignored in the material test used to identify the post-necking strain hardening. Therefore, it is considered to be good practice to select a material test resembling the conditions (predominant deformation mode, strain rate,) in joining by forming.

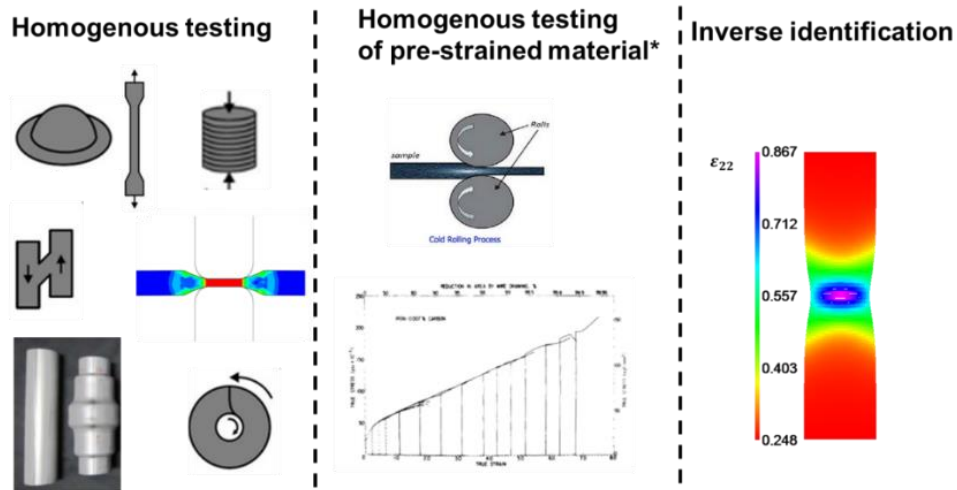


Figure 13: Identification of the large strain flow curve of sheet metal. Homogenous testing, Homogenous testing of pre-strained material and Inverse Identification

Table 4: Characteristics of the plastic deformation imparted by the material tests

Material tests	Predominant deformation mode	Typical order of magnitude of imparted strain	Order of magnitude of strain rate ( $\frac{1}{s}$ )	Remarks
Tensile test	Axisymmetric elongation	0.2-0.3	$10^{-5} \frac{1}{s} \rightarrow 10^2 \frac{1}{s}$	Decreasing strain rate up to max uniform strain
Stack Compression test	Balanced biaxial tension	0.5	$10^{-3} \frac{1}{s}$	Test protocol is not standardized
In-plane torsion test	Shear	1 to 3	$10^{-3} \frac{1}{s}$	Strain rate cannot be controlled
Plane strain compression test	Plane strain	2 to 3	$10^{-3} \frac{1}{s}$	Friction must be reduced
Post-necking tensile experiment	Uniaxial tension towards plain strain	0.7 to 1	$10^{-3} \frac{1}{s} \rightarrow 10^{-1} \frac{1}{s}$	Strain rate increases in the diffuse neck
Hydraulic bulge test	Balanced Biaxial tension	0.4 to 0.8	$10^{-4} \frac{1}{s}$	Strain rate controlled bulge test

### 3 Problem and research objective

Up to now there are no standards or technical guidelines for determining and applying flow curves required for simulation of joining by forming. Unlike the joining industry, the forging industry previously aimed at standardization of flow curve determination [IND08] to enhance predictive accuracy of simulations. For similar reasons, standardization of flow curve determination is required for the industry dealing with joining by forming.

Numerous variants of testing and evaluation methods can be found in literature and research projects. The studies typically examine test procedures and model assumptions from different angles. The diversity in methods and their utilization under different conditions leads to uncertainty and a limited reliability of the results. The latter is also inherently related to the complexity of numerical simulation for mechanical joining. The following examples illustrate the existence of unanswered research questions in joining by forming.

The left panel of Figure 14 illustrates the effect of material anisotropy and imposed stress state on the strain hardening behaviour of EN AW-6016 T4. It can be inferred that the obtained strain hardening behaviour shows differences depending on the adopted material test (tensile or upsetting test). Clearly, the identified material behaviour depends on the imposed stress state due to plastic anisotropy. Obviously, the discrepancy observed in the left panel of Figure 14 scales with the level of anisotropy and theoretically disappears for plastically isotropic materials. The evaluation of a flow curve is normally restricted to the range where damage starts or plastic instability sets in. Conventionally, flow curves for larger true plastic strains (required for FE simulation) are obtained by extrapolation of measured strain hardening data. However, extrapolation of flow curves can cause remarkable errors since it depends on the a priori chosen hardening law. The right panel of Figure 14 shows a large discrepancy as a result of extrapolation using two different hardening models. The diagram illustrates flow curves determined by tensile and upsetting tests and the extrapolation into the post-necking regime is performed using Ludwik and Hollomons model and Hockett and Sherby's model, respectively.

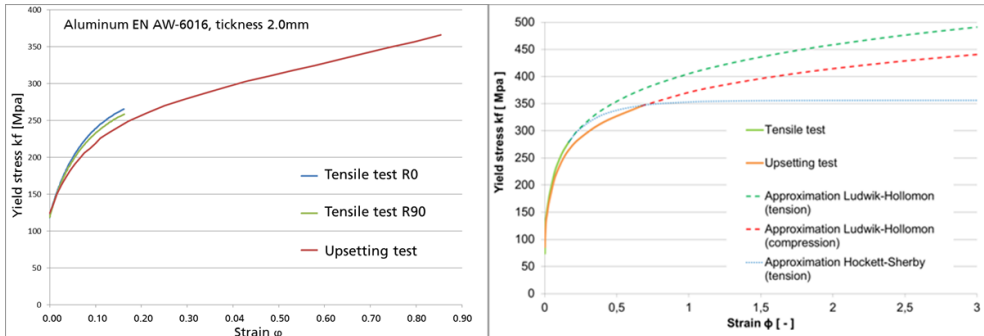


Figure 14: Comparison of aluminum EN AW-6016 flow curves between tensile and upsetting test; left: influence of anisotropy, right: influence of approximation approaches for flow curve extrapolation

FE models of mechanical joining operations put specific demands on the quality of flow curve description. Ideally, the material test mimics the situation of the actual joining process, i.e. similar stress/strain states are probed during material testing. Additionally, the same plastic strain levels are preferably probed. From an experimental point of view, however, probing plastic strains of the order 2-3 and simultaneously identifying the strain hardening of sheet metal is very difficult. As such, extrapolation will likely be required, however, the uncertainty of this process can be minimized by enlarging the range on which the extrapolation is based.

On the other hand, ultra-thin sheet metal materials and potentially strong anisotropic characteristics entail specific experimental challenges. Below examples of clinching and self-pierce riveting processes are discussed to illustrate these issues.

Mechanical joining processes are often characterized by excessive material deformations, e.g. in the neck and the bottom of a clinched joint. True plastic strains up to  $\varphi \sim 2$  are generated as shown in the right panel of Figure 15. For these areas it could be essential to control the material damage..

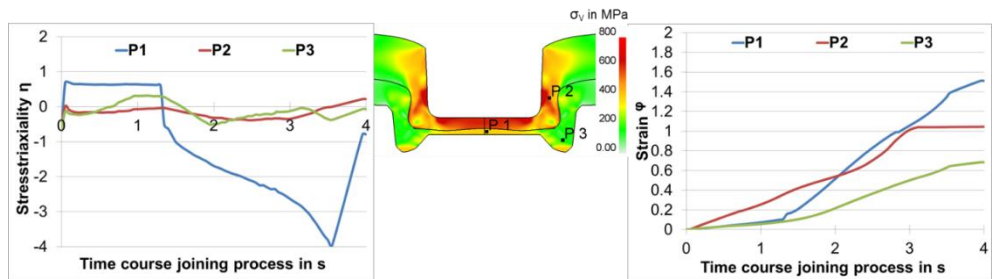


Figure 15: Local and transient stress state for clinched joint EN AW-7021 T4 ( $t = 2.0$  mm) in EN AW-6016 T4 ( $t = 1.2$  mm)

The left panel of Figure 15 shows for point P1 of the clinched joint the stress-state evolution which exhibits a transition from a pure tensile state to a complex compression. For this case influences of stress triaxiality on yield stress and, if necessary a kinematic hardening model to cope with stress reversal, should be considered.

Large true plastic strains will be achieved by joining technologies which employ a cutting element like self-pierce riveting. In these processes, plastic yielding occurs until strains are on the limit of the forming capacity of the material. Simulation of material separation or the evaluation of crack initiation in joining parts requires additional numerical expertise.

Figure 16 demonstrates the influence of flow curve variation on the calculation results for self-pierce riveting. Three strain hardening models for joining two aluminum EN AW-6016 T4 sheet metals with thickness  $t = 2.0$  mm are adopted. In addition, different material tests (tensile test and upsetting test) were used to calibrate the strain hardening models, see Figure 14.

It can be seen from Figure 16 that the different flow curves affect the simulation accuracy in terms of the final geometry (left) and the process graph (right). Significant strain hardening yields a strongly compressed rivet along with a strong spreading of the rivet foot. This leads to deformations in the rivet potentially causing cracks. Moreover, the sheet strength and the modified rivet diameter potentially influence the joint strength. The fundamental characteristic “minimal sheet thickness” beneath the rivet foot alters correlatively with the joint geometry. Remarkable is the fact that the dimension of the interlock between rivet foot and die-sided sheet metal – a common equivalent to joint strength – will be hardly affected. Also a significant influence on the joining force can be seen. Because the flow curve has a relevant influence on the state of stress, the computed material separation is also shifted. These examples show that an appropriate flow curve is one essential ingredient for the quality of simulation models in joining by forming.

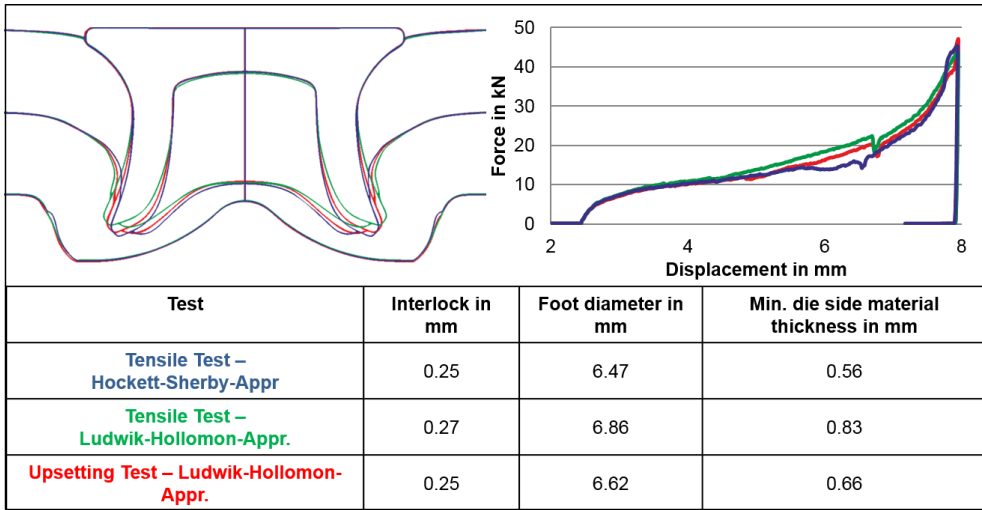


Figure 16: Simulation results for the self-pierce riveting process with varying material tests and flow curve approximations

In clinch forming true plastic strains of the order of 2-3 are not unusual and stress-strain data far beyond the maximum uniform strain have to be available for the numerical analysis. Figure 17 shows a cross section of a clinched joint. In general, the static strength of such a joint primarily depends on the amount of interlock (see red box) and the material state (stress levels) after joining in the neck of the joint (see dashed black box). Additionally, analytical calculations of the static strength [COP12] and fatigue life [SU15] are often based on geometrical parameters of the cross section. In [MEC16] it has been shown that the dominant fatigue failure mechanisms in clinching are associated to fretting. The latter implies that a small relative displacement present after forming is detrimental with respect to the fatigue resistance of the joint. As such, an accurate prediction of the final geometry and material state after clinch forming is of utmost importance to assess the quality and strength of the joint.

Figure 18 shows that the calculation of the interlock (red box in Figure 17) is sensitive to the strain hardening model. Two common hardening laws (Swift and Voce) were calibrated based on a multi-layered upsetting test while the material was assumed to be plastically isotropic. The difference between these two hardening models only becomes apparent at high plastic strains. Using a Voce type hardening law it is assumed that strain hardening becomes negligible at higher strains while a Swift law assumes that strain hardening continues. Figure 19 shows the interface in the interlock region of the two sheets obtained by an axisymmetric FE model. It can be inferred from this figure that the use of the Voce model causes a slightly larger interlock compared to the use of the Swift law. This figure shows that the metal flow in the interlock region is influenced by the adopted hardening law: a difference of approximately 36 % in the interlock is observed. The effect is even larger if the hardening laws are calibrated using a standard tensile test which only provides fitting data up to maximum uniform strain.

The accuracy of the plastic material behaviour determines the accuracy of the calculated material state. The neck region Figure 17 is probed during a single lap shear test. As such, the accuracy of strength simulations is sensitive to the material state after forming. The latter is shown in Figure 19. The left panel shows different hardening models while the right panel shows the shear strength prediction using two different hardening models.

It can be concluded that in clinch forming simulations attention must be paid to the identification of the strain hardening of the sheet at large plastic strains.

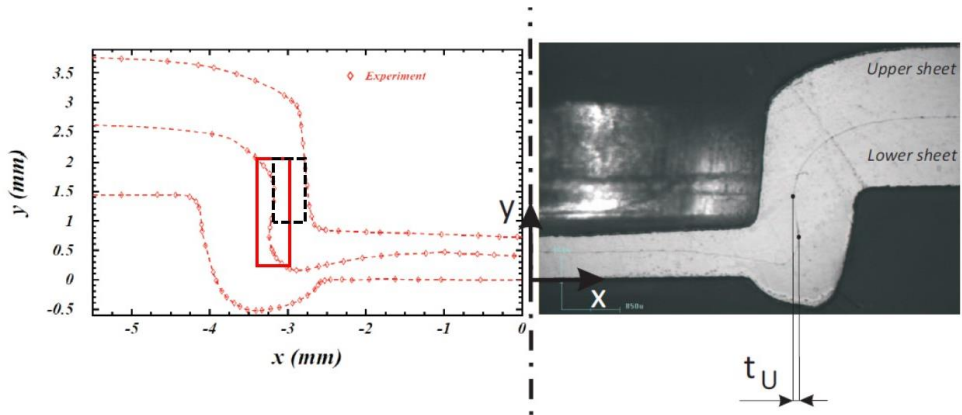


Figure 17: Single-stroke non-cutting round clinched joint. Material DC05, initial thickness 1.15 mm. Left Panel: contour measurement. Right panel: encapsulated cross-section.

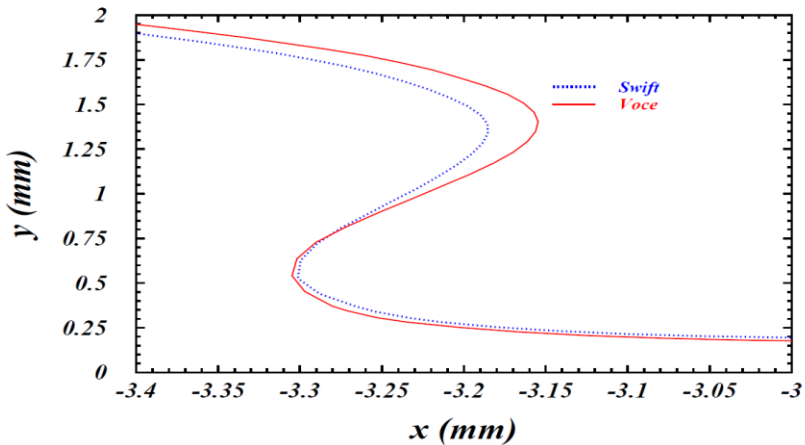


Figure 18: Final interface in the interlock region between upper and lower sheet calculated using different strain hardening models

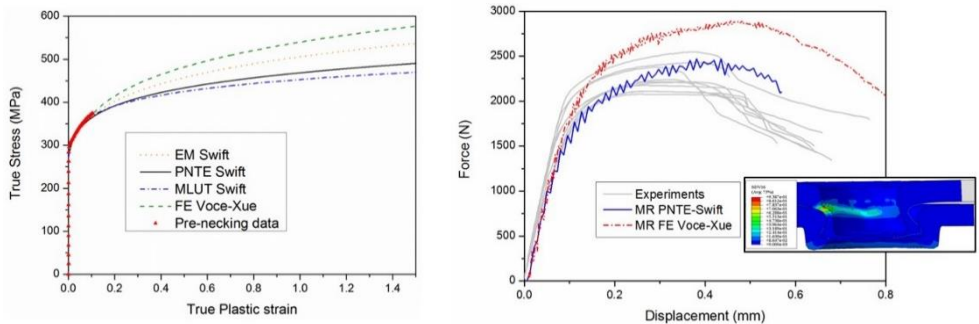


Figure 19: Left panel: strain hardening models identified using different methods. Right panel: sensitivity of the shear lap simulation with respect to the hardening model

Another challenge for mechanical joining is material data determination of auxiliary joining parts such as self-pierce rivets. The small geometry of the rivets and the comparatively large hardness puts high demands on the testing technology. Indeed, large testing forces are required combined with suitable devices to measure small displacements and geometries. The most straightforward method is the Finite Element Model Updating (FEMU) technique [DEN16] by a compression test on the rivet using hardened smooth anvils. This is complicated by frictional conditions which need to be known or treated as unknowns. The FEMU technique relies on the minimization of the discrepancy between the simulation and the experiment (e.g. the force-height reduction) by modifying the unknown strain hardening model. The advantage of this method is that it enables to mimic similar conditions in the rivet as the actual forming operation. This technique has been recently applied to identify the local strain hardening behaviour in blind rivet nuts [VAN16].

Currently, FE simulation of mechanical joining processes are usually performed assuming isotropic material models. Although several researchers [COP12], [SAB08], [HAH03] claimed that plastic anisotropy is of minor importance in clinch forming simulations, it is not clear which level of anisotropy can be ignored safely. The material model parameters are predominantly obtained through tensile testing. Extrapolation based on pre-necking data is not accurate and yields deviations between experiment and simulation. Dedicated material tests and inverse calibration can enhance the simulation accuracy. The latter strategy, however, is time-consuming and cost-intensive as well as it generates unique results. As such, this trial-and-error approach is inadequate for prospective simulation tasks which become increasingly complex due to a variety of factors in a multi-material context. To limit the experimental effort for validating numerical calculations, more accurate and reliable data is required. The latter can be achieved by selecting the correct material testing procedure prior to numerical calculation. Of course, the adopted material models have to describe physical characteristics as accurately as possible, but they should also be properly calibrated.

The research project targets to manage the determination of flow curves tailored for the requirements in mechanical joining. Hence, the study has the goal of making a contribution to quality improvement and control of simulation results in joining by forming.

The solutions for these research questions should have a high potential for industrial valorisation. Indeed, from an industrial point of view, the proposed procedure should be driven by the amount of experimental effort to obtain an acceptable level of accuracy. Obviously, the primary aim in industry is to reduce the time period to bring a new material or product to market.

The approaches for flow curve determination will be based on investigations on two commonly applied joining by forming techniques, namely clinching and self-pierce riveting. These two techniques are considered to be representatives of joining-by-forming family. Additionally, the selected joining techniques are frequently applied in sheet metal industry guaranteeing the industrial relevance of this project. New joining challenges in sheet metal industry can be tackled with clinching and SPR provided that adaptive and innovative designs can be derived with aid of simulation tools. The latter process would clearly benefit from standardization with respect to material identification.

## 4 Materials, equipment and tools

### 4.1 Investigated materials

The project is confined to sheet or thin-walled materials with a thickness equal or smaller than 2 mm. In order to be able to draw general conclusions, a variety of material families are considered. The following major categories are distinguished: large ductility (DC04), limited ductility (EN-AW 6082 T6), anisotropic plastic material behaviour (DC04), higher strength steels (CR330Y590T-DP) and standard aluminum sheets (EN AW-5182). In the mechanical properties of the considered materials, which were determined by a standard tensile test (DIN EN ISO 6892-1) are shown in Figure 20.

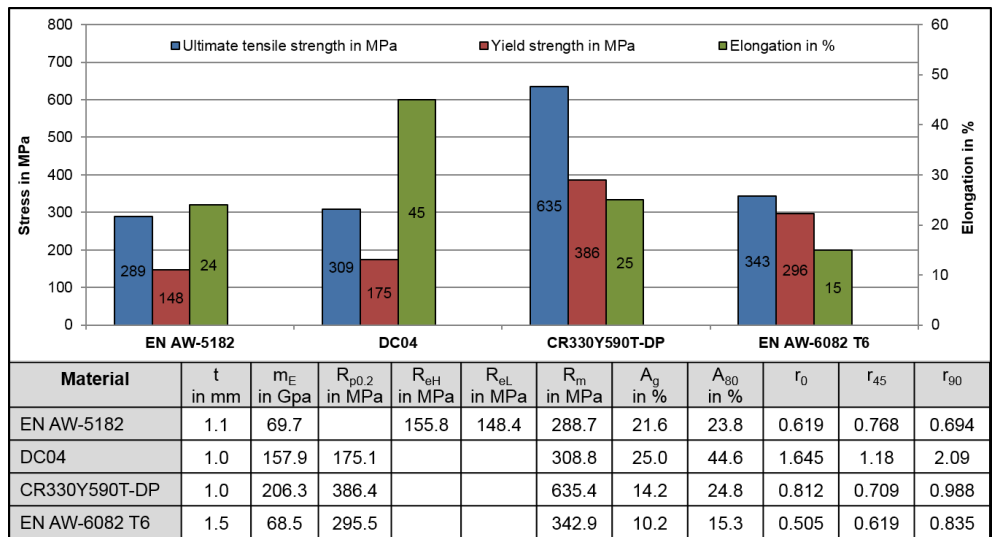


Figure 20: Mechanical properties for the considered materials

Table 5 shows the considered material combination for clinching and SPR. For both joining methods the same material combinations are considered. To determine the influence of the flow curve determination for each material type, the materials are considered separately at 3 material combinations. Only for material combination No. 3 a mixed combination is considered.

Table 5: Considered material combination for each joining method

Joining Method	No.	Punch-side part	$t_1$ in mm	Die-side part	$t_2$ in mm
Self-pierce riveting / Clinching	1	EN AW-5182	1.1	EN AW-5182	1.1
	2	DC04	1.0	DC04	1.0
	3	CR330Y590T-DP	1.0	EN AW-5182	1.1
	4	EN AW-6082 T6	1.5	EN AW-6082 T6	1.5

## 4.2 Joining setup

For experimental joining investigation of the SPR and clinching process at the Fraunhofer IWU a test stand with an electromechanical press is used (Figure 21). In order to ensure the best possible coaxiality between the setting tool and the die, the joining tools are arranged in a column guide frame in the centre of the press.

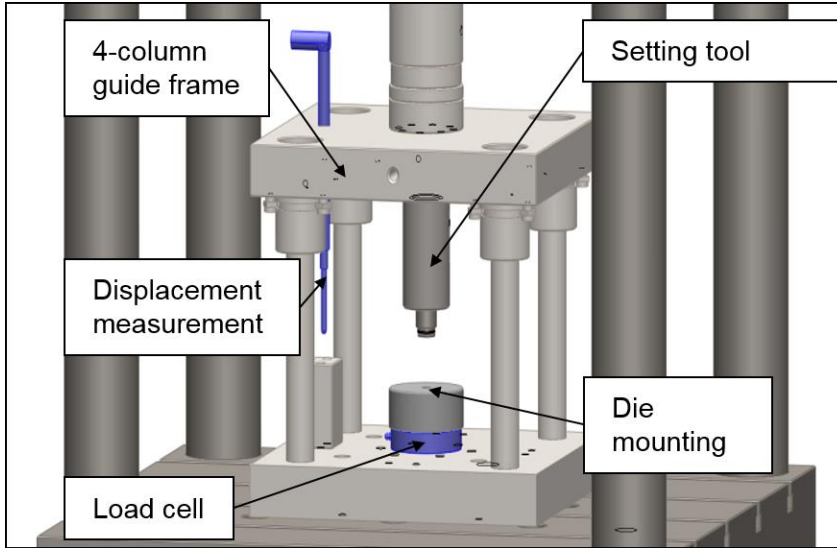


Figure 21: Test stand for the joining experiments

The exact measurement of the joining forces and punch displacement is carried out by an external, inductive displacement transducer from HBM GmbH as well as a piezoelectric load cell from Kistler Instrumente AG.

## 4.3 Joining elements and tools

### 4.3.1 Self-pierce riveting

There is a big variety of rivets and die geometries which can be used for SPR. Figure 22 shows the dimensions of the in this project used joining elements and tools.

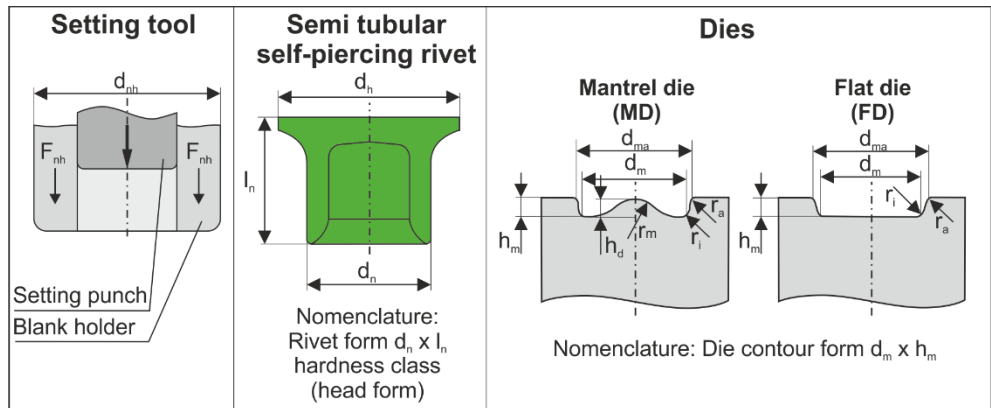


Figure 22: Dimensions for tools and rivets used for SPR

The in this project used variable and constant process parameters for rivets, dies and setting tool can be found in Table 6.

Table 6: Used process parameters for SPR

Element	Explanation	Used
Semi-tubular self-piercing rivet $d_n \times l_n$	Countersunk head Hardness class $d_n$ Shaft diameter $d_h$ Head diameter $l_n$ Rivet length Rivet material Rivet coating	SK H4 $d_n = 5.3\text{mm}$ $d_h = 7.8\text{mm}$ $4.0\text{ mm} \leq l_n \leq 5.0\text{ mm}$ Steel Almac
Die $d_m \times h_m$	$d_a$ Outer die diameter $h_m$ Die contour depth $d_m$ Die contour diameter	$d_a = 18\text{mm}$ $1.2\text{ mm} \leq h_m \leq 1.5\text{ mm}$ $9.0\text{ mm} \leq d_m \leq 10\text{ mm}$
Setting tool	$d_{nh}$ Blank holder diameter $F_{nh}$ Blank holder force $v_s$ Setting speed	$d_{nh} = 18\text{ mm}$ $F_{nh} = 4 - 6\text{ kN}$ $v_s = 1; 20; 50\text{ mm / s}$

### 4.3.2 Clinch forming

Similar to SPR, a large number of different tool geometries are also possible for clinching. Figure 23 shows the different parameters.

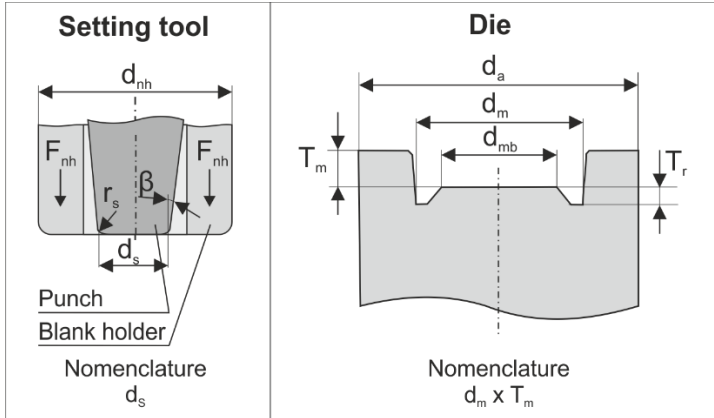


Figure 23: Dimensions for tools used for Clinching

An overview of the constant and variable process parameters for the clinching investigations is shown in Table 7.

Table 7: Used process parameters for clinching

Element	Explanation	Used
Punch $d_s$	$d_s$ Punch diameter $r_s$ Punch radius $\beta$ Punch angle	$d_s = 5.4$ mm $r_s = 0.3$ mm $5^\circ$
Die $d_m \times T_m$	$d_a$ Outer die diameter $T_m$ Die contour depth $d_{mi}$ Die contour diameter	$d_a = 14$ mm $1.2 \text{ mm} \leq T_m \leq 1.4$ mm $d_m = 8$ mm
Setting tool	$d_{nh}$ Blank holder diameter $F_{nh}$ Blank holder force $v_s$ Setting speed	$d_{nh} = 18$ mm $F_{nh} = 4 - 6$ kN $v_s = 1; 20; 50$ mm / s

## 5 Experimental joint analysis

In order to validate the numerical simulations of clinch forming and SPR, several joints that were produced for the selected joining techniques will be subjected to a cross-sectional analysis. Firstly, the characteristic dimensions of the joints, as specified in section 2 of this report, will be measured. Additionally, a contour measurement of each joint type will be conducted and calibrated. This calibrated joint contour can be used to assess the predictive accuracy of the FE model.

The considered materials and the used equipment and tools are described in chapter 4. For each material combination, joints were made by using different joining speeds.

### 5.1 Procedure

All produced joints were cold embedded using a transparent two-component epoxy resin. After embedding, the specimen was grinded and polished up to the mid-section reference point was reached, as shown. Then, the polished joints were metallographically investigated and all characteristic joint dimensions were measured at a magnification of 50. For each joining parameter combination and joining speed, five specimens were analysed, and an average result of geometric value (e.g. interlock, minimum material thickness) could be determined.

In addition to measuring the geometrical parameters, the contour of the joining points was also captured for later comparison with the numerical calculation. These measurements can be automatic or manually performed by using a digital profile projector with bottom and top lightening, as illustrated in Figure 24.

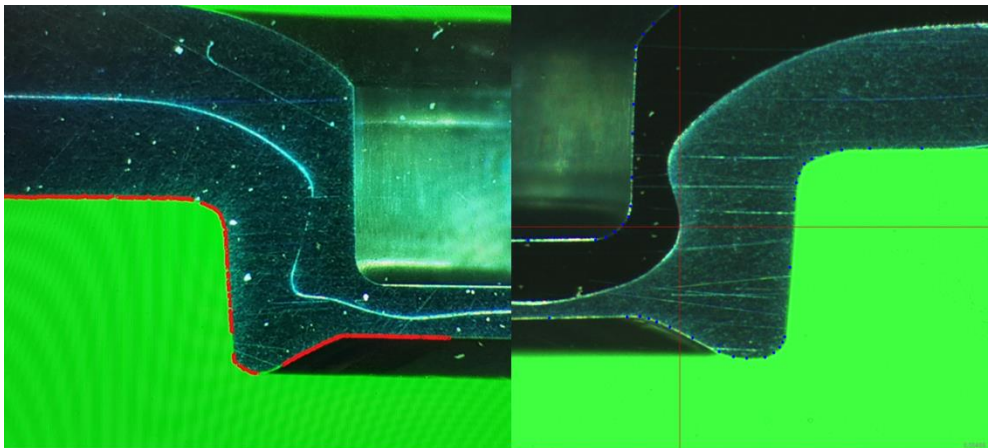


Figure 24: Automatic (left) and manual (right) contour measurement of a clinched joint.

After contour measurement, all data points can be exported as a comma-separated values or CSV data file. This data will be further processed by a calibration procedure and the final cross section profile of the joint can be determined and used for validation of the FE-analysis.

The calibration procedure is performed in order to reduce the error made by polishing and grinding the cross sections. Ideally, each joint shall be measured at a plane, exactly through the centre-plane of the joint. However in reality, a deviation on the cross section is possible due to the limited deviation on the cross section plane location parallel to the center-plane of each joint.

For SPR joints, it is assumed that the diameter of the rivet head does not change after the joining process. Therefore, the diameter of the rivet head will be used to calculate a linear calibration value in the X-direction. This is performed in order to fit the measured contour of the data points, located on the rivet head, with the actual rivet head dimensions. In the Y-direction, a deviation is possible due to a deviation of the cross-section plane. However, the calibration cannot be assumed to be linear and furthermore, no reference value is available in this direction to calibrate the measured data.

For SPR, the contours of the top-sheet (x3 bodies), bottom sheet (x1 body) and the rivet (x1 body) were detected. In order to calibrate the measured data points in the X-direction, two additional reference points P1' and P2' were measured. After contour measurement, the X-value of all data points are modified in order to achieve a measured rivet diameter equal to the original rivet diameter of 7,77mm.

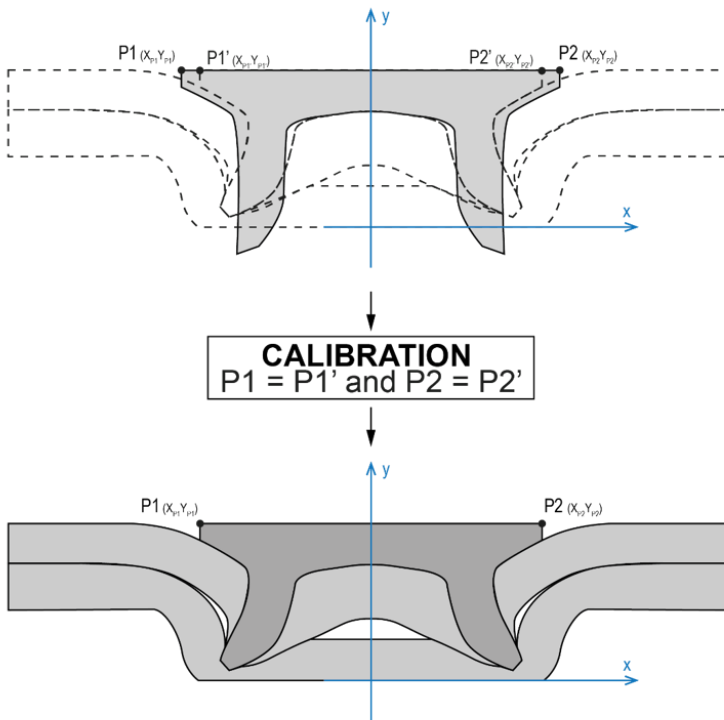


Figure 25: Contour measurement and calibration of an SPR connection.

Each contour measurement consists of multiple data points along the edge of the measured body (sheet or rivet). Through these points a best fit curve is plotted.

For clinched joints, the geometric dimensions of the punch tool will be used to calculate a linear calibration value in the X-direction. This is performed in order to fit the measured contour of the data points, located on the indent produced by the punch tool, with the actual punch tool dimensions. In the Y-direction, no calibration is performed on the measured data points as these Y-values are independent of the cross-section plane location.

For clinching, the contours of the top-sheet (x1 body) and bottom sheet (x1 body) were detected. In order to calibrate the measured data points in the X-direction, two additional reference points P1' and P2' were measured. After contour measurement, the X-value of all data points are modified in order to achieve a measured diameter equal to the original punch diameter at the specific measured height. The diameter of punch tool at a given height, y, can be found by using the following equation:

$$D_{punch} = 2 \times (0,0375y + 2,7) \tag{1}$$

After the calibration value was calculated the XY-coordinate system was shifted down so that the new X'Y'-coordinate system has a zero point (0,0) in the middle of the top surface from the die tool used during joining.

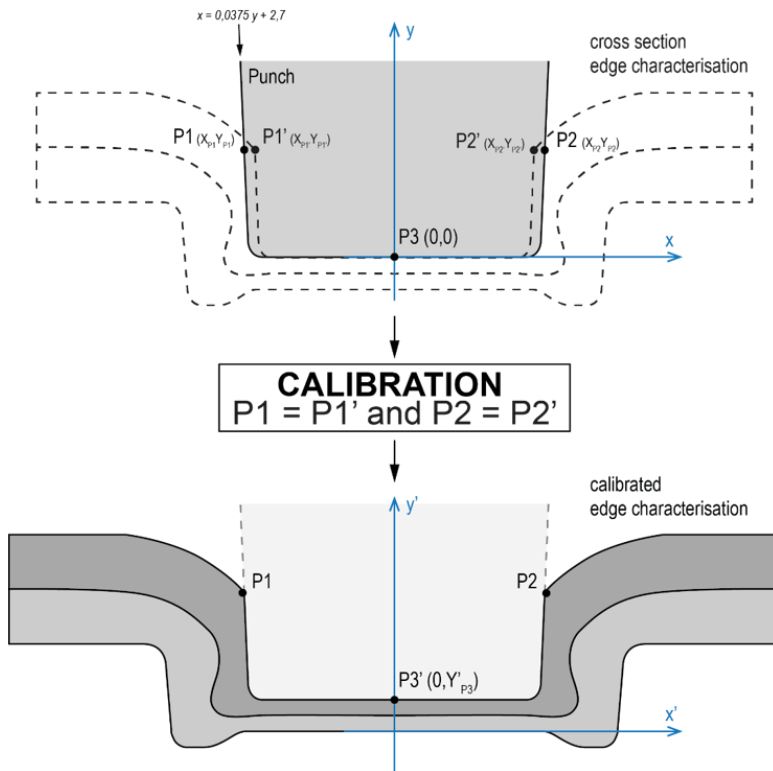


Figure 26: Contour measurement and calibration of a clinch connection.

Each contour measurement consists out of multiple data points along the edge of the measured body (top and bottom sheet). Through these points a best fit curve is plotted.

## 5.2 Self-pierce riveting

In the SPR tests, all material combinations were joined at setting speeds of 1, 20 and 50 mm/s and then evaluated by means of micrograph analyses. The results are shown in Figure 27 to Figure 30.

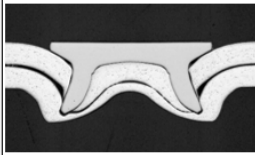
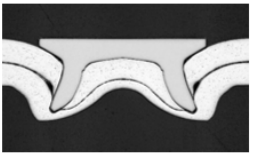
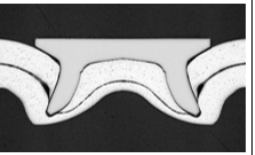
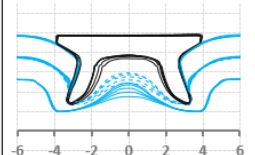
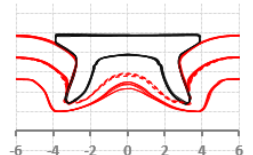
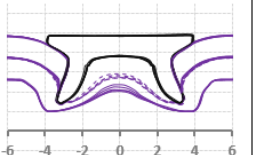
Process parameters			
Punch-side part:	thickness:		
EN AW-5182	1,1 mm		
Die side part:	thickness:		
EN AW-5182	1,1 mm		
Rivet:	C5.3 x 4.0 H4		
Die:	MD 9.5 x 1.8		
System:	Promess 70		
Setting force:	41 kN	41 kN	42 kN
Joining speed:	1 mm/s	20 mm/s	50 mm/s
Average values			
Number of joints:	5	5	5
Interlock:	$0.12 \pm 0.03$ mm	$0.08 \pm 0.02$ mm	$0.07 \pm 0.02$ mm
min. sheet thickness:	$0.26 \pm 0.03$ mm	$0.29 \pm 0.02$ mm	$0.31 \pm 0.01$ mm
Cross section			
			
Contour			
			

Figure 27: Results of the experimental joining analysis for SPR of EN AW-5182 ( $t = 1,1$  mm) in EN AW-5182 ( $t = 1,1$  mm)

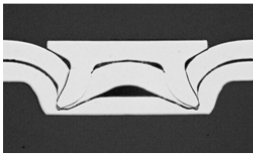
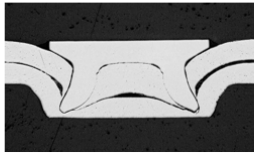
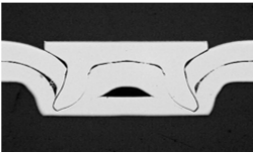
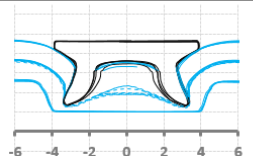
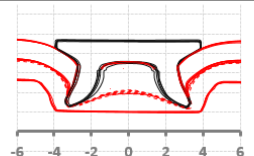
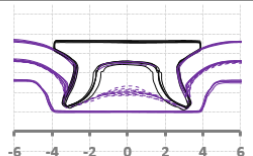
Process parameters			
Punch-side part:	thickness:		
DC04	1,0 mm		
Die side part:	thickness:		
DC04	1,0 mm		
Rivet:	C5.3 x 4.0 H4		
Die:	FD 9.0 x 1.5		
System:	Promess 70		
Setting force:	38 kN	38 kN	40 kN
Joining speed:	1 mm/s	20 mm/s	50 mm/s
Average values			
Number of joints:	5	5	5
Interlock:	0.06 ± 0,03 mm	0.09 ± 0.03 mm	0.09 ± 0.03 mm
min. sheet thickness	0.22 ± 0,04 mm	0.19 ± 0.04 mm	0.16 ± 0.07 mm
Cross section			
			
Contour			
			

Figure 28: Results of the experimental joining analysis for SPR of DC04 ( $t = 1,0$  mm) in DC04 ( $t = 1,0$  mm)

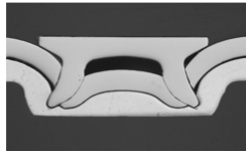
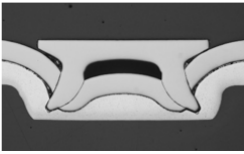
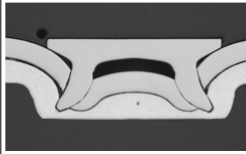
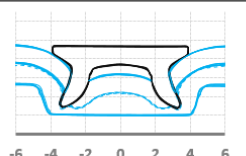
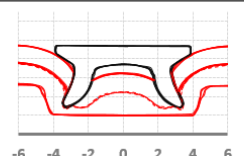
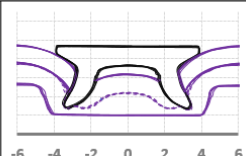
Process parameters			
Punch-side part:	thickness:		
CR330Y590T-DP	1,1 mm		
Die side part:	thickness:		
EN AW-5182	1,1 mm		
Rivet:	C5.3 x 4.0 H4		
Die:	FD 9.0 x 1.8		
System:	Promess 70		
Setting force:	37 kN	35 kN	36 kN
Joining speed:	1 mm/s	20 mm/s	50 mm/s
Average values			
Number of joints:	5	5	5
Interlock:	$0.18 \pm 0.03$ mm	$0.15 \pm 0.02$ mm	$0.16 \pm 0.01$ mm
min. sheet thickness	$0.28 \pm 0.01$ mm	$0.28 \pm 0.01$ mm	$0.26 \pm 0.01$ mm
Cross section			
			
Contour			
			

Figure 29: Results of the experimental joining analysis for SPR of CR330Y590T-DP ( $t = 1,0$  mm) in EN AW-5182 ( $t = 1,1$  mm)

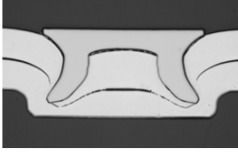
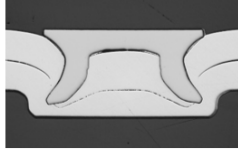
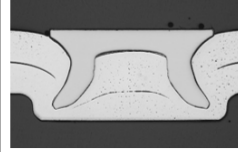
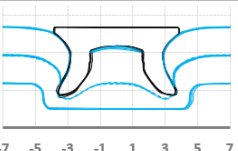
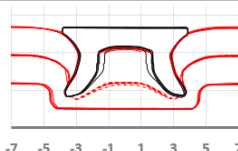
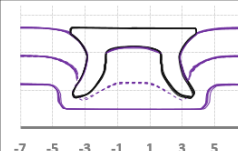
Process parameters			
Punch-side part:	thickness:		
EN AW 6082-T6	1,5 mm		
Die side part:	thickness:		
EN AW 6082-T6	1,5 mm		
Rivet:	C5.3 x 5.0 H4		
Die:	FD 9.0 x 1.2		
System:	Promess 70		
Setting force:	71 kN	73 kN	78 kN
Joining speed:	1 mm/s	20 mm/s	50 mm/s
Average values			
Number of joints:	5	5	5
Neck thickness, $t_n$ :	$0.17 \pm 0.03$ mm	$0.21 \pm 0.04$ mm	$0.22 \pm 0.06$ mm
Interlock, $f$ :	$0.51 \pm 0.03$ mm	$0.63 \pm 0.04$ mm	$0.58 \pm 0.06$ mm
min. sheet thickness:	$1.36 \pm 0.03$ mm	$1.32 \pm 0.05$ mm	$1.31 \pm 0.04$ mm
Cross section			
			
Contour			
			

Figure 30: Results of the experimental joining analysis for SPR of EN AW-6082 T6 ( $t = 1,5$  mm) in EN AW-6082 T6 ( $t = 1,5$  mm)

With all material combinations, good SPR joints with sufficient geometrical characteristics and without damage to the sheets or the rivet could be achieved. In order to enable the best possible comparison to the material tests with regard to the strain rates, the tests with a joining speed of 1 mm/s are used for the validation of the simulation models.

### 5.3 Clinching

In the clinching tests, too, all material combinations were joined at setting speeds of 1, 20 and 50 mm/s and then evaluated using micrograph analyses. The results are shown in Figure 31 to Figure 34.

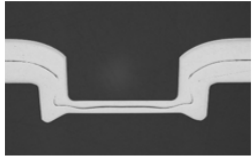
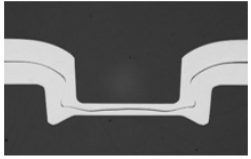
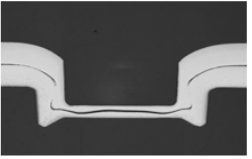
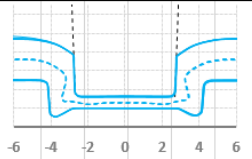
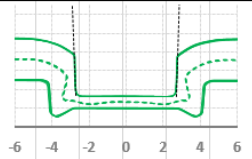
Process parameters			
Punch-side part:	thickness in mm:		
EN AW-5182	1.1		
Die side part:	thickness in mm:		
EN AW-5182	1.1		
Punch (dia.):	5,4 mm		
Die (dia. x depth):	8x1,4 mm		
System:	Promess 100		
Setting force in kN:	44	44	44
Joining speed:	1 mm/s	20 mm/s	50 mm/s
Average values in mm			
Number of joints:	5	5	5
Neck thickness, $t_n$ :	$0,46 \pm 0,03$	$0,48 \pm 0,031$	$0,47 \pm 0,032$
Interlock, $f$ :	$0,25 \pm 0,03$	$0,24 \pm 0,015$	$0,23 \pm 0,011$
Min. sheet thickness:	$0,22 \pm 0,02$	$0,19 \pm 0,021$	$0,21 \pm 0,022$
Bottom thickness, $t_b$ :	$0,61 \pm 0,013$	$0,59 \pm 0,011$	$0,61 \pm 0,012$
Cross section			
			
Contour			
			

Figure 31: Results of the experimental joining analysis for clinching of EN AW-5182 ( $t = 1,1$  mm) in EN AW-5182 ( $t = 1,1$  mm)

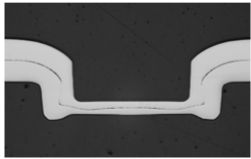
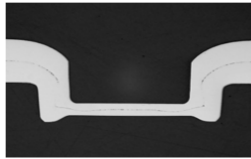
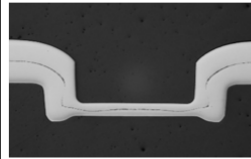
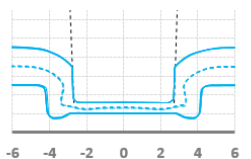
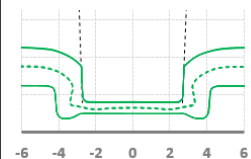
Process parameters			
Punch-side part:	thickness in mm:		
DC04	1.0		
Die side part:	thickness in mm:		
DC04	1.0		
Punch (dia.):	5,4 mm		
Die (dia. x depth):	8 x 1,4 mm		
System:	Promess 100		
Setting force in kN:	53	51	49
Joining speed:	1 mm/s	20 mm/s	50 mm/s
Average values in mm			
Number of joints:	5	5	5
Neck thickness, $t_n$ :	0,51 ±0,028	0,5 ±0,025	0,49 ±0,018
Interlock, $f$ :	0,15 ±0,02	0,16 ±0,025	0,16 ±0,017
min. sheet thickness:	0,21 ±0,008	0,2 ±0,014	0,21 ±0,006
Bottom thickness, $t_b$ :	0,6 ±0,016	0,57 ±0,015	0,59 ±0,017
Cross section			
			
Contour			
			

Figure 32: Results of the experimental joining analysis for clinching of DC04 ( $t = 1,0$  mm) in DC04 ( $t = 1,0$  mm)

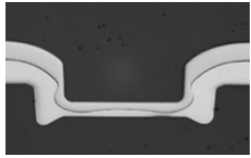
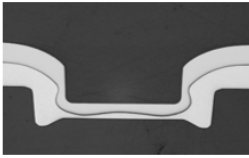
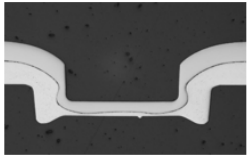
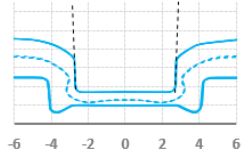
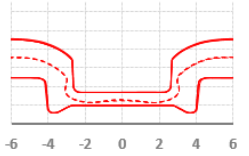
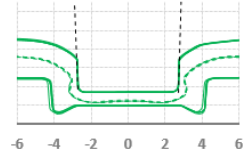
Process parameters			
Punch-side part:	thickness in mm:		
CR330Y590T-DP	1.0		
Die side part:	thickness in mm:		
EN AW-5182	1.1		
Punch (dia.):	5,4 mm		
Die (dia. x depth):	8 x 1,4 mm		
System:	Promess 100		
Setting force in kN:	53	50	50
Joining speed:	1 mm/s	20 mm/s	50 mm/s
Average values in mm			
Number of joints:	5	5	5
Neck thickness, $t_n$ :	$0,33 \pm 0,022$	$0,32 \pm 0,021$	$0,32 \pm 0,041$
Interlock, $f$ :	$0,14 \pm 0,04$	$0,12 \pm 0,016$	$0,12 \pm 0,023$
min. sheet thickness:	$0,15 \pm 0,017$	$0,13 \pm 0,01$	$0,11 \pm 0,01$
Bottom thickness, $t_b$ :	$0,7 \pm 0,02$	$0,7 \pm 0,012$	$0,7 \pm 0,01$
Cross section			
			
Contour			
			

Figure 33: Results of the experimental joining analysis for clinching of CR330Y590T-DP ( $t = 1,0$  mm) in EN AW-5182 ( $t = 1,1$  mm)

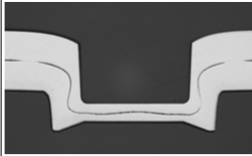
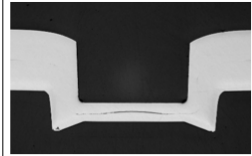
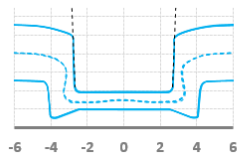
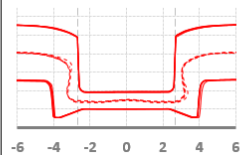
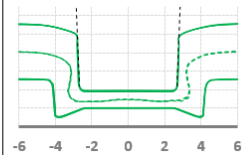
Process parameters			
Punch-side part:	thickness in mm:		
EN AW-6082 T6	1.5		
Die side part:	thickness in mm:		
EN AW-6082 T6	1.5		
Punch (dia.):	5,4 mm		
Die (dia. x depth):	8 x 1,2 mm		
System:	Promess 100		
Setting force in kN:	52	51	50
Joining speed:	1 mm/s	20 mm/s	50 mm/s
Average values in mm			
Number of joints:	5	5	5
Neck thickness, $t_n$ :	$0,43 \pm 0,03$	$0,43 \pm 0,044$	$0,42 \pm 0,032$
Interlock, $f$ :	$0,18 \pm 0,04$	$0,18 \pm 0,027$	$0,19 \pm 0,033$
min. sheet thickness:	$0,36 \pm 0,016$	$0,36 \pm 0,011$	$0,36 \pm 0,008$
Bottom thickness, $t_b$ :	$0,91 \pm 0,02$	$0,92 \pm 0,008$	$0,91 \pm 0,014$
Cross section			
			
Contour			
			

Figure 34: Results of the experimental joining analysis for clinching of EN AW-6082 T6 ( $t = 1,5$  mm) in EN AW-6082 T6 ( $t = 1,5$  mm)

With all material combinations, good clinch joints with sufficient geometrical characteristics and without damage to the sheets could be achieved. In order to enable the best possible comparison to the material tests with regard to the strain rates, the tests with a joining speed of 1 mm/s are used for the validation of the simulation models.

## 6 Simulation models of the joining processes

For SPR and clinching both 2D simulation models were built in Simufact V15 (Figure 35). The chosen parameters of the combined friction model were validated by numerical sensitivity analyses by fitting the calculated with the experimental joint contour and force-displacement curve for several SPR and clinching processes, which was done in a previous study [Fal19].

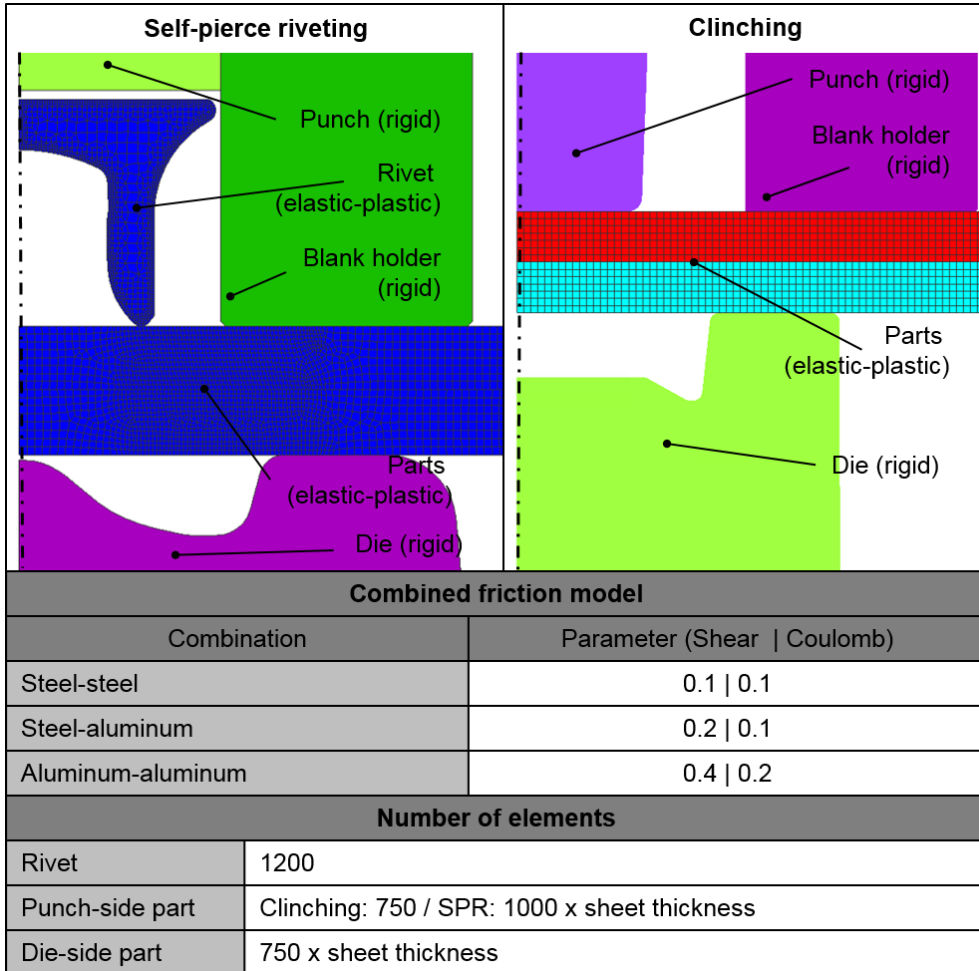


Figure 35: Simulation models for SPR and Clinching

The separation of the punch-sided sheet during the SPR process is realized by using a geometrical damage model. Thereby the elements in the area of material separation are deleted when the thickness of the sheet is below 0.1 mm. Although this model is not based on physical mechanisms, it has proven to be effective in practice. The sheets to be joined and the rivet are modelled with elastic-plastic deformation behaviour and all other objects are considered as rigid to reduce the calculation effort.

## 7 Material testing requirements for joining by forming

### 7.1 Plastic anisotropy

As already stated, joining by forming is usually simulated assuming a von Mises material solely requiring a large strain flow curve to account for strain hardening. Besides the fact that in the majority of the joining processes the plastic anisotropy does not manifest itself at the length scale of the joint, the use of an axisymmetric FE model inherently limits material modelling to J2 plasticity. In this regard, standard tensile tests are of limited usefulness because necking limits uniform deformation. Several experimental techniques have been developed (see chapter 2.4) to determine the large strain flow curve of sheet metal. In this regard, there are two issues:

1. These materials tests are typically dominated by a certain stress state and yield different results depending on the degree of plastic anisotropy.
2. Due to the small dimensions of the forming tools compared to the nominal thickness of the sheet metal, joining by forming must be regarded as a bulk forming process. The crux of the problem here is that the large strain flow curve is determined by material tests which subject the sheet metal to homogeneous plane stress conditions in the plane of the sheet.

The left panel of Figure 36 shows the results of a tensile test and a stack compression test on a low carbon steel exhibiting differential work hardening, the material (a low carbon steel) has an average  $r$ -value  $r_{\text{avg}} > 1.5$ . In essence, this means that the shape of the yield locus changes as a function of the amount of plastic deformation. It can be seen from Figure 36 that initial yielding in both experiments obeys the von Mises yield criterion. Indeed both the tensile test and the stack compression test yield a comparable yield stress. However, as deformation progresses, the difference between the flow stresses increases. Especially near equibiaxial tension the shape change of the yield locus is significant. If the flow curves stemming from the tensile test and the stack compression test are used to calibrate the von Mises yield criterion, one ends up with a situation shown in Figure 37. At a certain plastic equivalent strain, the von Mises yield criterion calibrated using the stack compression test will predict a much larger absolute stress level than the one calibrated using the tensile test data.

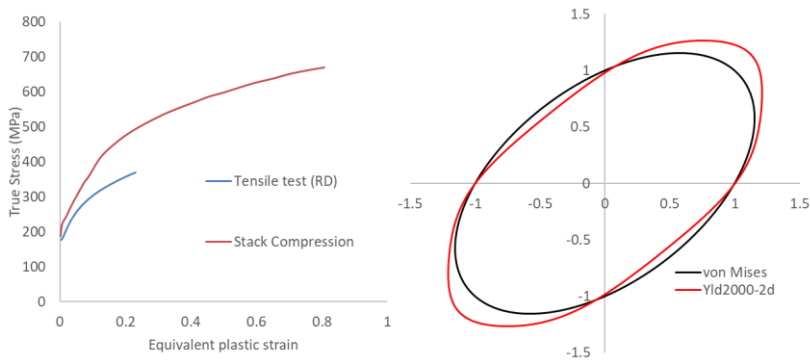


Figure 36: Flow curves obtained a low carbon steel by the tensile test and the stack compression test (left). The effect of differential work hardening on the yield locus after a 0.05 true plastic strain (right)

Figure 38 shows the extrapolated hardening behavior from the tensile test and the stack compression test used to simulate the clinch forming process. The simulation results are shown in Figure 39. In general, it can be concluded that if the flow curve exhibits enough strain hardening, the metal flow is not strongly affected. However, it can be inferred from the process graph (right panel Figure 39) that the absolute stress levels within the joint are strongly affected by the choice of the material test.

With regard to plastic anisotropy, the following conclusions can be drawn for joining by forming:

1. Plastic anisotropy has in general in marginal influence on the prediction of cross-sectional contours for joining by formig. In other words, the plastic anisotropy does not have a strong effect on the metal flow.
2. Plastic anisotropy has a clear effect on the stress levels (or more general: the material state) within the simulated joint. This can be indirectly assessed by the process graph.
3. Given that commercial FE codes are usually confined to axisymmetric FE modelling of the joining processes, and as a consequence limited to J2 plasticity, and that sheet metal often exhibits anisotropy, it is a good idea to use a material test that resembles the dominating stress state in the joining process.

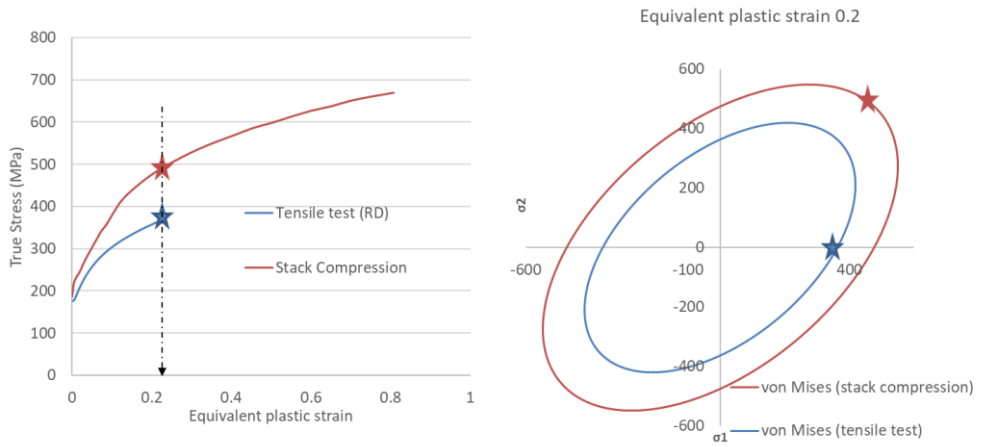


Figure 37: Stress state fitting of the von Mises yield criterion

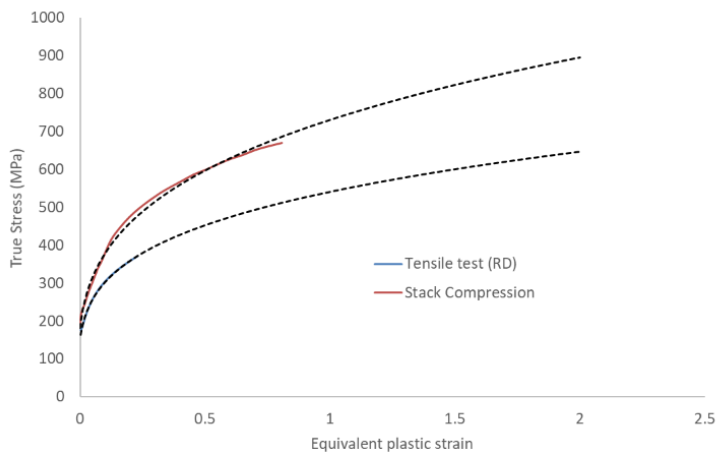


Figure 38: Flow curves used for assessing differential work hardening in clinch forming

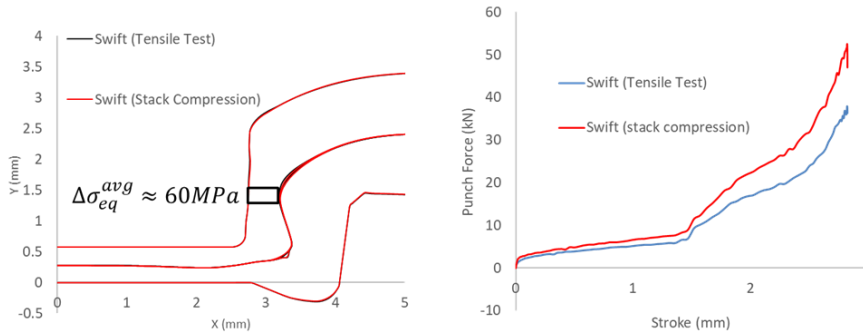


Figure 39: Effect of differential work hardening in clinch forming. Cross-section (left) and process graph (right)

## 7.2 Large strain flow curve

In this section, we want to scrutinize the requirements with respect to the large strain flow curve required for accurately simulating the clinch forming process. Obviously, it is better to use a material test that enables to probe very large plastic strains. However, what would be the lower bound in this regard to enable proper fitting of the phenomenological hardening law? In addition, how important is the choice of the hardening law? To this end, a virtual experiment (VE) is conducted using a reference hardening behaviour, an overview of the methodology is shown in Figure 40. The VE is created using FE software yielding synthetic data enabling to derive guidelines with respect to the large strain flow curve. The black solid curve shown in Figure 41 the reference flow curve (Swift type). The latter data is considered as the ground truth here. In practice, one does not know which hardening law is the best choice. As such, we have deliberately chosen a different hardening law, namely Voce's hardening law. The latter hardening law was fitted to different strain ranges in accordance with typical material tests. This yields three different hardening behaviours which can be used to assess the importance of

- i) the chosen hardening law; and
- ii) the importance of the strain level that is probed in the material test.

Obviously, the post-necking strain hardening behaviour of the flow curves differs significantly, see Figure 41. In addition, it can be inferred from Figure 42 that large differences are present in the pre-necking region.

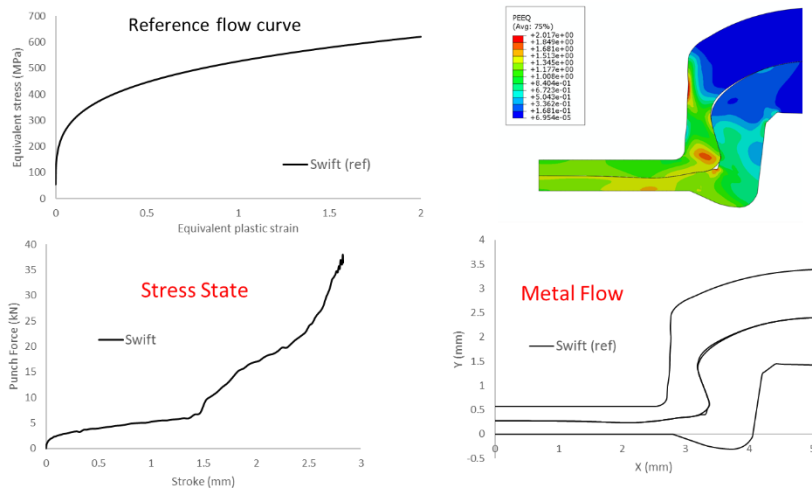


Figure 40: Concept of the Virtual Experiment to derive requirements for the large strain flow curve in clinch forming

Figure 43 shows the simulation results: the predicted contours of the joint and the process graph. The following conclusions can be drawn:

1. Pre-necking accuracy of the adopted hardening law is not of crucial importance;
2. Although strains in the order of 2 are generated, it is sufficient to probe strains of the order 0.7 in the material test; Figure 41 shows that when the Voce law is fitted to strain data up to 0.7, the metal flow and the process graph are relatively well reproduced. The stress state within in neck region, however, is underestimated by approximately 70 MPa. The choice of the hardening law is not crucial if the fitting range is large enough, preferably up to a true plastic strain of 0,7;
3. The absolute stress level in the neck is largely depends on the post-necking strain hardening. This is important when the simulation results are used for strength assessments using the solution variables from the forming simulation.

The Voce law is a saturation type of hardening law while Swift's hardening law exhibits a monotonic increase of work hardening. Obviously, we considered here the "worst case" scenario. If a more suitable hardening law would be chosen, e.g. Ludwik-Holomon, the requirements with respect to the fitting range are much less strict. The crux of the problem, however, is the selection of a proper hardening law. Figure 44 shows the Ludwik-Holomon law fitted to the pre-necking data of the reference material. It can be inferred that the post-necking strain hardening is slightly overestimated by the extrapolated Ludwik-Holomon law. The simulation results are shown Figure 45 and this shows a very good accuracy with respect to the cross-section and process graph. The stress state within the neck is slightly over estimated by approximately 20 MPa. In conclusion:

1. If a proper hardening model is available, then the requirements with respect to the size of the fitting range are less demanding. Nevertheless, it is always recommended to acquire large strain data to improve the fitting quality of the hardening law.
2. If a proper strain hardening law cannot be identified in advance, it is recommended to probe at least strains up to 0.7 in the material test used for identifying the flow curve.

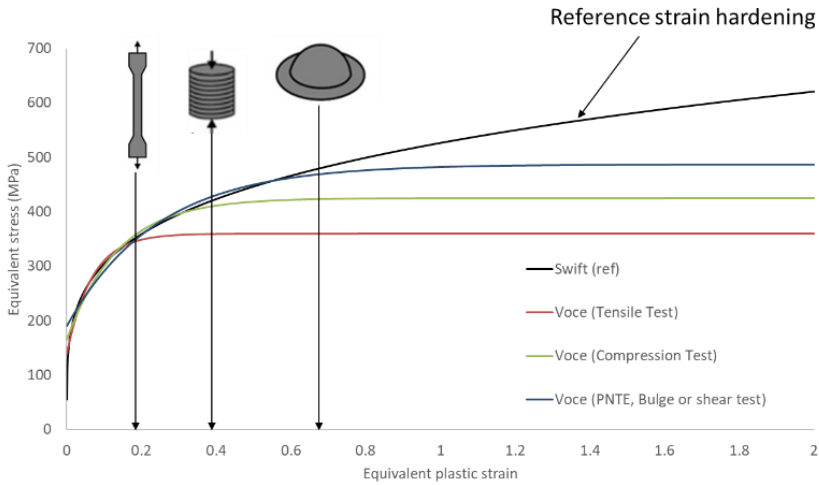


Figure 41: Reference strain hardening (Swift) and fitted Voce model using different data sets according to typical material tests to identify the flow curve

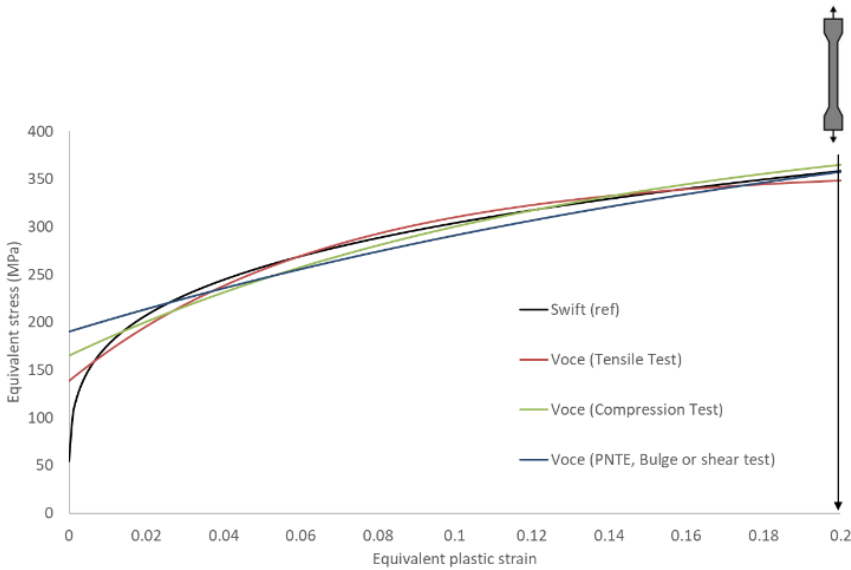


Figure 42: Reference strain hardening (Swift) and fitted Voce model using different data sets according to typical material tests to identify the flow curve: the pre-necking region

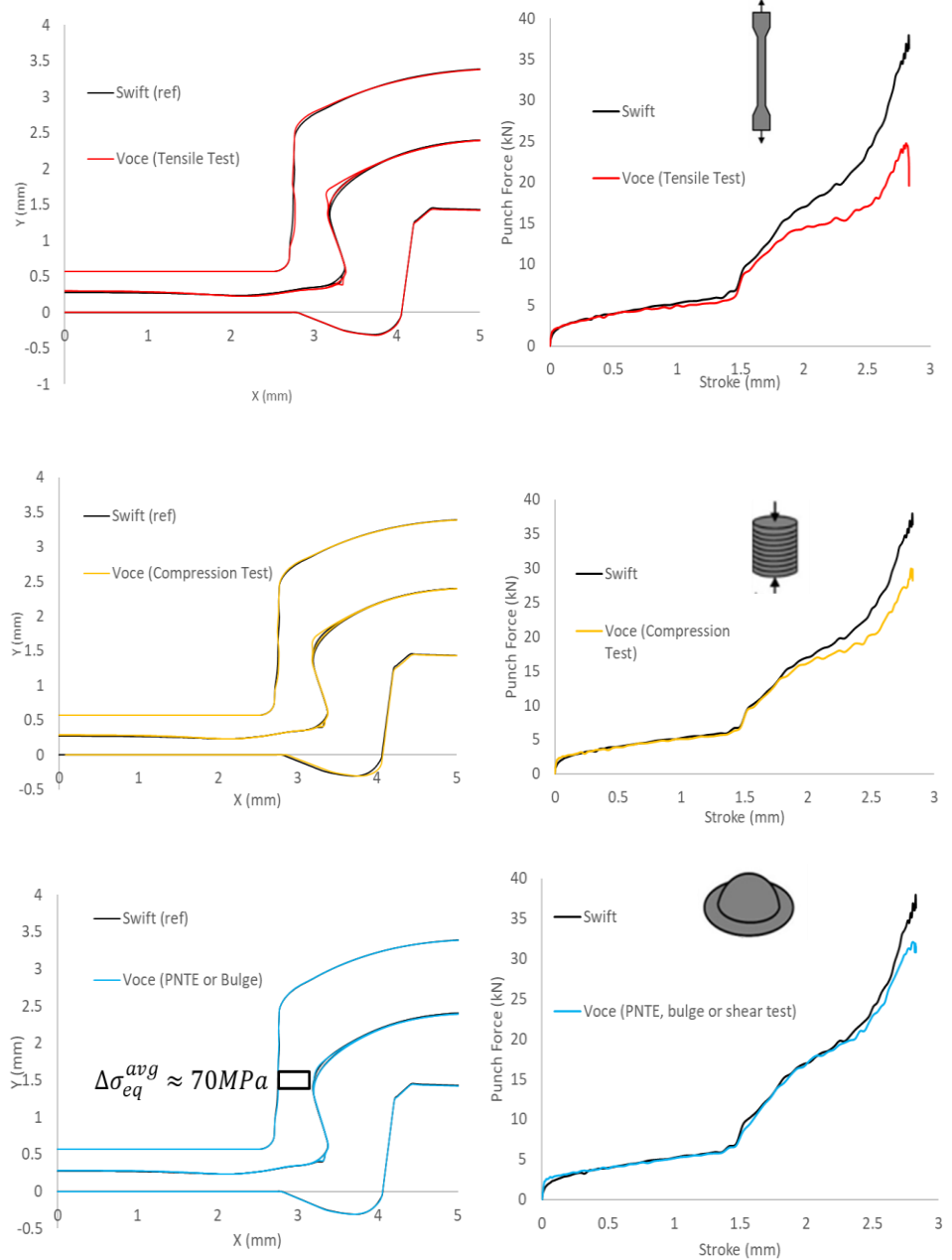


Figure 43: Effect of hardening law selection and strain range used to fit the hardening law

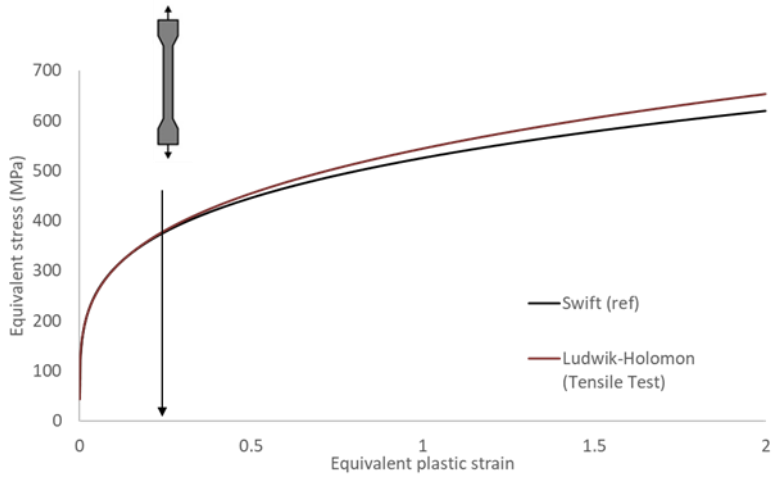


Figure 44: Ludwik-Holomon hardening fitted to the pre-necking data of the reference strain hardening represented by Swift's hardening law

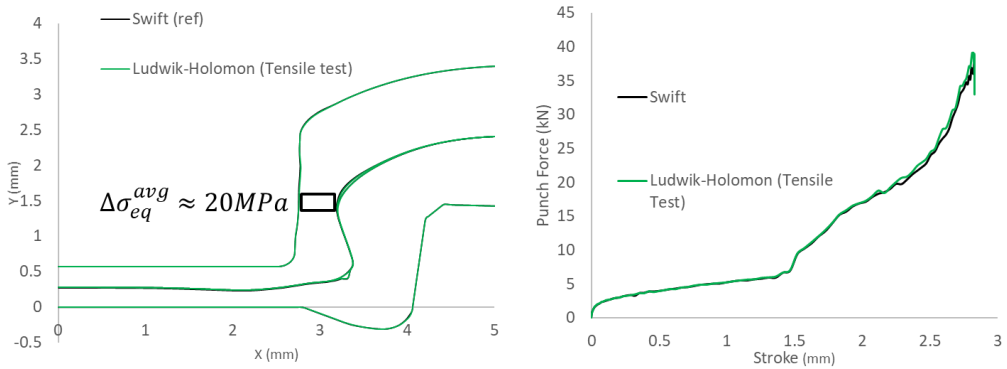


Figure 45: Effect of hardening law selection: Ludwik-Holomon fitted to the pre-necking data of the reference material

### 7.3 Strain rate effect

The strain rate that occurs with the clinched joint during forming depends on the punch speed. A rough estimation of the strain rate can be calculated by:

$$\dot{\varepsilon}_{eq,AVG}^{pl} = \frac{d\varepsilon_{eq}^{pl}}{dt}$$

To calculate the average strain rate, one needs the plastic equivalent strain in a material point and the total time increment. The latter depends on the punch speed. If a punch speed of 20 mm/s is used, and assuming that plastic equivalent strains of 1 to 2 are generated, then very high strain rates in the order of 7 to 14  $\frac{1}{s}$  are generated, respectively. Even if the joining process is conducted slowly, let's say completion after 1 second, strain rates of the order 1 to 2  $\frac{1}{s}$  can be expected (locally even much higher). Such strain rates are typical for forging applications. Given that many sheet metal material tests are conducted under quasi-static conditions, i.e. strain rate in the order of  $10^{-2}$   $\frac{1}{s}$  to  $10^{-3}$   $\frac{1}{s}$ , it is questionable to ignore strain rate effects in joining by forming of strain rate sensitive metals. In order to understand the importance of strain rate effects in clinch forming a mixed experimental-numerical approach was followed.

#### 7.3.1 Numerical

To assess the relevance of including strain rate dependency in clinch forming, a virtual experiment was conducted. The left panel of Figure 46 shows the FE model used to investigate the impact of considering strain rate dependency. The material considered here is DC04. The strain rate sensitivity of this material was determined by conducting tensile tests under different strain rates. The flow curves derived from these experiments are shown in the right panel of Figure 46. The punch velocity in the FE model was chosen to be 20 mm/s yielding high strain rates in the material. Figure 47 shows the calibrated strain rate dependent hardening model. The reference strain rate in the model equals 0.0001  $\frac{1}{s}$ . The strain rate sensitivity is identified as  $m=0.00921$ . The green solid curve is the material response predicted by the strain rate dependent hardening model for a strain rate of 0.1  $\frac{1}{s}$ . It can be seen that the model yields a good prediction: except for initial yielding the green curve is in good agreement with the experimentally obtained red curve.

Figure 49 shows the simulation results obtained with and without strain rate dependency. It can be inferred that the metal flow is slightly affected. However, the predicted contours are within the scatter of the experimentally obtained cross-sections. However, the stress levels within the joint are strongly affected. The reason for this is twofold:

1. An increasing strain rate comes with an increase in flow stress for the material under investigation; The strain rate dependent model is calibrated in the pre-necking region and subsequently extrapolated into the post-necking region. This extrapolation introduces a lot of uncertainty.

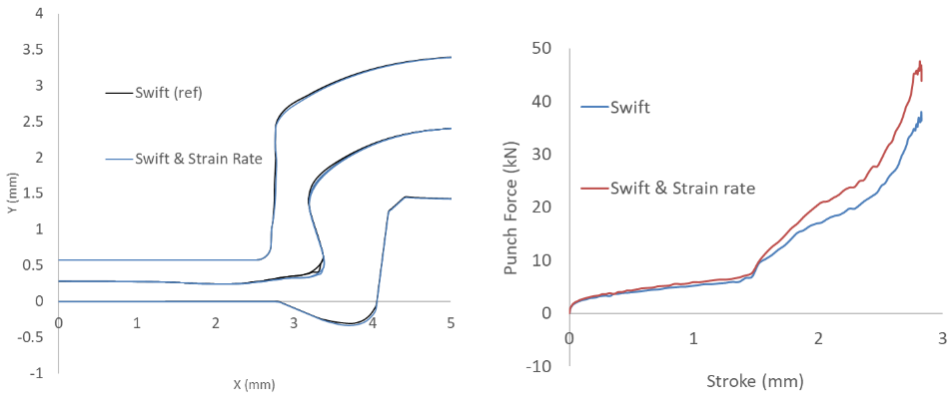


Figure 49: Extrapolation of the rate dependent hardening model (calibrated in the pre-necking region)

- Figure 48 shows that the extrapolated pre-necking data (tensile test 0.1/s) differs from the predicted strain hardening behaviour by the calibrated strain rate dependent model.

Conclusions:

- Strain rate effects potentially bias the simulation of joining by forming processes;
- Consideration of strain rate effects in clinch forming is hampered by the fact that little is known about strain rate dependency in the post-necking regime. Moreover, it is difficult to conducted experiments enabling to unambiguously probe strain rate sensitivity at large plastic strains.

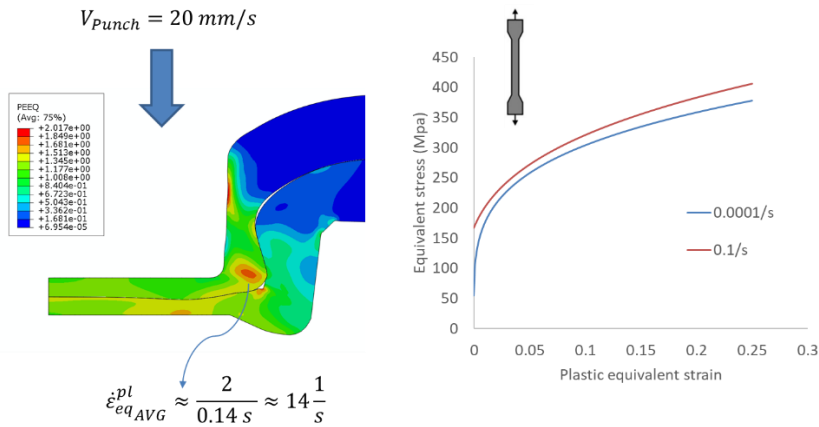


Figure 46: Effect of strain rate dependency in clinch forming

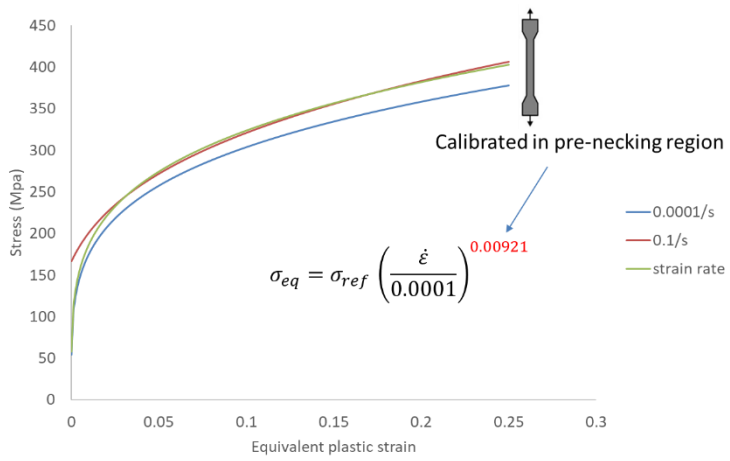


Figure 47: Calibration of the strain rate dependent hardening model

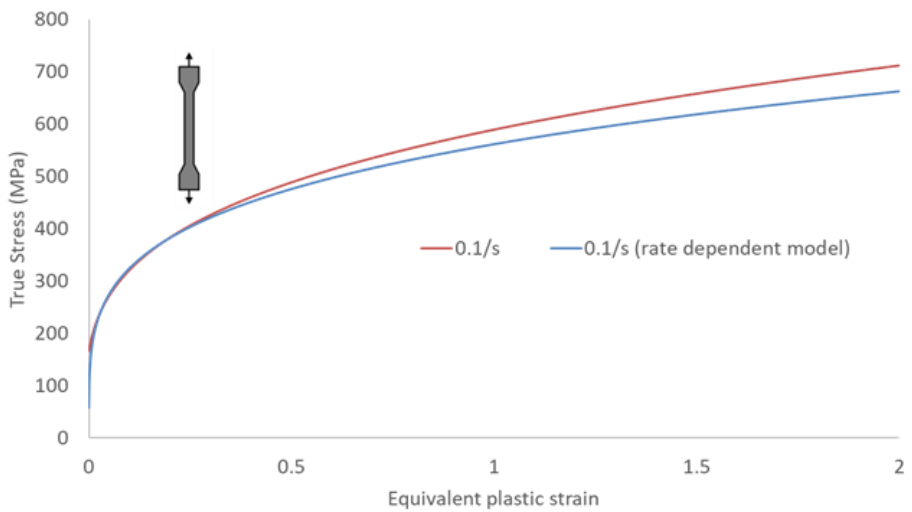


Figure 48: Effect of strain rate dependency in clinch forming

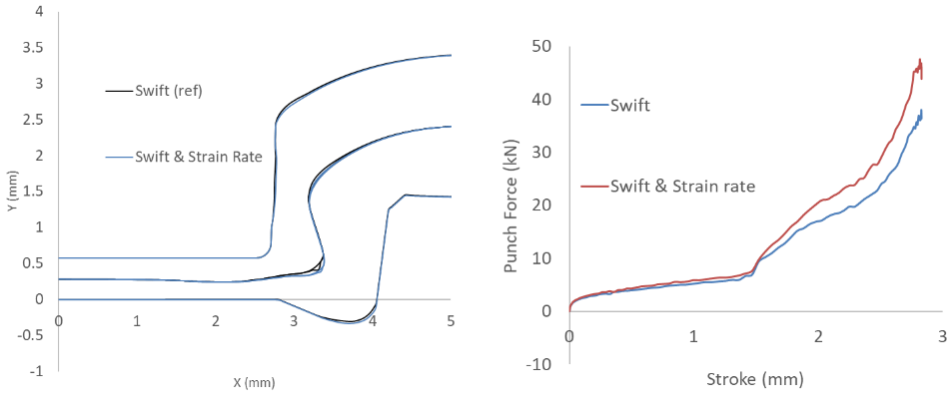


Figure 49: Extrapolation of the rate dependent hardening model (calibrated in the pre-necking region)

Joining by forming is associated with a large deformation energy in a relatively small forming zone. The generated plastic energy is partially converted into heat. As clinch forming can occur at high speeds resulting in high strain rates, the process might be seen as an adiabatic event in the sense that dissipation cannot occur sufficiently fast by heat radiation or thermal conductivity. Although, cold joining is of interest, significant heating of the forming zone can be expected when high joining speeds are used. Hartel et al. [HAR17] investigated heat generation in mechanical joining process. They found that the temperature in flat-clinching of DC04 sheets increases up to 240 degrees Celsius. The latter was derived with the aid of an experimentally validated thermo-mechanically coupled FE model developed in Simufact. Such a temperature increase causes thermal softening and the numerical simulation taking thermal effects into account was in close agreement with the experimentally observed metal flow.

It is well known that the strain rate dependence displayed by most metals affects the energies, force and forming limits involved in high speed forming. The Johnson-Cook model is a frequently used constitutive model enabling to simultaneously take strain rate and temperature dependent material behaviour into account:

$$\sigma_{eq} = (A + B\varepsilon^n) \left(1 + C \ln \frac{\dot{\varepsilon}}{\dot{\varepsilon}_0}\right) \left(1 - \left[\frac{T - T_{room}}{T_{melt} - T_{room}}\right]^m\right)$$

This model is used to understand the concurring effects between strain rate (that causes hardening) and thermal softening during clinch forming. The first part of the right hand side corresponds to the isothermal strain hardening behaviour conducted under quasi-static conditions, i.e. under a reference strain rate  $\dot{\varepsilon}_0$ . The second factor and the third express the rate effect and the thermal softening, respectively. Both C and m are calibrated using high strain rate tensile tests. As such, the reliability of the JC model can only be guaranteed in the pre-necking region. Moreover, the reliability of the JC model is also associated with the strain rate level itself. Nevertheless, the JC model can be used in a virtual experiment of a clinching forming process to understand the combined effects of strain hardening and thermal softening. C and m were taken from Verleysen et al. [VER11] and can be found in table 9.

Table 8: JC parameters obtained from [VER11].

C	m
0.071	0.23

A thermo-mechanically coupled model was built in Abaqus assuming the thermal properties shown in Table 9. The process is quasi-static and a punch velocity of 1 mm/s was adopted. A quasi-static punch speed generates maximum strain rates in order 2 to 4 1/s. The process graph of the *full thermo-mechanical model* is shown in Figure 50. In addition, Figure 50 also depicts the process graph of the *isothermal model* which is solely considering quasi-static strain hardening without rate and thermal effects. It can be seen that for quasi-static clinch forming, the full thermo-mechanical model yields a similar process curve than the isothermal model. The only difference is at the end of the process which is characterized by the forging of the material between anvil and die. This step comes with a fast increase of the strain rate and increase of the temperature. As the increase of strain rate and temperature have a concurring effect on hardening, the correspondence between the thermo-mechanical and the isothermal model suggests a balance between both effects. In the final step of the process, however, it seems that thermal softening is stronger than the rate effect. Figure 50 also shows the disentanglement of the rate and the thermal effects. Finally, it can be stated that all the models yield a similar metal flow. Very small differences in neck thickness and interlocking was observed. Simufact was also used to scrutinize the effect of strain rate and thermal softening. This study confirmed the small effect on the metal flow for quasi-static clinch forming.

#### Conclusions:

- It can be stated that for quasi-static clinching forming, locally strain rates of the order 2 to 4  $\frac{1}{s}$  occur;
- For clinch forming, a concurring effect between thermal and rate effects determines the process graph. For quasi-static loading, both effects seems to attenuate each other.
- Given that the calibration of the JC model i) is confined to the pre-necking region, ii) is inaccurate for moderately low strain rates and iii) comes with a large experimental effort, it is recommended to conduct the FE simulation using quasi-static experiments to identify the post-necking strain hardening.

Table 9: Full thermo-mechanical model: parameters

Property	Value
Conductivity	43 Wm <sup>-1</sup> K <sup>-1</sup>
Density	7850 kgm <sup>-3</sup>
Expansion	1.2 e <sup>-5</sup> at 293 K
Inelastic heat fraction	0.9
Surface radiation	440 Jkg <sup>-1</sup> K <sup>-1</sup>
Surrounding temperature	296 K

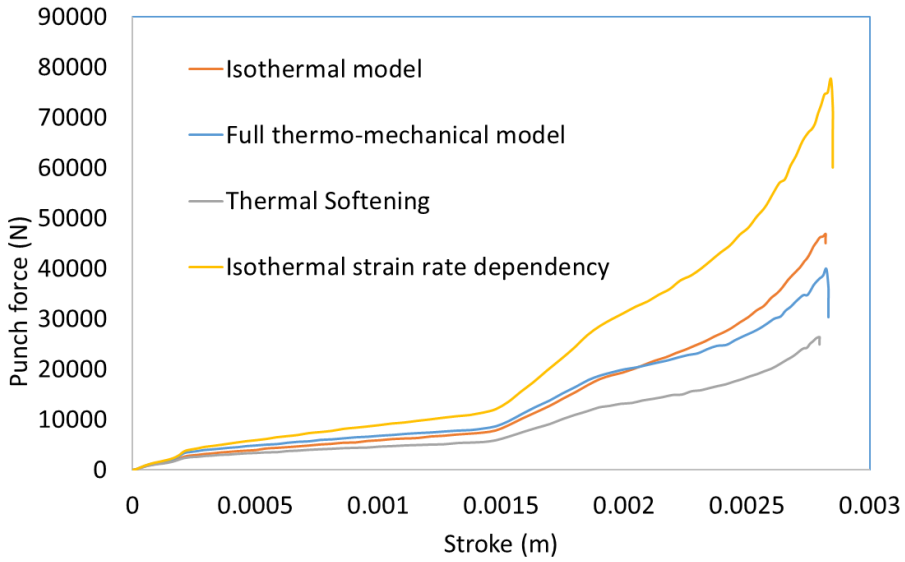


Figure 50: Effect of strain rate and thermal softening on the process graph in clinch forming

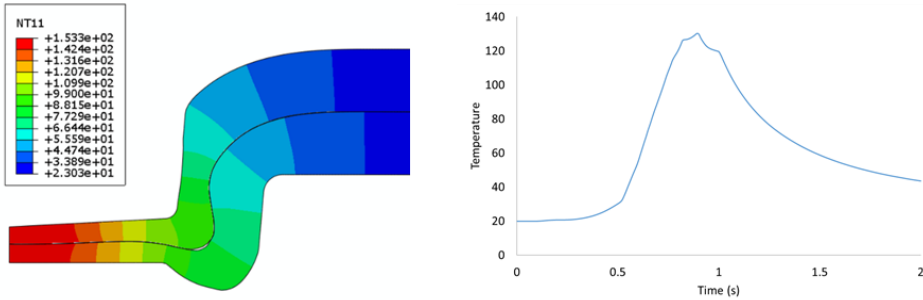


Figure 51: Left: temperature within the clinched joint just after complete die filling. Right: evolution of temperature in the bottom of the joint. After 1s: tools removed

### 7.3.2 Experimental

Given the difficulties in incorporating a reliable strain rate and temperature dependent material model in clinch forming simulations, we opted also to experimentally investigate the effects of strain rate. Figure 52 shows the experimental data acquired by conducting clinch forming of DC04-DC04 by different punch speeds. The process graph shows a complex interplay between rate effects and thermal softening. Intuitively, given the positive strain rate sensitivity of DC04, one would expect that the highest punch speed would result in the largest amount of energy required to complete the process. However, it can be seen that a punch speed of 50 mm/s yields the lowest maximum force. As predicted by the thermo-mechanical simulation, the biggest difference can be seen in the forging stage of the process. Increasing the punch speed consistently lowers the forging force. It can be seen that, depending on the speed, the forging stage is highly affected. The concurring effect between thermal and strain rate effects is clear for DC04-DC04. The effect on the associated metal flow is less pronounced. Some difference in the interlock can be seen in the left panel Figure 52 but more experiments are required to draw statistically solid conclusions here. The same experimental campaign was conducted on the joining case EN AW 5182- EN AW 5182. The results can be found in Figure 53. Obviously, EN AW 5182 is less sensitive to strain rate than DC04. As a consequence, both the process graph and the metal flow are not significantly affected by the joining speed.

The following conclusions can be drawn:

- Rate and thermal effects in joining by forming strongly depend on the material.
- For materials with a positive strain rate sensitivity, it seems that the concurring effects of strain rate and thermal softening attenuate each other out in quasi-static joining by forming.
- The topic of strain rate and thermal effects in joining by forming is underexposed in literature.

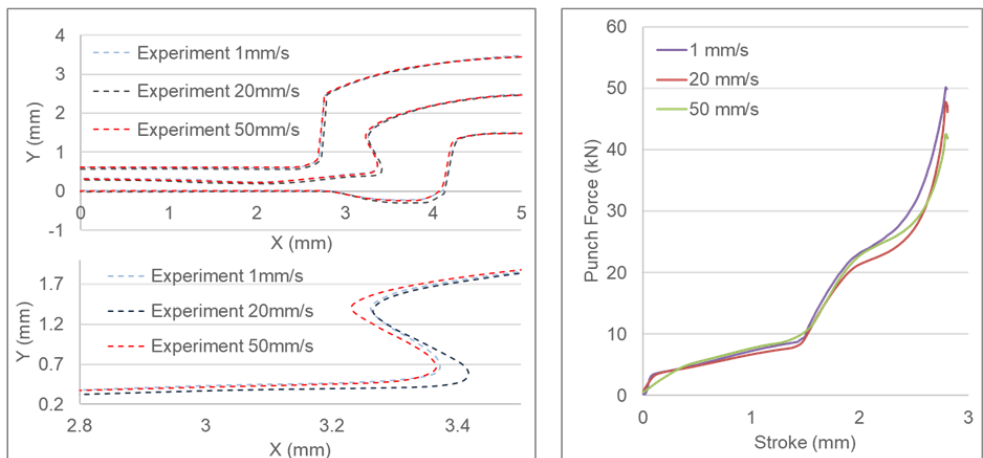


Figure 52: Average joint contour (left) and process graph (right) for clinching with different punch speeds of DC04 in DC04

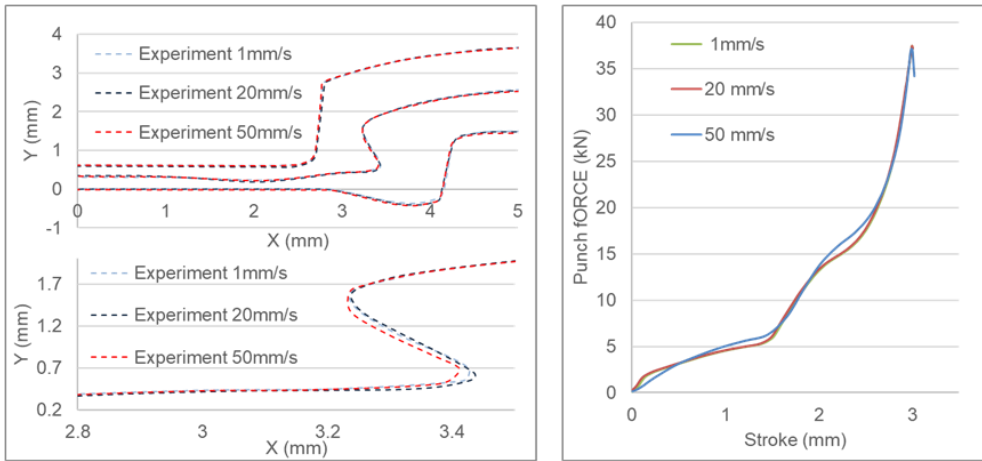


Figure 53. Average joint contour (left) and process graph (right) for clinching with different punch speeds of EN AW-5182 in EN AW-5182

---

## 7.4 Conclusions

### 1. Plastic Anisotropy

The material tests used to identify the flow curve subject the material to a specific deformation mode. When the material exhibits plastic anisotropy, the resulting flow curve might depend on the chosen material test. The effect of this on the numerical computation of the joint contour (or metal flow) is in general marginal for joining by forming. The internal stress state, however, strongly depends on this.

### 2. Flow curve data

- When dealing with physically anisotropic material that must be modelled using an isotropic material model, it is recommended to identify the flow curve using a material test with a predominant deformation mode resembling the one that dominates the mechanical joining technique;
- It is recommended to probe at least a true plastic equivalent strain of 0.7 in the material test. This improves the fitting quality of the chosen hardening law. Moreover, it is shown that for joining by forming, the importance of the selected hardening law significantly decreases by fitting the hardening law to large strain data. To mitigate the problem of hardening law selection, it is recommended to use at least a strain range between 0 and 0.7 true plastic strain.
- Very limited information is available about the effect of strain rate and thermal softening. The recommendations above apply to quasi-static joining by forming operations, or materials which exhibit a small strain rate sensitivity. More research is required for high speed joining by forming as it is shown that there occurs a complex interplay between strain rate effects and thermal softening.

## 8 Material characterization methods

In sheet metal forming, variety of material tests are available which can be used to characterize material. These tests include tensile test, stack compression test (SCT) for single axial loading while hydraulic bulge test (HBT), biaxial tension and shear test are for biaxial loading [BRU14]. A short summary of these tests can be seen in Figure 54. The first quadrant of the stress space includes the tests having tensile stress states with uniaxial tensile test at positive x-axis. While the third quadrant has tests with compression stress states with uniaxial compression test. In the middle of second quadrant, simple shear test and in-plane torsion test can be found. Both these tests are used to describe material in shear states [YIN14].

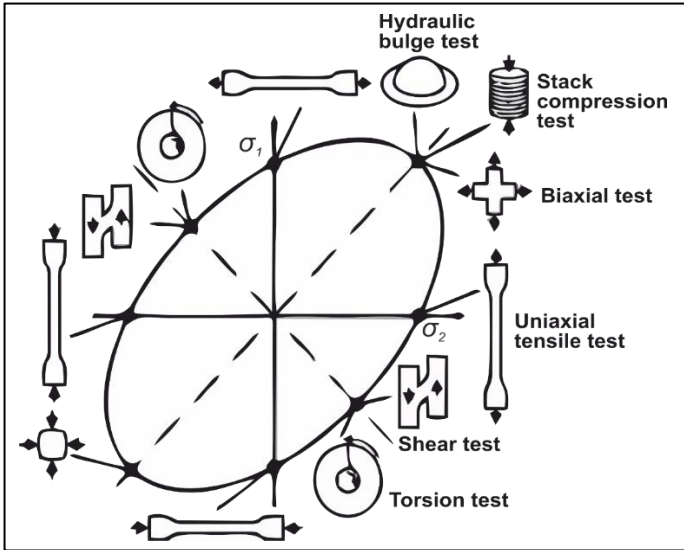


Figure 54: Material tests available for the characterization of material in sheet metal forming [YIN14]

### 8.1 Tensile test

Probably the most commonly adopted material to characterize a material is the simple uniaxial tensile test. There are basically two types, strain controlled and stress controlled. Since stress controlled can only be used for elastic region, strain controlled is more popular and is used frequently (ISO 6892-1, 2009). The test can be performed using a universal testing machine and dimensions of the specimen (Figure 2.5) can be taken as per European standard (EN 10002-1, 2001).

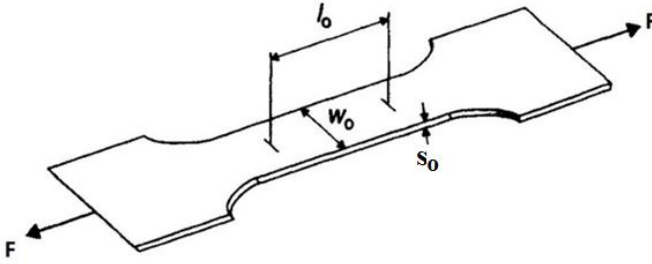


Figure 55: A typical tensile-test specimen strip (MAR02)

If the original cross-sectional area  $A_0$  and gage length  $l_0$  of the specimen are used for the calculation, the stress and strain is called engineering stress and engineering strain and if instantaneous area  $A$  and gage length  $l$  are taken then the stress and strain is called true stress and strain. As the cross-sectional area tends to decrease in tensile test, the true stress is always greater than the engineering stress [GER04]. The force and displacement results from the experiment can be converted to engineering stresses  $\sigma_e$  and engineering strains  $\varepsilon$  as per

$$\sigma_e = \frac{F(t)}{A_0} \quad 2$$

$$\varepsilon = \frac{\Delta l}{l_0} = \frac{l_f - l_0}{l_0} \quad 3$$

And true stress and true strain as per

$$\sigma = \frac{F(t)}{A} = \sigma_e(1 + \varepsilon) \quad 4$$

$$\varphi = \ln\left(\frac{L}{L_0}\right) = \ln(1 + \varepsilon) \quad 5$$

Consequently, the plastic strain  $\varphi_{pl}$  can be determined by deducting the elastic strain  $\varphi_{el}$  from the true strain as

$$\varphi_{pl} = \varphi - \varphi_{el} = \varphi - \frac{\sigma}{E} \quad 6$$

Assuming a pure uniaxial stress state, the flow stress  $k_f$  and equivalent plastic strain  $\bar{\varphi}$  are as

$$k_f = \sigma \quad 7$$

$$\bar{\varphi} = \varphi_{pl} \quad 8$$

Thus, the given data can be used to determine the flow curve until the maximum tensile strength.

The uniaxial tensile test has few drawbacks. First of all, the test is limited by the onset of diffuse necking in the specimen and hence plastic strain can only be measured until the range of 0.1 to 0.3 true plastic strain.

## 8.2 Extended tensile test

Obviously the standard tensile test is of limited usefulness to acquire the large strain flow curve. Coppieters et al. [COP11] proposed to extract the post-necking hardening curve from the diffuse neck during a quasi-static uniaxial tensile test. In essence, the identification strategy relies on the minimization of the discrepancy between the external work and internal work within the diffuse neck. The external work can be easily determined based on the elongation of the diffuse neck and the tensile force. The displacement fields at the surface of the diffuse neck are measured with the aid of a stereo-DIC system. Subsequently, an element mesh is used to reconstruct the strain tensor for each material point in the diffuse neck. A stress update algorithm incorporating the material model (i.e. yield criterion and hardening law) is then used to reconstruct the experimental stress fields within the diffuse neck. The reconstructed strain and stress fields at different load steps enable to compute the internal work. The key point is that the unknown post-necking hardening curve is identified by minimizing the discrepancy between internal and external work. Detailed information about the method can be found in [COP11, COP14c].

Standard tensile specimens according to ISO 6892 are used to extract the post-necking hardening curve. The experiment is conducted on a standard tensile testing machine with a load capacity of 10 kN. In order to subject the material to quasi-static conditions ( $\dot{\epsilon} \approx 10^{-3}/s$ ) within the diffuse neck, a constant crosshead speed of 0.05 mm/s is applied. The area of interest (AOI), i.e. the region in which the diffuse neck develops, is taken as 20 mm x 40 mm. The displacement fields obtained through DIC are used to reconstruct the strains in the AOI using a mesh containing 2,960 bilinear elements. The multi-step stress return mapping algorithm proposed by Yoon et al. [YOO04] is adopted to reconstruct the stress field at the Gauss points of the element mesh. 100 load steps are used in the identification process. Figure 56 shows a schematic overview of the method. Displacement fields are measured using DIC. The strain fields then are reconstructed using an element mesh. Finally, the strain increments are used to derive the experimental stress field using a return mapping algorithm. The latter requires the choice of a hardening law of which the parameters are sought by minimizing the discrepancy between external and internal work using the following cost function:

$$C(\mathbf{p}) = \frac{1}{2} \sum_{i=0}^N ((W_{ext})_i - (W_{int}(\mathbf{p}))_i)^2$$

An important caveat regarding the identification procedure, however, is that the material is assumed plastically isotropic. Tardif and Kyriakides [TAR12] showed that the profile of the diffuse neck depends on the degree of plastic anisotropy. Hence, the identification of the post-necking hardening potentially depends on the plastic anisotropy. Coppieters and Kuwabara [COP14c] investigated the importance of the adopted anisotropic yield criterion with regard to the identification of the post-necking hardening curve and found a minor influence for mild steel sheet. Ha et al. [HA20] recently investigated this for AA6022-T4 and drew the same conclusion that the post-necking strain hardening is not affected by potential plastic anisotropy.

Finally, Hakoyama et al. [HAK19] showed the influence of the strain rate can be safely ignored when applying the procedure of Coppieters et al. [COP11] and further improved by Coppieters and Kuwabara [Cop14c].

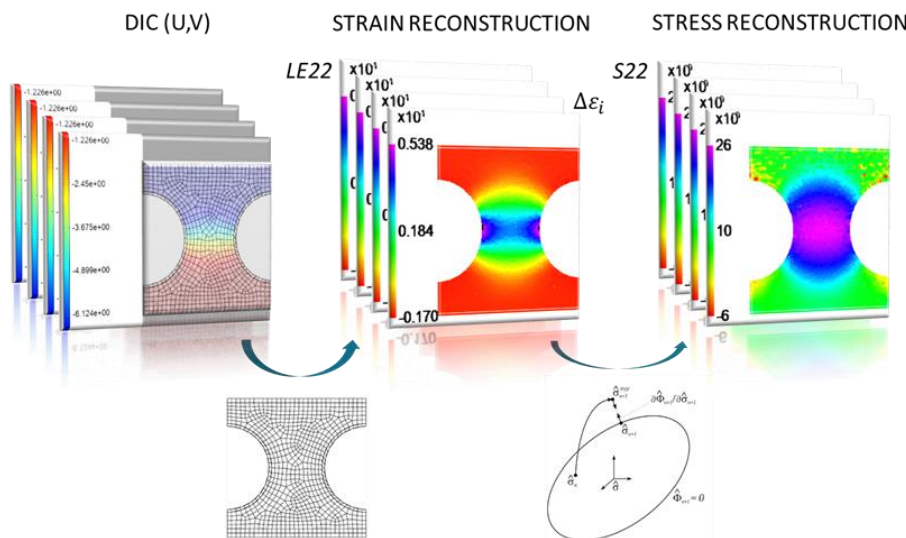


Figure 56: Schematic overview of the Extended Tensile Test

### 8.3 Stack compression test (SCT)

The SCT, also referred to as through-thickness compression test, layer compression test or multi-layer upsetting test, enables to suppress plastic instabilities hence enabling to probe large plastic strains. The stack can consist of small circular discs or square specimens. The stack is compressed between parallel plates of a testing machine, see Figure 57. A clear benefit is that the SCT requires only a small amount of test material, which can be locally removed to acquire the local flow behaviour. Friction between the stack and the compression platen is inevitable. A friction-hill analysis shows that a small height to diameter (or width for bricks) ratio, referred to as aspect ratio in the remainder of this work, requires a correction for friction to obtain an accurate flow curve. The latter implies that the friction coefficient can be measured, and, more importantly, is constant during the SCT. Indeed, friction conditions might vary as lubrication deteriorates due to thinning of the film and extension of the surface. With the aid of the ring compression test, An and Vegter [AN05] showed that oiled PTFE film yields a constant frictional behaviour. Coppieters [COP12] adopted the modified two specimen method [HAN02] to calibrate the coefficient of friction in the SCT of low carbon steel. Steglich et al. [STE14] and Merklein and Godel [MER09] did not correct for friction when subjecting magnesium alloys and steel sheets to the SCT, respectively. Despite this inconsistency with respect to the role of friction in the SCT, it is clear that the aspect ratio plays a crucial role in assessing the need for friction correction [AN05]. The lower the aspect ratio of the stack, the more pronounced the frictional effect and the need for friction correction. However, when targeting the large strain flow curve, a small aspect ratio is favoured for the stability of the stack deformation and mitigating preliminary stack defects such as disc localization. Moreover, frictional effects lead to a triaxial stress state which further complicates the determination of the flow curve. Obviously, friction is a disadvantage of the SCT. The crux of the problem is that one must be able to guarantee a strain range for which a constant frictional condition prevails. In addition, correction of the flow curve requires a method to quantify the frictional condition.

When a shearable film (e.g. TPE) is used, a correction can be made based on the shear strength of the film [AN05].

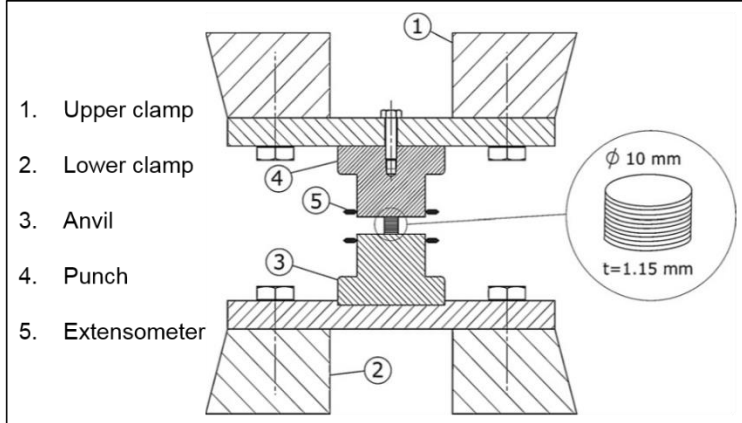


Figure 57: The schematic experimental set-up for stack compression test [COP10]

In this work, oil is applied to minimize the effect of friction. The average compressive true stress is calculated as:

$$\sigma_{avg}^c = \frac{F \cdot h}{\pi \cdot r_0^2 \cdot h_0}$$

where  $\sigma_{avg}^c$  is the average compressive true stress,  $F$  the measured force and  $h_0$ ,  $r_0$  the initial stack height and radius, respectively. The logarithmic true compressive strain is simply:

$$\varepsilon = \ln\left(\frac{h_0}{h}\right)$$

When dealing with a low aspect ratio of the stack, it is required to compensate for friction. The friction-hill analysis of a homogenous compression of a single disc [DIE87] leads to:

$$\sigma = \frac{2 \cdot \sigma_{avg}^c}{\left(\frac{h}{\mu r}\right)^2 \cdot \left[ e^{\frac{2\mu r}{h}} - \frac{2\mu r}{h} - 1 \right]}$$

with  $h$ ,  $r$  the instantaneous height and radius of the stack, respectively. The height  $h$  of the stack is measured and  $r$  is derived assuming volume constancy.

Equivalent plastic strain up to 0.7 can be determined using this test [BRU14]. If the material is assumed to be plastically isotropic, the von Mises equivalent flow stress  $\sigma_{eq}$

$$\sigma_{eq} = \sigma$$

and equivalent plastic strain  $\varepsilon_{eq}^{pl}$

$$\varepsilon_{eq}^{pl} = \varepsilon$$

are calculated and used for constructing flow curve.

## 8.4 Plane strain compression test (PSCT)

One of the disadvantages of the compression test is the barrelling of the stack due to friction between the large contact region between the sheets and the compression platens. This problem can be mitigated by using dies with thin indenters forming a flat groove along the width of the sheet [REE12]. The sheet is in plane strain condition as the deformation in the width direction is almost zero and the decrease in thickness direction is compensated by elongation in the length direction. Thus, the testing process is very similar to cold rolling of sheets and consequently the test was further expanded as a material characterization method for large strains [ROW77].

The sheet metal strip is pressed between the upper and lower tools forming an indentation in the middle. The friction in the contact region can be addressed by applying lubricant e.g. paste of molybdenum disulphide [YAB14].

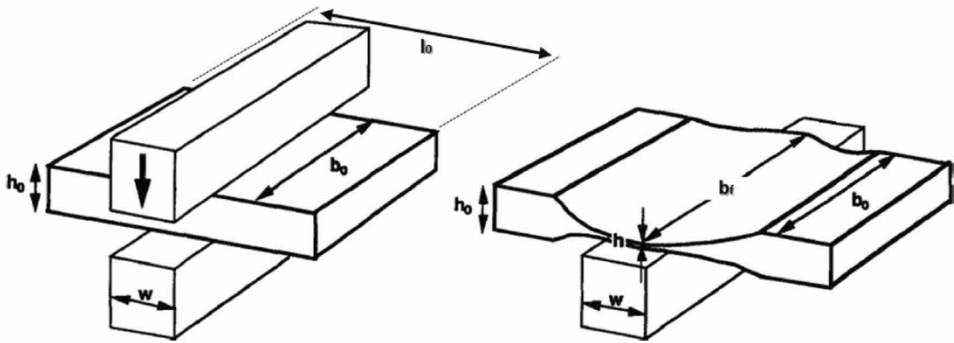


Figure 58: The schematic experimental set-up for plane strain compression test [GEL94]

The PSCT's performed in this project were carried out by Faurecia Autositze GmbH using the method described in [CHE20]. The equivalent stress according to Tresca's yield criterion can be computed as:

$$\bar{\sigma}^T = \frac{F}{ab} \frac{1}{\frac{h}{\mu a} (e^{\mu \frac{a}{h}} - 1) + \frac{1}{4} \tan(\alpha)}$$

With  $F$  the compressive force,  $a$  the tool width excluding the tool radii,  $b$  the actual width of the specimen,  $h$  the actual thickness of the specimen,  $\mu$  the coefficient of friction and  $\alpha$  the angle between the free workpiece surface and the flat surface of the tool without a radius at the border of the ideal forming zone.

The von Mises equivalent strain can be computed as:

$$\bar{\varepsilon}_{pl}^{vM} = \frac{2}{\sqrt{3}} \varepsilon_{ps}$$

With  $\varepsilon_{ps}$  the global true strain in the ideal plane strain state. The final flow curve according to the von Mises yield criterion is obtained via a conversion to the uniaxial tensile test. This scaling is conducted in accordance with the work equivalence conditions and schematically shown in Figure 59. More details can be found in [CHE20].

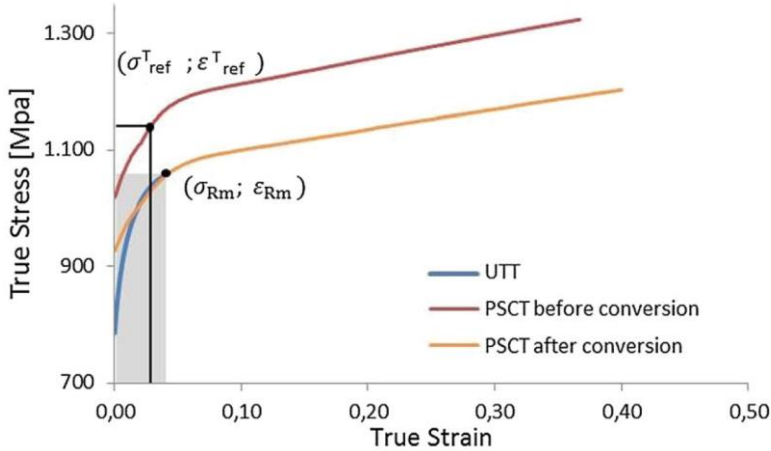


Figure 59: Scaling the PSCT to the UTT in accordance with the work equivalence condition. After [CHE20]

## 8.5 In-plane torsion test (IPPT)

The in-plane torsion test provides an excellent method to characterize material in a simple shear state and determine flow curve in the post-necking regime. As the standard tests like tensile or stack compression test are not able to investigate shear stress states, this test offers this option [YIN15]. Many of the limitations such as necking or buckling and frictional effects can be overcome with this test [BRU14].

As shown in Figure 60, the set-up for in-plane torsion test consists of an inner and outer clamp, the circular specimen is fixed between these clamps. The measurement of torque is done by a static torque sensor attached to the Zwick 100 kN universal testing machine. The clamping force of 100 kN and rotational speed of the servo motor of 0.01 rpm can be used for the experiment. The outer clamps at  $r = 30$  mm is rotated with an external torque while the inner clamp at  $r = 15$  mm is kept fixed [YIN15]. This imparts shear stress state in the sheet which varies in gradient along the radial direction with maximum value at the inner clamp radius as shown by red line in Figure 60 [TRA18b].

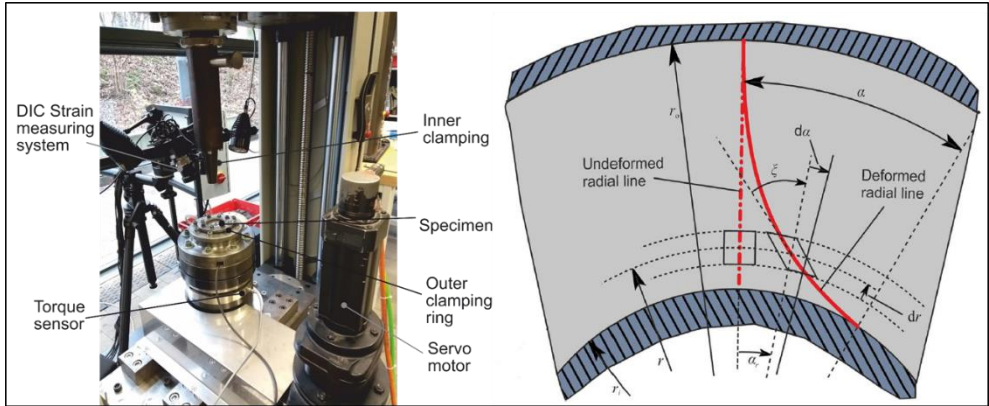


Figure 60: Experimental setup of in-plane torsion test (left) and variation of shear stress along the radial direction for specimen in-plane torsion test (right)

The measurement of the torque  $M$  and rotation angle  $\alpha$  in the circular sheet with thickness  $s$  is done using a rotary encoder and a torque sensor connected with the testing machine. The shear stress  $\tau$  and shear strain  $\gamma$  generated in the element at radial distance  $r$  for the specimen can then be calculated using [TRA18a]:

$$\tau = \frac{M}{2\pi \cdot s \cdot r^2} \quad 9$$

$$\gamma = r \frac{d\alpha}{dr} \quad 10$$

Finally equivalent flow stress  $k_f$  and equivalent plastic strain  $\bar{\varphi}$  can be calculated according to von Mises criterion [TRA18a]:

$$k_f = \sqrt{3} \cdot \tau \quad 11$$

$$\bar{\varphi} = \frac{\gamma}{\sqrt{3}} \quad 12$$

However common tests available to investigate shear fracture possess some limitations. For most of the cases, the specimen fails at the edges of the sheet rather than at shear crack tip which is ideal location for measurement of strain. There has also been instance where triaxiality and lode parameter doesn't remain constant and tends to vary till fracture [YIN15]. An inclusion of groove in the specimen overcomes these difficulties and also maintains triaxiality and lode parameter equal to zero. The details of the specimen can be seen in Figure 61.

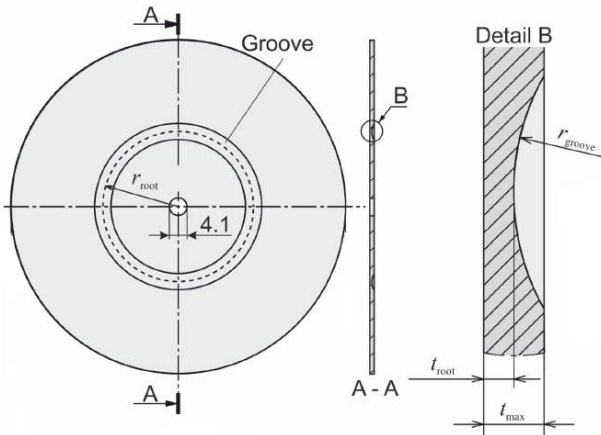


Figure 61: Details of the specimen used in groove in-plane torsion test

The manufacturing of the groove can be done using turning, milling and electronic discharge machining (EDM) and the ideal choice for method will depend material and surface roughness of the specimen [TRA18b]. The dimensions of the groove will depend on the thickness of the specimen used (Table 10). A large emphasis has to be given to the groove depth and width as small change can result to error in flow curve calculation.

Table 10: Groove Dimensions of groove in relation to sheet thickness

$t_{\max}$ in mm	1.0	1.1	1.5
$t_{\text{root}}$ in mm	0.5	0.55	0.75
$r_{\text{root}}$ in mm	17.0	17.1	17.4
$r_{\text{groove}}$ in mm	4.0	4.0	4.0

The measurement of strain at IPPT can be done directly using the DIC measurement system or indirectly by measuring the torque and the rotation angle. However, for larger strains, both these methods possess some disadvantages. For DIC method, the pattern gets distorted severely at the groove section as the rotation angle increases. The direct DIC method can be improved by reapplying a new optical pattern after a certain increment of the test. The results of each increment can be added and flow curve for higher strain can be evaluated with lesser distortion of the pattern. The indirect method can only be used for planar specimen as it fails to measure strains locally [TRA18].

Another method as explained by [TRA18] that can be used without reapplying the pattern is incremental strain measurement. In this method, two tangential lines are drawn virtually, one near the inner clamping ( $r = 15.3$  mm) and another one near outer clamping ( $r = 25$  mm) and the angle of rotation is measured between these two lines until fracture. Since the lines are located outside the grooved region with lesser strain initial optical pattern can be easily detected until the end of the experiment.

One of the major difficulties faced in grooved in-plane torsion test is the determination of strain in the grooved region due to higher strain. At higher strain the pattern used for DIC method

gets distorted severely and become unable to be detected by the camera. Although, this problem can be rectified by using the method incremental strain measurement as described by [TRA18], the measurement of strain is not done on the groove region where maximum strain occurs leading to some error in the result.

Another drawback that can be seen is its limited process window as seen in in terms of sheet thickness  $t$  and inner clamping radius  $r_i$ . For example, when inner clamping radius  $r_i=15$  mm, the sheet with thickness less than 1 mm will tend wrinkle prematurely. Figure 62 shows the wrinkling of the sheet for material with highly ductility for example DC04.

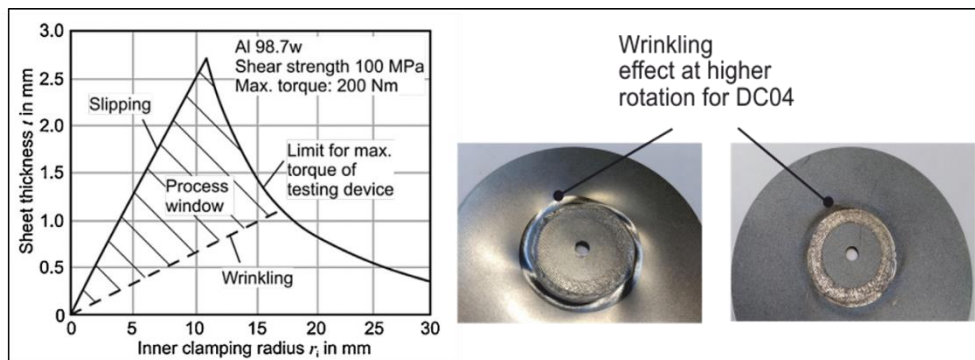


Figure 62: The process limit for in-plane torsion test [TEK82] (right) and Wrinkling effect in DC04 for higher rotation at in-plane torsion test [TRA18]

The IPPT tests performed in this project were carried out by the Institute of Forming Technology and Lightweight Components (IUL) of the TU Dortmund, using the method described in [TRA18a].

## 8.6 Hydraulic bulge test (HBT)

The hydraulic bulge test (HBT) enables to probe large plastic strains under quasi-balanced biaxial tension. The experimental setup of the test is shown in the left panel of Figure 63.

Since the thickness of sheets metal is very small compared to other dimensions, stress in the thickness direction can be ignored and material is under plane stress condition. Also, since the specimen is symmetrical about the central axis, bending stresses are also neglected and membrane theory can be used to calculate equivalent stress. The equation for the membrane theory and is given by

$$\frac{\sigma_1}{\rho_1} + \frac{\sigma_2}{\rho_2} = \frac{p}{s} \quad 13$$

with  $\sigma_1$  and  $\sigma_2$  as principal stresses,  $\rho_1$  and  $\rho_2$  as radii of curvature,  $p$  being hydraulic pressure and  $s$  is thickness of the sheet. Assuming the material undergoes axisymmetric deformation,  $\sigma_1 = \sigma_2 = \sigma_b$  and  $\rho_1 = \rho_2$  is valid at the top of the dome. Equation 13 can be rewritten as [CAM14]:

$$\sigma_{eq} = \frac{p \cdot \rho}{2 \cdot s} \quad 14$$

The logarithmic true strain is estimated as:

$$\varepsilon = -\varepsilon_1 - \varepsilon_2 \quad 15$$

which is valid assuming equal strain or equal stress at the specimen pole. The radius of curvature  $\rho$  and the principal strains  $\varepsilon_1, \varepsilon_2$  at the top of the bulged specimen are measured using a stereo DIC system. In this regard, ISO 16808 is followed and extended with a closed-loop strain rate control at the top of the dome. The average strain rates in the HBT and the SCT are both approximately  $10^{-4} \frac{1}{s}$ .

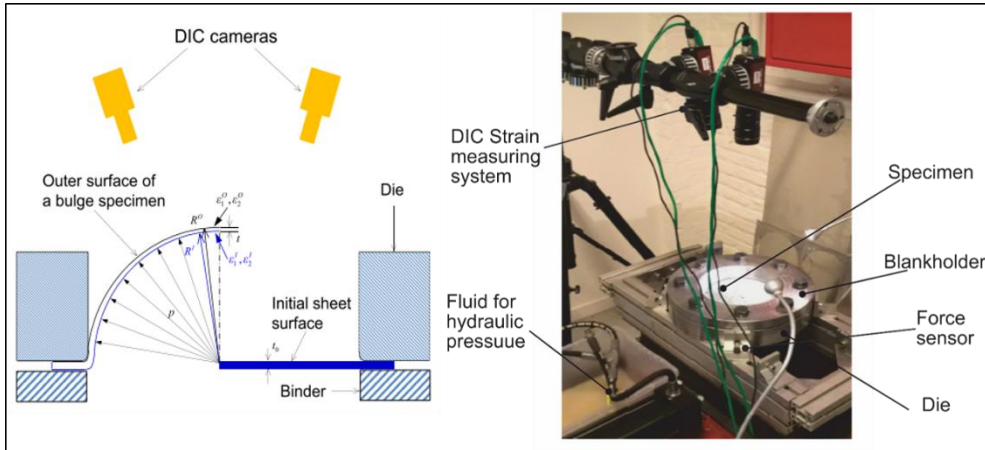


Figure 63: The schematic setup for hydraulic bulge test [MIN17] and the experimental set-up for the hydraulic bulge test [COP18]

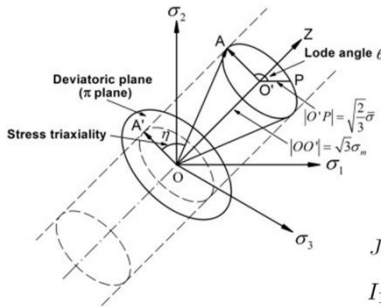
As opposed to the SCT, the HBT does not suffer from frictional effects but in turn lacks accuracy due to assumptions involved in the analytical treatment of the experimental data [MUL15]. In addition, it is well-known that the HBT is not accurate in determining the flow curve at moderately low plastic strains due to the uncertainty related to measuring the curvature of the dome apex. One could also argue that stresses and strains that are used to determine the flow curve are calculated on the outside surface while pressure applied on the sheet is on the inward surface which can lead to some error in the flow curve. The test requires large amount of material and should be strain controlled, thus making the equipment costly and time consuming. The sheet is assumed not to bend during the whole process and onset of fracture must occur at the bulge, however in reality sheet tends to bend a little and sometime the fracture occur prematurely at the draw bead leading to error in calculation. [MIN17]

The HBT tests performed in this project were carried out by Division of Advanced Mechanical Systems Engineering, Institute of Engineering of the Tokyo University of Agriculture and Technology, using the method described in [YAN12].

## 9 Numerical stress analysis

### 9.1 Stress-state metric

If the material exhibits plastic anisotropy, it seems important to calibrate the von Mises yield criterion to a stress state which dominates the joining process. The latter procedure can be regarded as stress state fitting, and, consequently, the selection of a proper material test requires a stress state analysis. Since the deformation generated in joining by forming is expected to be complex, numerical simulation is used for the stress state analysis. The selection strategy involves a first order FE simulation (i.e. using a realistic strain hardening behaviour for the material at hand). The solution variables (stresses and strains) are then used to assess the dominating stress state. A 3D stress state can be unambiguously described by the Lode angle  $\xi$  and the triaxiality  $\eta$  [BAI08].



$$\eta = \frac{-p}{\bar{\sigma}} = \frac{1}{3} \frac{(\sigma_1 + \sigma_2 + \sigma_3)}{\bar{\sigma}}$$

$$\xi = \frac{27}{2} \frac{J_3}{\bar{\sigma}^3}$$

$$J_3 = \det s_{ij} = \frac{1}{27} (2I_1^3 - 9I_1I_2 + 27I_3)$$

$$I_1 = \sigma_1 + \sigma_2 + \sigma_3$$

$$I_2 = \sigma_1\sigma_2 + \sigma_2\sigma_3 + \sigma_1\sigma_3$$

$$I_3 = \sigma_1\sigma_2\sigma_3$$

Figure 64: Lode angle and triaxiality (after [BAI])

Figure 64 is a schematic representation of the Lode angle and triaxiality in the stress space. Both the Lode angle and the triaxiality are scalars derived from the tensorial stress state  $\sigma_{ij}$ . The left panel of Figure 65 shows the  $(\omega-\eta)$ -diagram, where the stress metric  $\omega$  is defined as  $\omega=1-\xi^2\omega = 1-\xi^2$ . For shear-dominated stress states  $\omega$  equals 1, while for axisymmetric stress states  $\omega$  equals 0. The solid black curve shown in the  $(\omega-\eta)$ -diagram is the so-called *plane stress path* directly derived from the normalized plane stress von Mises yield locus (see right panel of Figure 65). The *plane stress path* can be divided in three regions associated with the four stress space quadrants. The blue box and the red box correspond to the first and the third quadrant of the stress space, respectively. The green box contains the stress path associated with the second and the fourth quadrant of stress space.

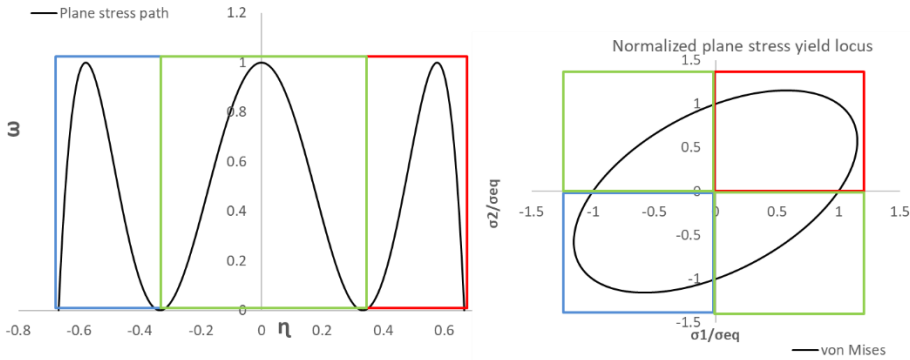


Figure 65: The  $(\omega-\eta)$ -diagram (left) with the plane stress path associated with the normalized von Mises yield locus (right)

For each material point in the forming zone, the stresses stemming from the first order FE simulation can be used to derive a data point in the  $(\omega-\eta)$ -diagram. The idea is to plot all material points of the forming zone onto the  $(\omega-\eta)$ -diagram. Subsequently, the distribution of the cloud of material points needs to be analysed to extract the dominating stress state. Material points lying on the plane stress path exhibit a plane stress condition and can be probed using a sheet metal material test. The orange material point in Figure 66 can be evaluated by conducting a biaxial tensile test. Material points which deviate from the plane stress path are subjected to a 3D stress state, see for example the red material point. Besides the stress state, it is also important in metal forming to consider the imparted plastic deformation. Therefore, the size of the bubbles in the  $(\omega-\eta)$ -diagram corresponds to the magnitude of the equivalent plastic strain in the considered material point. Finally, the material tests can be theoretically shown in this diagram enabling to guide the selection of the most adequate material test.

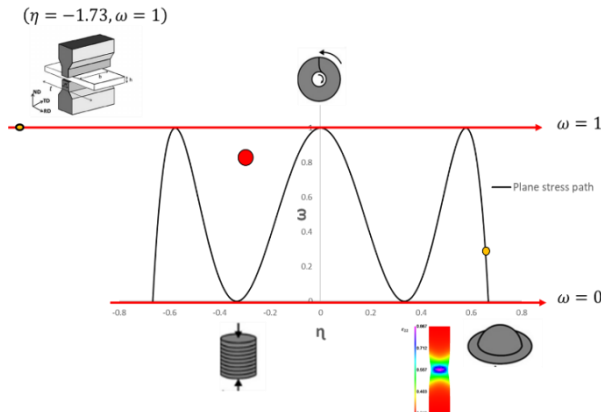


Figure 66: Stress state analysis linked with the material tests

## 9.2 Process-informed method selection

The  $(\omega-\eta)$ -diagram enables to analyse the stress states and plastic strains generated in metal forming processes. The complexity of the deformation history, however, requires an additional metric to extract the dominating stress state. Figure 67 shows the initial indentation of the punch during clinch forming along with the equivalent plastic strain, the triaxiality and the stress metric  $\omega$ . It must be noted that both the stress metrics are averaged to account for the complex deformation history. Instantaneous values of the stress metrics are of limited usefulness here since we are interested in the dominating stress state across all forming stages. To this end, the stress metrics are averaged as follows:

$$\omega^{avg} = \int \frac{\omega(\sigma_{ij})}{\varepsilon_{eq}^{max,pl}} d\varepsilon_{eq}^{pl}$$

$$\eta^{avg} = \int \frac{\eta(\sigma_{ij})}{\varepsilon_{eq}^{max,pl}} d\varepsilon_{eq}^{pl}$$

Figure 68 shows a comparison between instantaneous and averaged stress metrics. It can be inferred that, as opposed to the instantaneous values, the averaged stress metrics yield smooth colour plots. The averaged stress metrics yield consistent results that can be easily understood. For example, the regions that are subjected to a shear-dominated stress state ( $\omega=1$ ) during the course of the deformation are clearly visible when looking at the averaged plot of  $\omega$ . Additionally, the averaging process smooths the results and avoids unwanted numerical scatter. In the remainder of this work, the latter averaging approach is adopted.

The stress states in the upper sheet associated with the forming stage shown in Figure 67 are plotted in the  $(\omega-\eta)$ -diagram shown in Figure 69. It can be inferred that the stress states corresponding to large plastic deformation cluster around  $\omega=1$ . Indeed, the upper sheet is sheared between the punch and the die shoulder. Below the punch, the upper sheet is subjected to biaxial tension, albeit at a significantly lower plastic deformation. In this case, it is clear that the majority of the stress states is shear-dominated. When the joining process proceeds, however, the material state becomes more complicated. In order to objectify the assessment of the dominating stress state, the consumption of plastic work can be considered in identifying the dominating stress state. The left panel of Figure 69 shows the plastic work (% of total consumed plastic work in the process) associated with the different stress states (by binning the stress metric  $\omega$ ). In such a way, it can be concluded that almost 50% of the plastic work relates to shear-dominated stress states. The latter information can guide the selection of the most appropriate material test for flow curve identification. Indeed, for this particular forming stage shown in Figure 67 the IPTT would be preferred to identify the flow curve of the *upper* sheet. The lower sheet, however, is subjected to biaxial tension and therefore the HBT could be used.

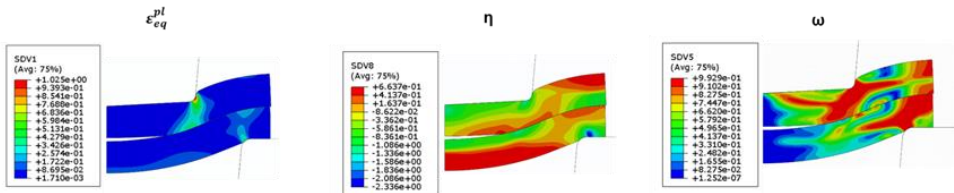


Figure 67: Clinch forming: Stage I. Equivalent Plastic Strain (Upper), Triaxiality (Middle), Stress metric  $\omega$  (Lower).

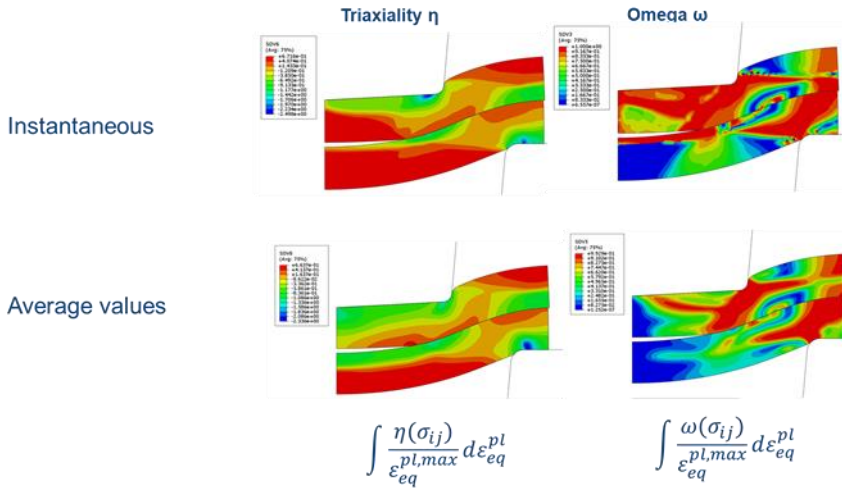


Figure 68: Instantaneous and average values of triaxiality and  $\omega$

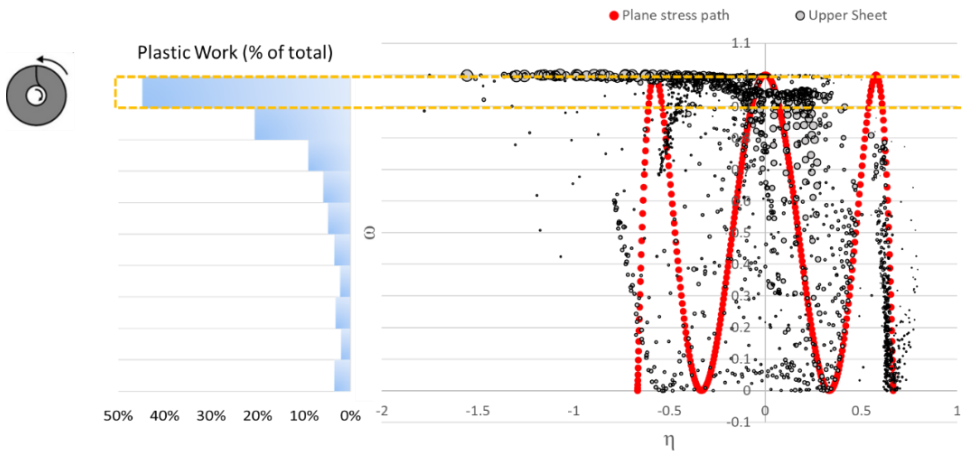


Figure 69: Stress state analysis clinch forming Stage I: Upper Sheet

### 9.3 Clinching

The methodology presented in the previous section is applied to clinch forming of two DC04 sheets with a nominal thickness of 1 mm. Figure 70 shows the equivalent plastic strain, the triaxiality  $\eta$  and the stress metric  $\omega$  at the end of the joining process. The  $(\omega-\eta)$ -diagrams associated with the upper and lower sheet are shown in Figure 71 and Figure 72, respectively. It can be seen that similar stress states occur in the upper and the lower sheet. Assessment of the consumption of plastic work shows that more than 20% of the plastic work is associated with a pure axisymmetric stress state. Indeed, the stress states cluster around ( $\eta=-1.5$ ,  $\omega=0$ ). Due to the punch indentation, the upper sheet consumes more shear-dominated plastic work than the lower sheet. Nevertheless, the dominating stress state in terms of plastic work in both sheets is axisymmetric in nature. As such, the stress state analysis suggests that, both sheets are preferably characterized using a material test, which induces an axisymmetric stress state (assuming symmetry between tension and compression) with  $\eta \approx -1.5$  and an equivalent plastic strain in the order of 2. Obviously, there is no sheet metal test available satisfying the latter conditions. From the considered material test in chapter 7, the SCT is the only axisymmetric test enabling to probe large plastic strains under a negative triaxiality ( $\eta=-1/3$ ). As such, from the stress state analysis, it is expected that the SCT yields the most accurate result for simulating clinching forming of DC04 in DC04 as shown in Figure 70.

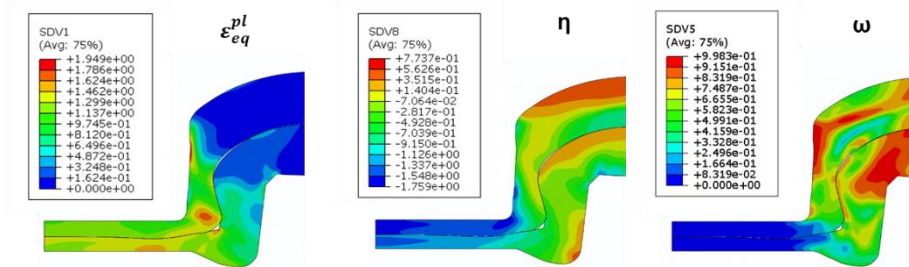


Figure 70: Clinch forming: stress state analysis of DC04 ( $t = 1.0$  mm) in DC04 ( $t = 1.0$  mm) after joining completion

The stress state analysis for EN AW-5182 - EN AW-5182 is very similar to DC04-DC04 case. Given the comparable sheet thicknesses and identical clinching tools used for both cases, this is not surprising. The case EN AW-6082 T6 - EN AW-6082 T6, however, yields a different dominating stress state. Figure 73 shows the equivalent plastic strain, triaxiality and  $\omega$  for this case. The associated  $(\omega-\eta)$ -diagrams for the upper and lower sheet are shown Figure 74 and Figure 75, respectively. It can be seen that the predominant deformation mode is shear-dominated for both sheets. The case EN AW-6082 T6- EN AW-6082 T6 requires tools that prevent premature fracture as EN AW-6082 T6 exhibits limited ductility. Clearly, this yields a different deformation mode than the DC04-DC04 case (and the case EN AW 5182 - EN AW 5182) with more weight to shear-dominated deformation.

Figure 76 shows the stress state analysis of the dissimilar joining case CR330Y590T-DP in EN AW 5182. Figure 77 and Figure 78 show the associated  $(\omega-\eta)$ -diagrams. For this case, the upper sheet can be divided in two regions: an axisymmetric stress state under the punch and a shear-dominated stress state in the neck region. It would be justified to calibrate the upper sheet with SCT or the IPTTT. The stress state in the lower sheet is evenly distributed with a clear peak around the *omega bin*  $\omega = 0.6 \rightarrow 0.7$ , and, consequently, a shear-dominated material test is preferable.

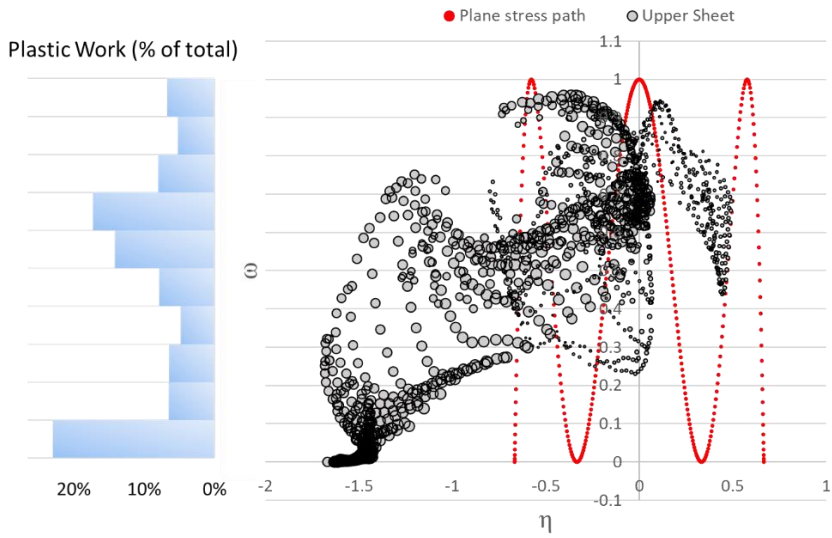


Figure 71: Stress state analysis clinching forming stage IV DC04-DC04: Upper sheet

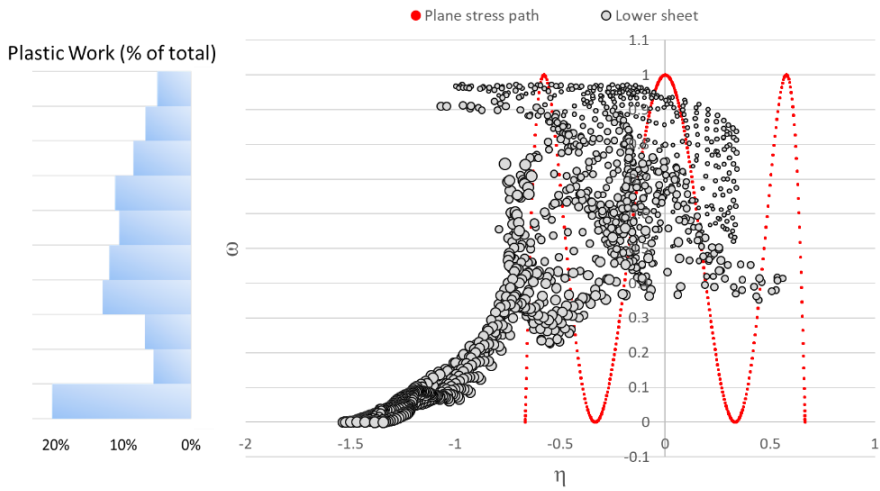


Figure 72: Stress state analysis clinching forming stage IV DC04-DC04: Lower sheet

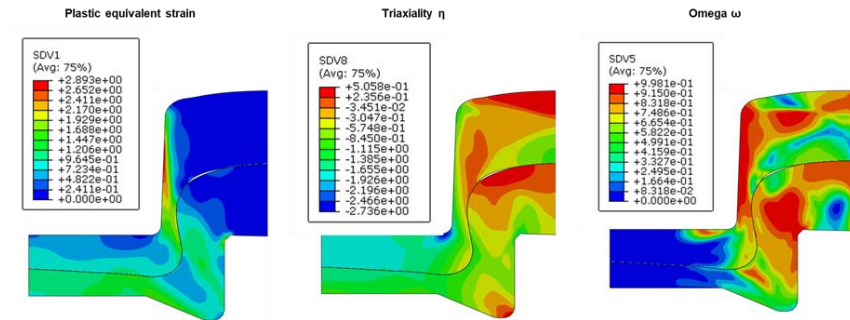


Figure 73: Clinch forming: stress state analysis of EN AW-6082 T6 ( $t = 1.5$  mm) in EN AW-6082 T6 ( $t = 1.5$  mm) after joining completion

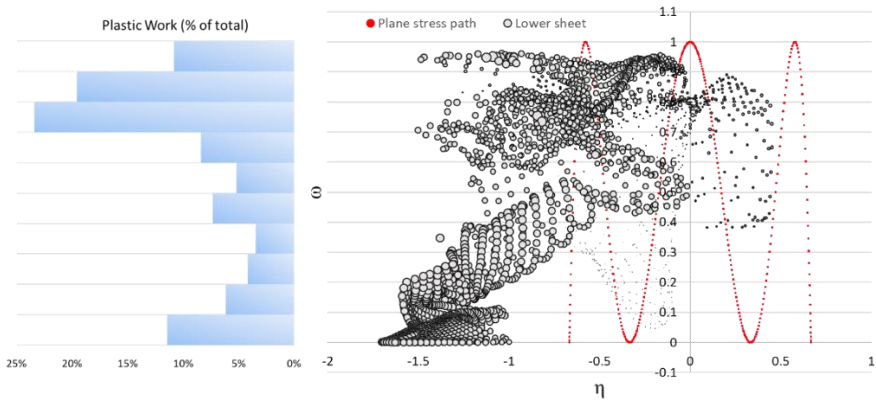


Figure 74: Stress state analysis clinching forming stage IV EN AW 6082- EN AW 6082: upper sheet

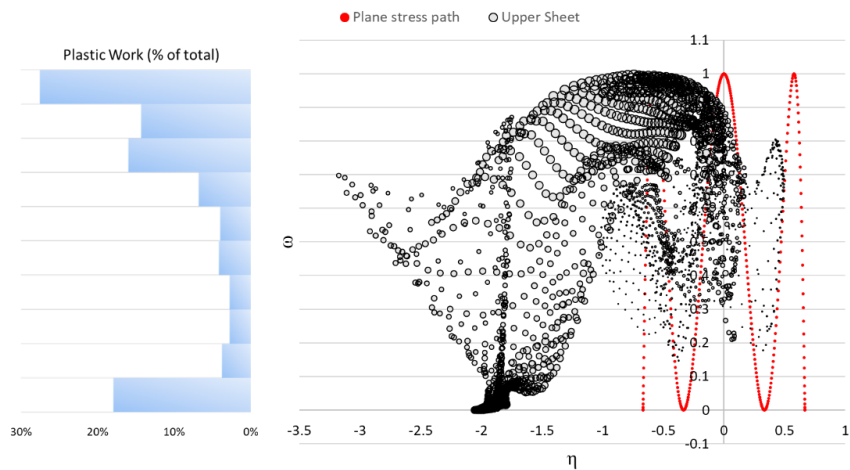


Figure 75: Stress state analysis clinching forming stage IV EN AW 6082- EN AW 6082: lower sheet

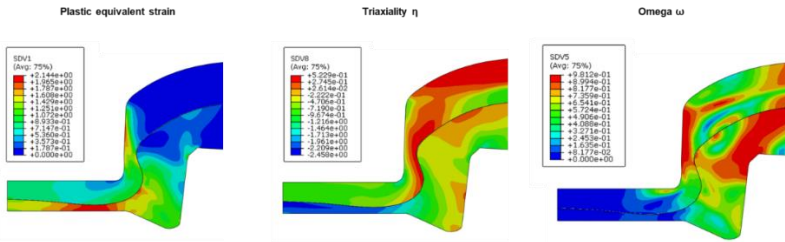


Figure 76: Clinch forming: stress state analysis of CR330Y590T-DP ( $t = 1 \text{ mm}$ ) in EN AW 5182 ( $t = 1 \text{ mm}$ ) after joining completion

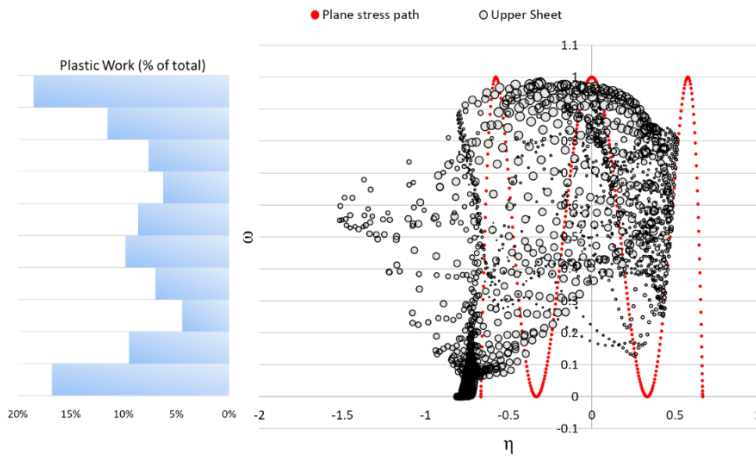


Figure 77: Stress state analysis clinching forming stage CR330Y590T-DP EN AW 5182: upper sheet (CR330Y590T-DP)

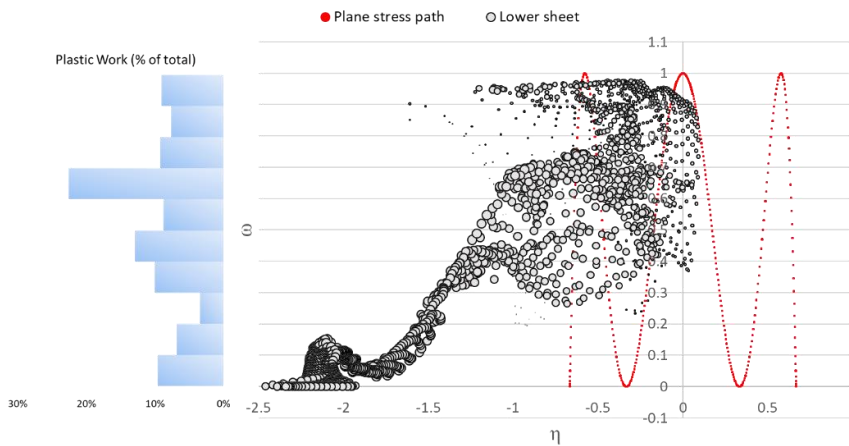


Figure 78: Stress state analysis clinching forming stage IV CR330Y590T-DP - EN AW 5182: lower sheet (EN AW 5182)

## 9.4 Self-pierce riveting

Figure 79 shows the calculated plastic equivalent strain, triaxiality and omega for the end of the SPR process with a thorn die of EN AW-5182 ( $t = 1.1$  mm) in EN AW-5182 ( $t = 1.1$  mm).

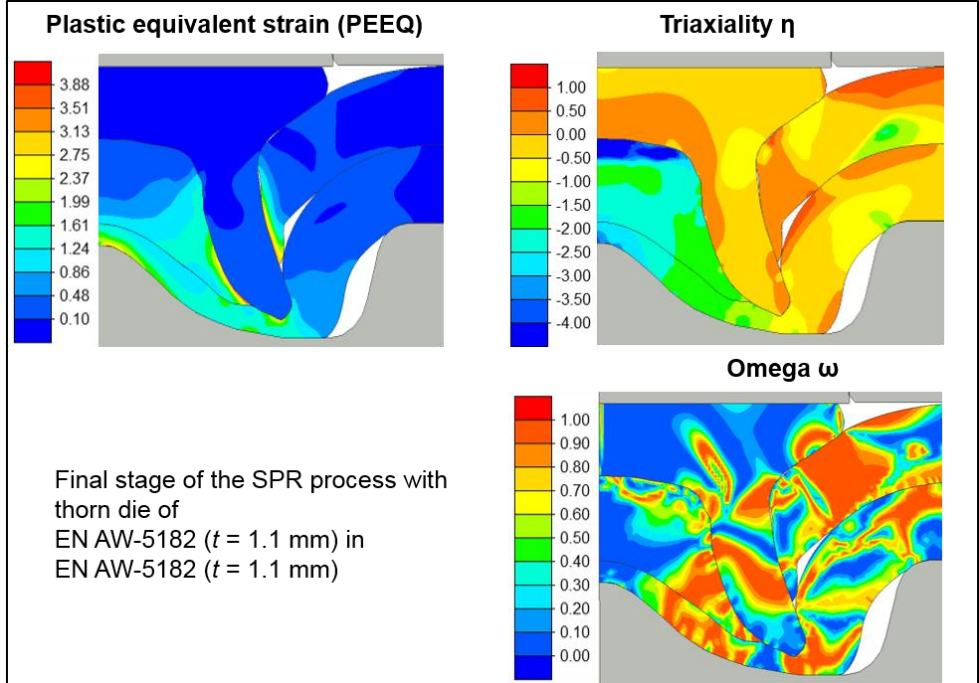


Figure 79: Plastic equivalent strain, triaxiality and omega for the SPR process of EN AW-5182 ( $t = 1.1$  mm) in EN AW-5182 ( $t = 1.1$  mm)

Recording to the calculated results the highest strains occur besides the rivet leg and in the middle of the die-sided sheet. In terms of triaxiality, the highest pressure occurs under the rivet head in the punch-sided sheet. Outside the area under the rivet also tensile stresses are calculated. The instant omega values are quiet diverse for both the sheets as well as the rivet.

In addition to the visualization of the strain-stress-characteristics of the joint, Figure 80 also shows the data analysis for each finite element of the process simulation and the relationships between plastic equivalent strain and omega as well as triaxiality and omega. From Figure 80, a can be derived that calculated strain and shear characteristics are very comparable for both top and bottom sheet. The maximum strain is about  $\varphi_{max} \approx 3.9$ , but average strain is only  $\varphi_{ave} \approx 0.73$  when considering all elements in this process stage.

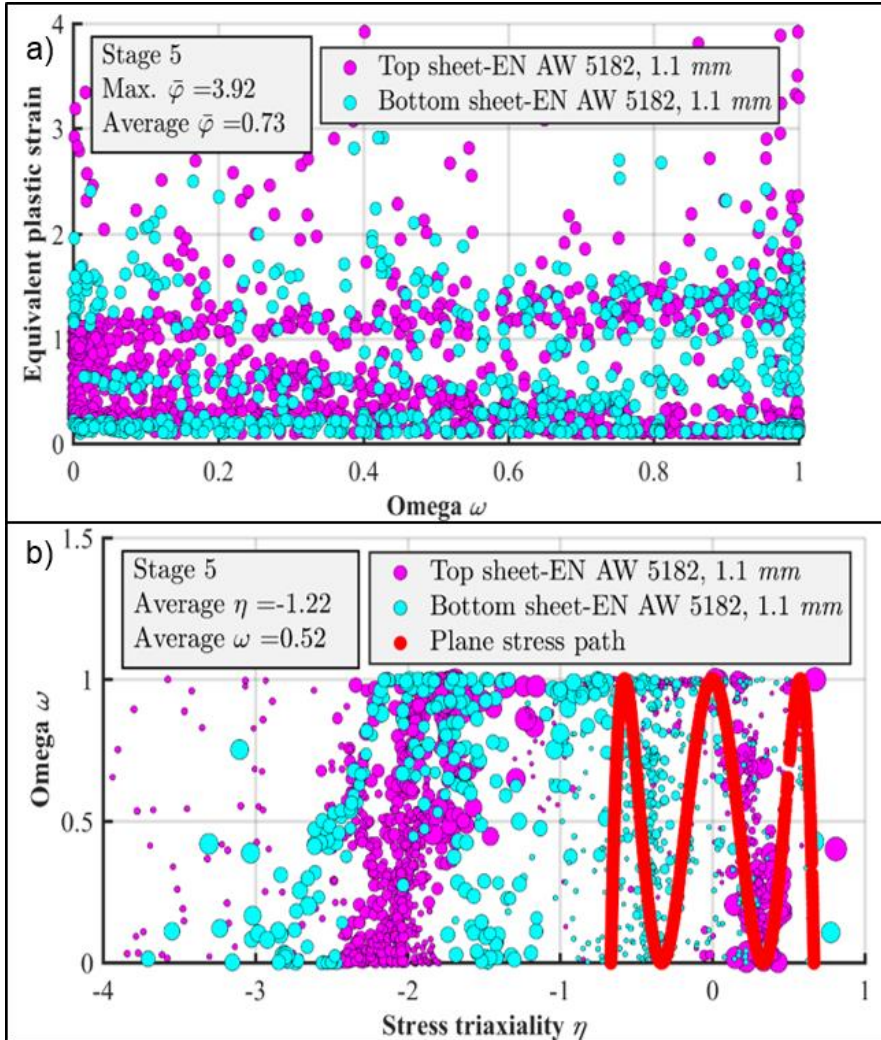


Figure 80: Diagrams for plastic equivalent strain over omega and omega over triaxiality for all elements the SPR simulation of EN AW-5182 ( $t = 1.1$  mm) in EN AW-5182 ( $t = 1.1$  mm)

In the omega-stress triaxiality diagram (Figure 80, b) significant differences between the sheets are visible. In the bottom sheet mainly negative triaxiality occurs while also tensile stresses occur in the top sheet. Overall, however, a negative average triaxiality of  $\eta_{ave} \approx -1.2$  can be determined. In both sheets the average shear stress components are almost balanced with an average omega of  $\omega_{ave} \approx 0.5$ .

Figure 81 shows the calculated plastic equivalent strain, triaxiality and omega for the end of the SPR process with a thorn die of DC04 ( $t = 1.0$  mm) in DC04 ( $t = 1.0$  mm).

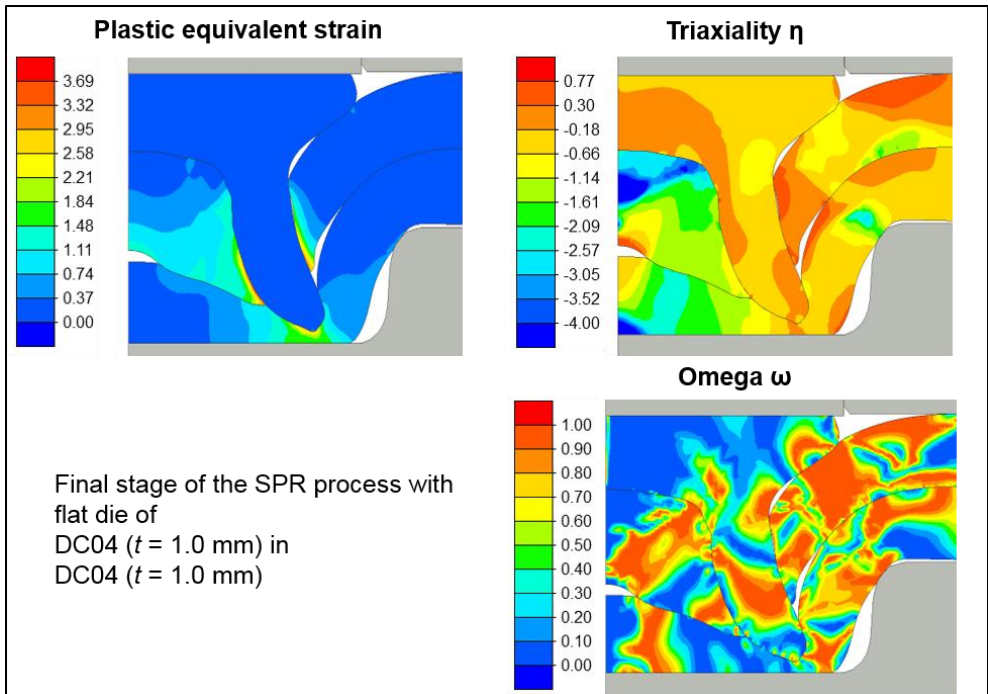


Figure 81: Plastic equivalent strain, triaxiality and omega for the SPR process of DC04 ( $t = 1.1$  mm) in DC04 ( $t = 1.1$  mm)

In comparison to the SPR process of EN AW-5182 ( $t = 1.1$  mm) in EN AW-5182 ( $t = 1.1$  mm) in which a thorn die was used (Figure 79), differences in terms of the triaxiality conditions can be determined. Thereby the pressure in the area under the rivet head is with the flat die geometry much lower than with the thorn die. Also due to the missing thorn geometry the plastic equivalent strain is much lower in the die-sided sheet. In regards to the omega, however, the calculated results are comparable to the aluminum joint (Figure 79).

The influence of the flat die geometry can also be seen in the analysis of the calculated strain-stress data (Figure 82). On consideration of plastic equivalent strain (Figure 82, a) the maximum ( $\varphi_{max} \approx 3.7$ ) as well as the average for all elements ( $\varphi_{ave} \approx 0.73$ ) is lower than the SPR joint with the thorn die (Figure 79, a).

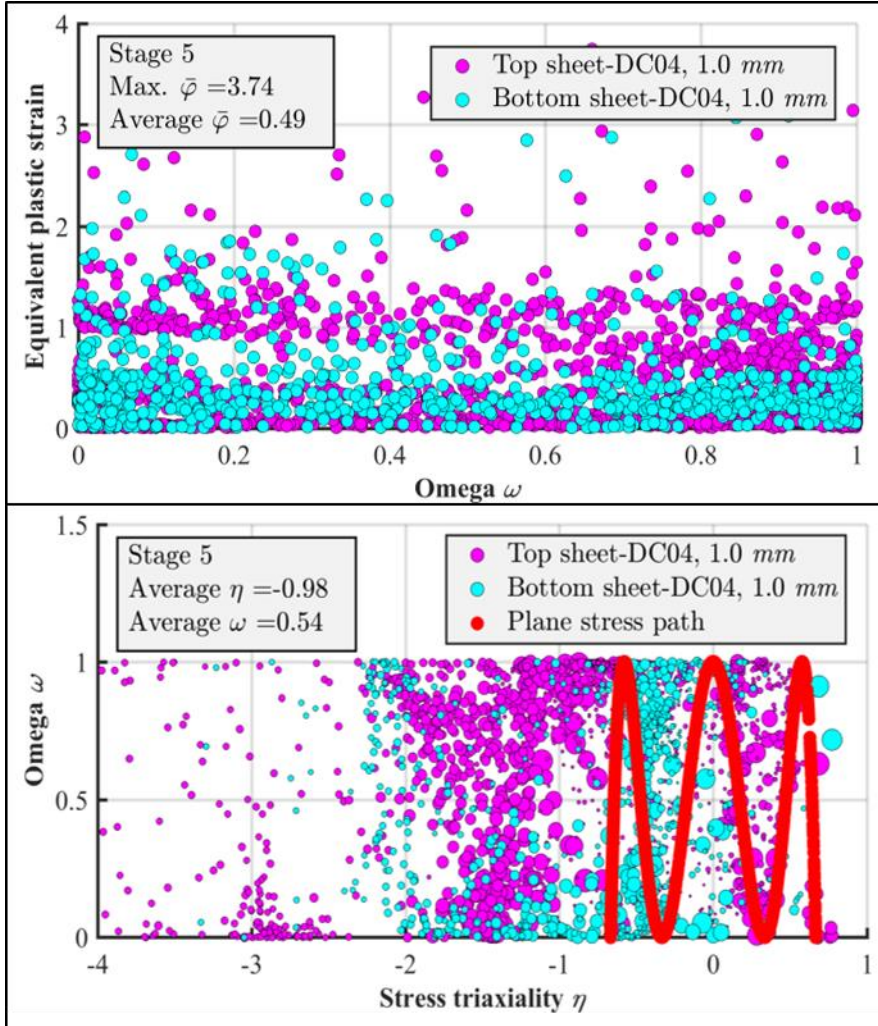


Figure 82: Diagrams for plastic equivalent strain over omega and omega over triaxiality for all elements the SPR simulation of DC04 ( $t = 1.0$  mm) in DC04 ( $t = 1.0$  mm)

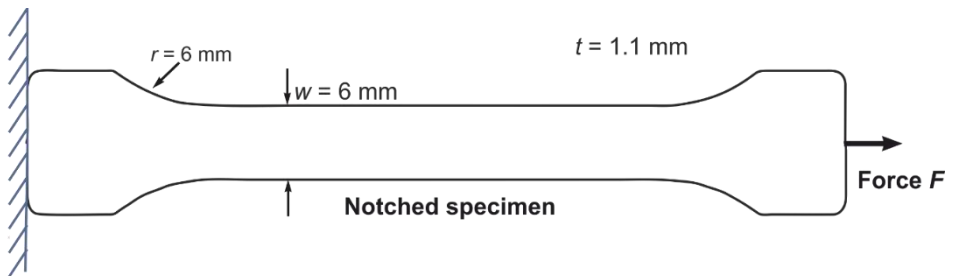
Also the average triaxiality ( $\eta_{ave} \approx -1$ ) is lower when using a die without a thorn (Figure 79, b). A significant influence on the relationship between shear and plane stress cannot be determined since the average omega of  $\omega_{ave} \approx 0.5$  is comparable to the SPR joint with thorn die.

## 9.5 Material characterization tests

In this section, the stress state analysis is applied to the considered material tests. Theoretically, the stress state probed in a material test is unique and remains constant throughout the test. In other words, in theory the material test takes a unique position in the  $(\omega-\eta)$ -diagram. In practice, however, deviation from the homogenous stress state can occur. Especially the material tests which involve friction might exhibit a heterogeneous stress state in the measurement gauges.

### 9.5.1 Extended Tensile Test

A simple FEM model (Figure 83) has been constructed in ANSYS workbench and used to investigate the stress-state in a uniaxial tensile test. A standard notched sheet of thickness 1 mm is axially stretched from one direction while keeping the other end fixed and force  $F$  is applied until the point of necking.



#### Fixed support

Figure 83: Structure of the simulation model analysis of the uniaxial tensile test

The visualization the calculated plastic strain, triaxiality and omega are shown in Figure 84.

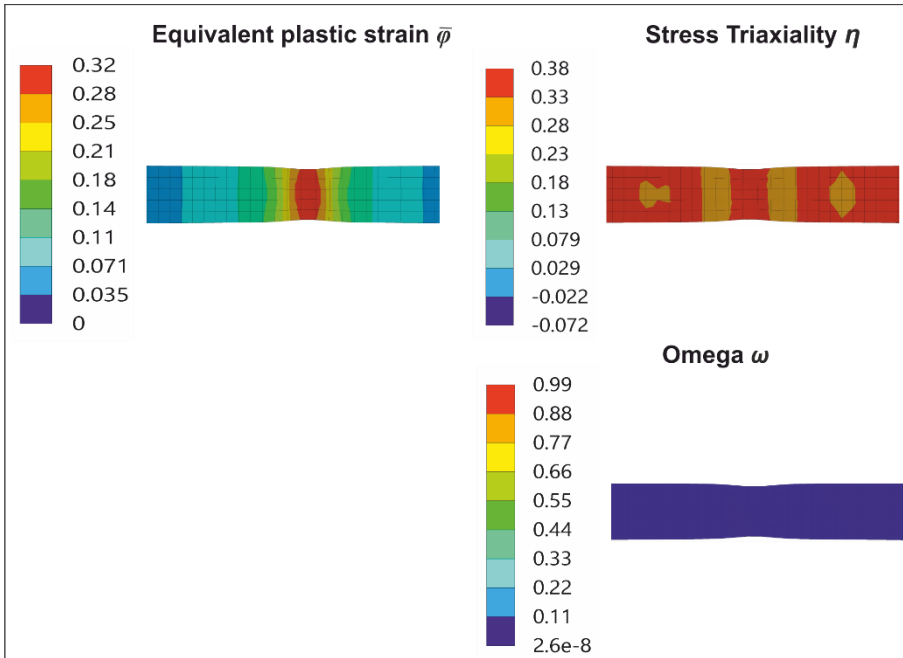


Figure 84: Calculated equivalent plastic strain, stress triaxiality and omega for the tensile test

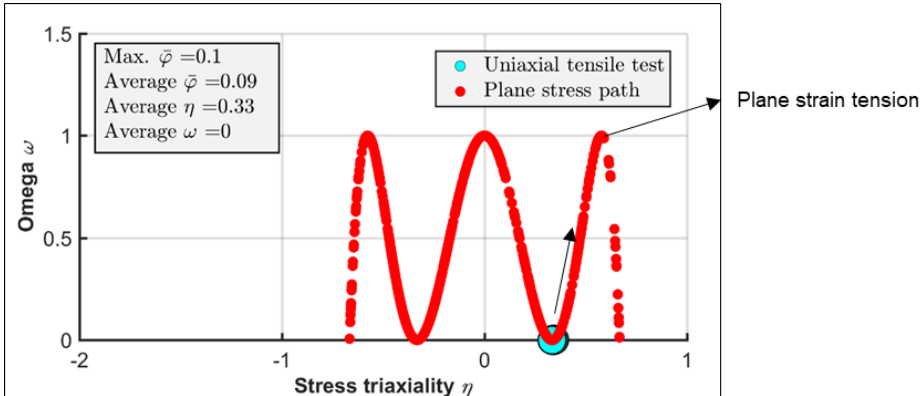


Figure 85: Distribution of strain elements in relation to stress triaxiality and omega for the tensile test

Figure 84 shows the relation of equivalent plastic strain as bubble size with omega  $\omega$  in y-axis and the triaxiality  $\eta$  in x-axis for all nodes. It can be viewed that maximum strain that could be attained is 0.3 and the elements have omega being almost zero and triaxiality being positive and around 0.3. These results show that the nature of stress state of material is tensile and agrees with the theory related to the tensile test. In practice, for ductile materials, equivalent plastic strains of the order 0.9 can be probed in the diffuse neck. In the extended tensile test, the strain path evolves as follows:

1. Before maximum load: uniaxial tension
2. During diffuse necking: biaxial tension
3. Local necking: plane strain tension

This implies that during the extended tensile test the stress state gradually evolves towards plane strain tension. The latter is schematically shown by the black arrow in Figure 85.

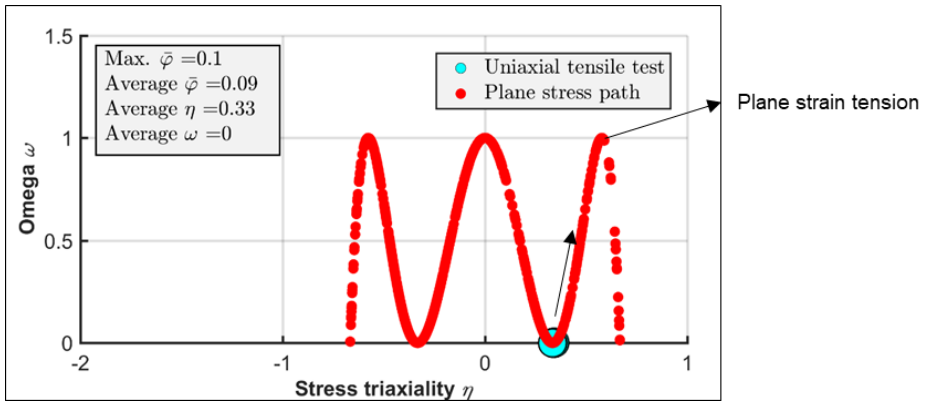


Figure 85: Distribution of strain elements in relation to stress triaxiality and omega for the tensile test

### 9.5.2 Stack compression test

For the numerical analysis of the stress state of the stack compression test (SCT) a FEM model has been constructed in ANSYS to replicate the test with three circular sheets. The sheets are placed between opposing two dies, upper moving die and lower stationary die. The upper die compresses the sheets against the lower die and deforms till half of the total thickness of the sheets. The contact friction between the tools and sheets have been evaluated by [Cop10]. The friction of coefficient  $\mu_t$  between the sheets and the tools is taken 0.19 and friction of coefficient  $\mu_i$  between the sheets is taken 0.1.

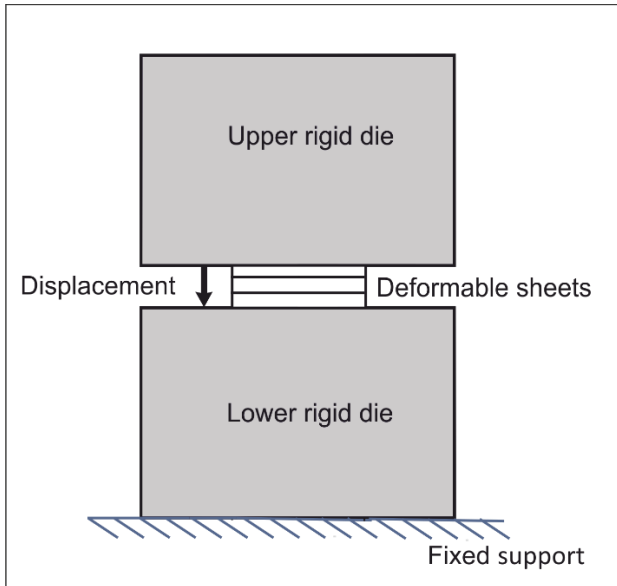


Figure 86: Structure of the simulation model for analysis of the stack compression test

Figure 87 shows results for equivalent plastic strain, stress triaxiality and omega. The specimen tends to bulge a little due to higher friction with strain reaching up to 0.6. Figure 88 describes the distribution of elements in terms of triaxiality and omega. The average  $\eta$  is negative and approximately equal to -0.5. Thus, the material at compression test are biaxial and compressive in nature. Also, average value of  $\omega$  is almost zero stating no elements have shear stresses and thus, corroborating with the theory of the SCT.

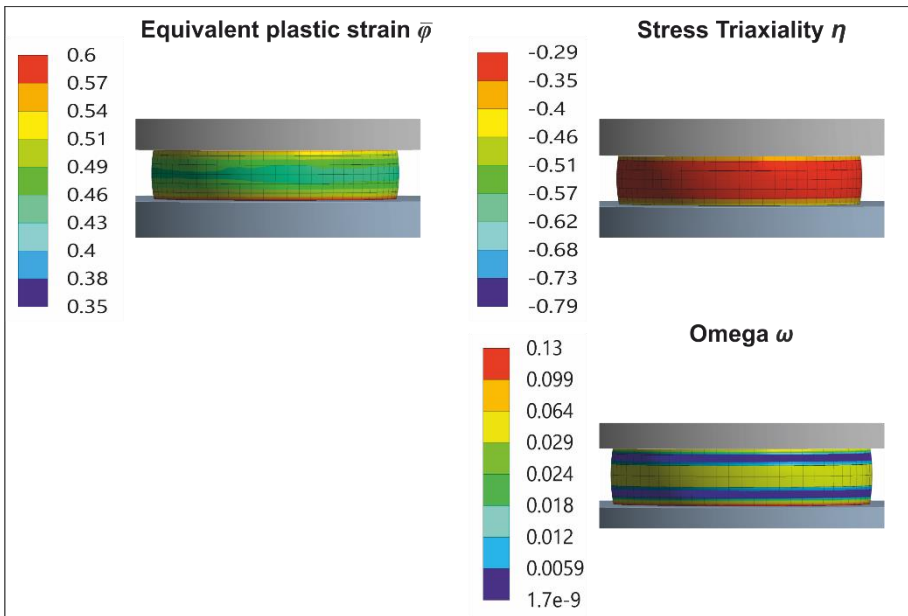


Figure 87: Calculated equivalent plastic strain, stress triaxiality and omega for the stack compression test

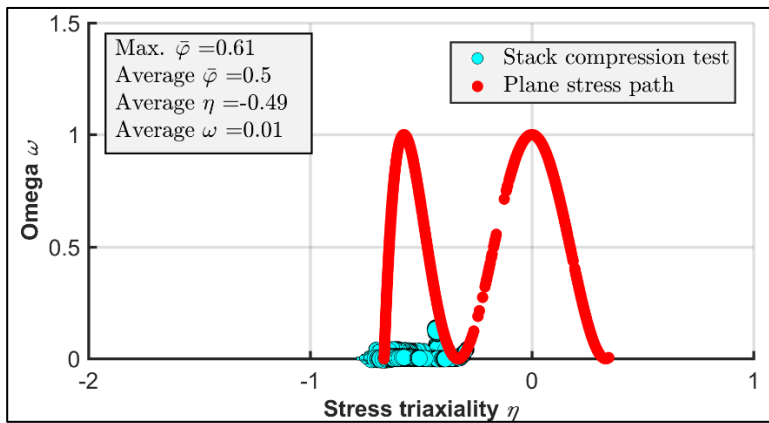


Figure 88: Calculated distribution of strain elements in relation to stress triaxiality and omega for stack compression test

### 9.5.3 Plane strain compression test

Similarly, the FEM model for the plane strain compression is developed in ANSYS workbench. The model with its dimension can be seen in Figure 89. The sheet is placed between opposing two dies, upper moving die and lower stationary die, however in this test the dies have thin indenters instead of large surface area. Thus, the effect of friction on the specimen is reduced as compared to stack compression test. The upper die compresses the sheets against the lower die until thickness of the sheet is halved. The friction of coefficient  $\mu$  between the sheet and the tools are has been taken 0.1.

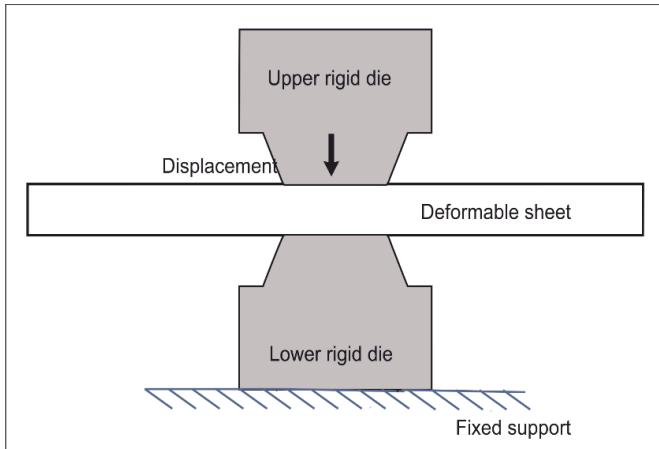


Figure 89: Structure of the simulation model for analysis of the plane strain compression test

The effect of friction can also be seen in Figure 90 evident from the bulging of the specimen at the edges of the tools. Since the deformation in width direction is restricted, strain  $\varphi_3$  is zero. The strain in axial direction  $\varphi_1$  reaches upto 0.67 while in longitudinal direction  $\varphi_2$  is up to 0.09 and the overall equivalent plastic strain  $\bar{\varphi}$  is 0.79.

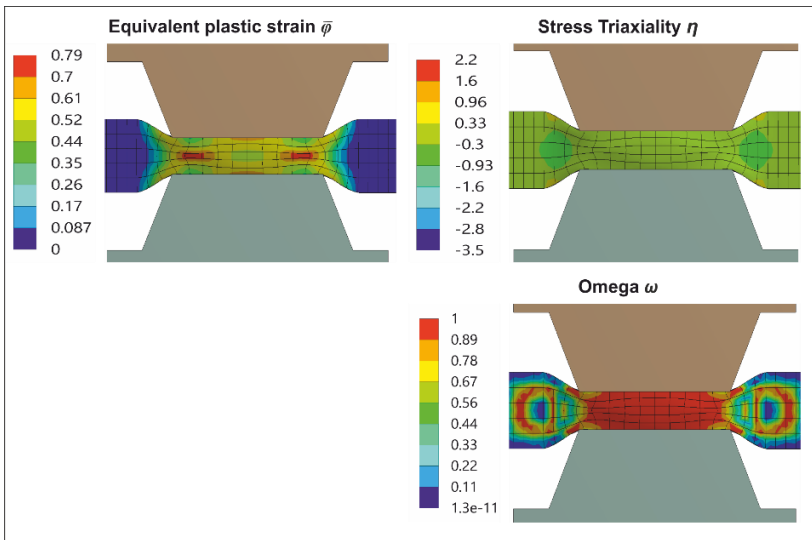


Figure 90: Calculated equivalent plastic strain, stress triaxiality and omega for the plane strain compression test

The Figure 91 describes the distribution of elements in terms of triaxiality and omega. In contrast to stack compression test, it can be seen that most of the large bubbles are at higher  $\omega$  (avg  $\omega = 0.7$ ) with  $\eta$  between -0.2 and -0.9. The average  $\eta$  is negative and approximately equal to -0.25. Thus it can be concluded that most of the elements with higher strain are either in shear states or biaxial compression states while the elements with lower strain are tensile in nature. Nevertheless, the predominant deformation mode is clearly shear-dominated under a negative triaxiality.

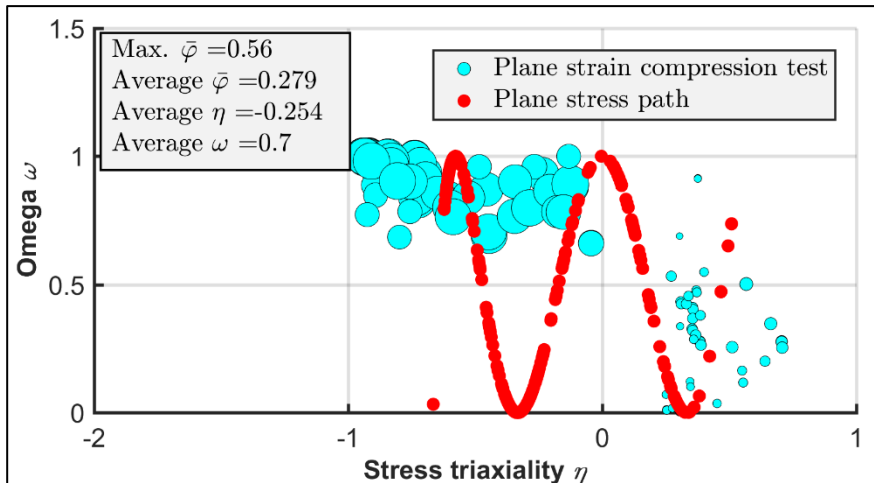


Figure 91: Calculated distribution of strain elements in relation to stress triaxiality and omega for the plane strain compression test

#### 9.5.4 In-plane torsion test

For stress-state analysis of the in-plane torsion test, a simulation model is constructed in ANSYS workbench with the boundary conditions as similar to the experiment. The inner surface of the grooved specimen is kept fixed while the outer surface is rotated by angle of  $24^\circ$  as shown in Figure 92. This produces a plastic strain near the grooved region.

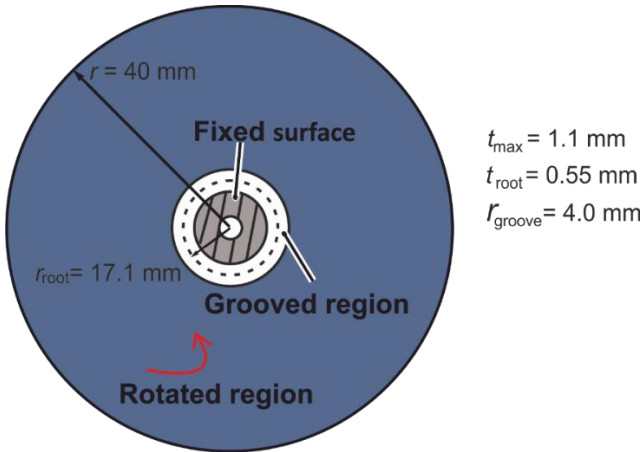


Figure 92: Structure of the simulation model for numerical analysis of the in-plane torsion test

The calculated distribution of the plastic strain, stress triaxiality and omega is shown in Figure 93 and Figure 94. The middle region of the groove has the maximum equivalent strain  $\phi$  reaching up to 1.26. In the figures, it can be seen that average omega is close to one and while triaxiality remaining close to zero. Thus, it can be concluded that the material is in a pure shear as the theory suggests.

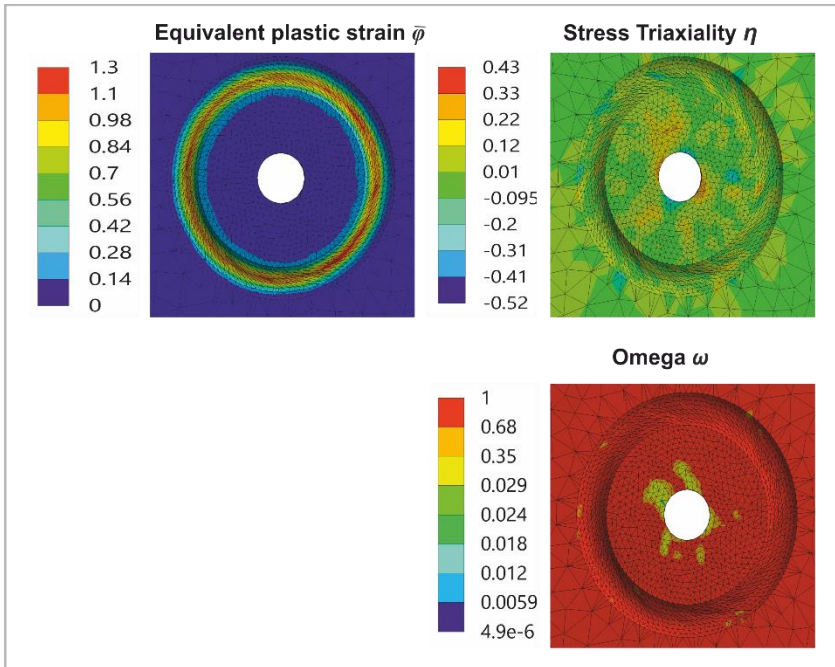


Figure 93: Calculated equivalent plastic strain, stress triaxiality and omega for the in-plane torsion test

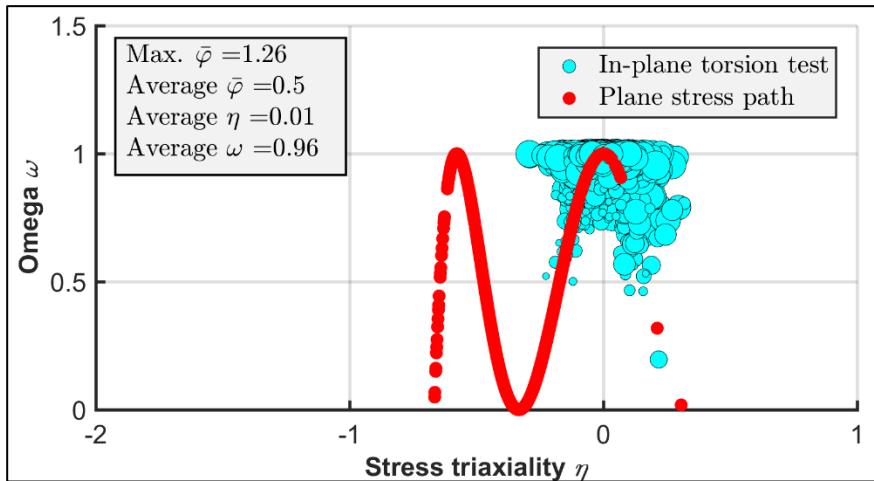


Figure 94: Calculated distribution of strain elements in relation to stress triaxiality and omega for the in-plane torsion test

### 9.5.5 Hydraulic bulge test

The stress-state for this test can be analysed by constructing a FEM model as seen in with conditions similar to the actual test. The stress state involved in hydraulic bulge test is biaxial tension. A circular blank of sheet of 1 mm is placed on a hollow rigid die with a fixed blankholder on the top. Displacement of both die and blank holder is kept zero. Pressure of increasing magnitude from 0 to 0.3 MPa is applied at the centre of the sheet. In the model, draw bead can be replicated by fixing the nodes of the specimen at the outer surface of the specimen as shown in Figure 95.

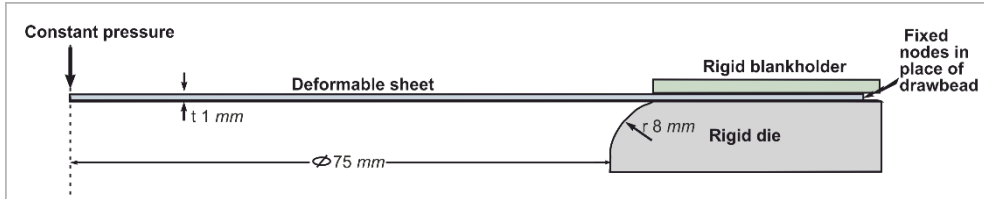


Figure 95: Structure of the simulation model for numerical analysis of the hydraulic bulge test

Only the elements near the bulge area ( $r = 7.5$  mm) are extracted for the analysis. The distribution of plastic strain triaxiality and omega on the model are shown in Figure 96. The maximum strain of about 0.6 is close to the centre of the bulge and have the triaxiality of 0.7. The omega for almost the elements are close to zero.

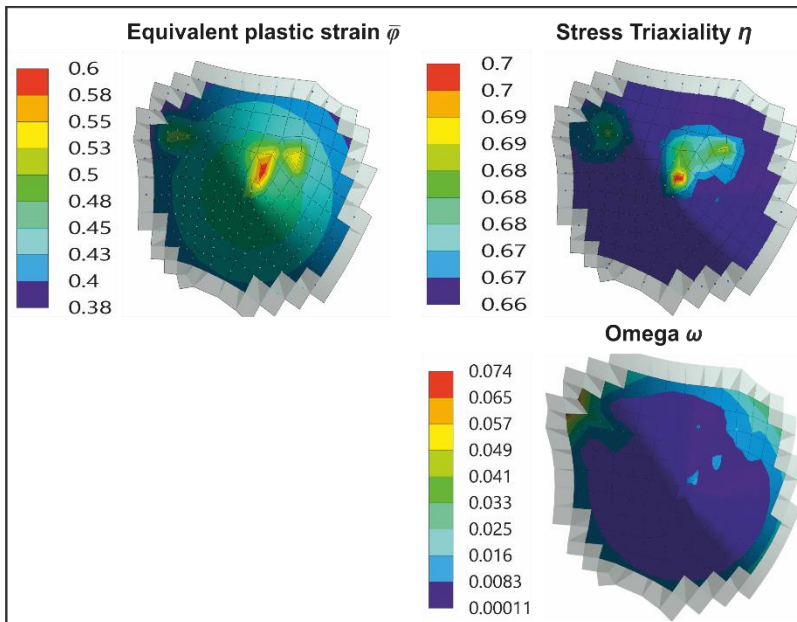


Figure 96: Calculated equivalent plastic strain, stress triaxiality and omega for the hydraulic bulge test

The visualisation for triaxiality and omega for each element of the simulation can be seen in Figure 97. The average plastic strain reached in the bulge area is 0.44 with omega equating to zero. Since the triaxiality is positive and higher than 0.3, it can be understood that the stress states are in biaxial tension and similar to the theory.

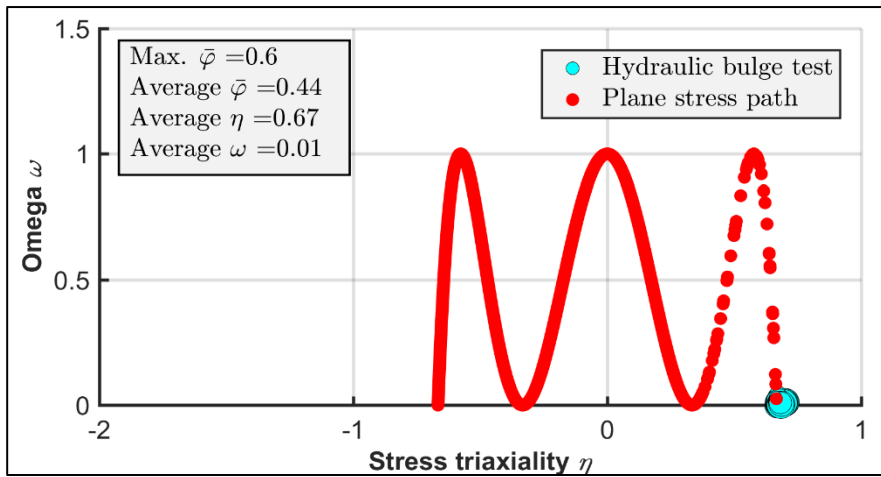


Figure 97: Calculated distribution of strain elements in relation to stress triaxiality and omega for the hydraulic bulge test

### 9.5.6 Summary

Finally, results of all the tests can now be combined and represented in the plane stress path as shown in Figure 98 . The diagram shows the resulting stress states for the considered mechanical tests in relation to the plane stress path. These results can be used to assign the tests to the mechanical joining methods.

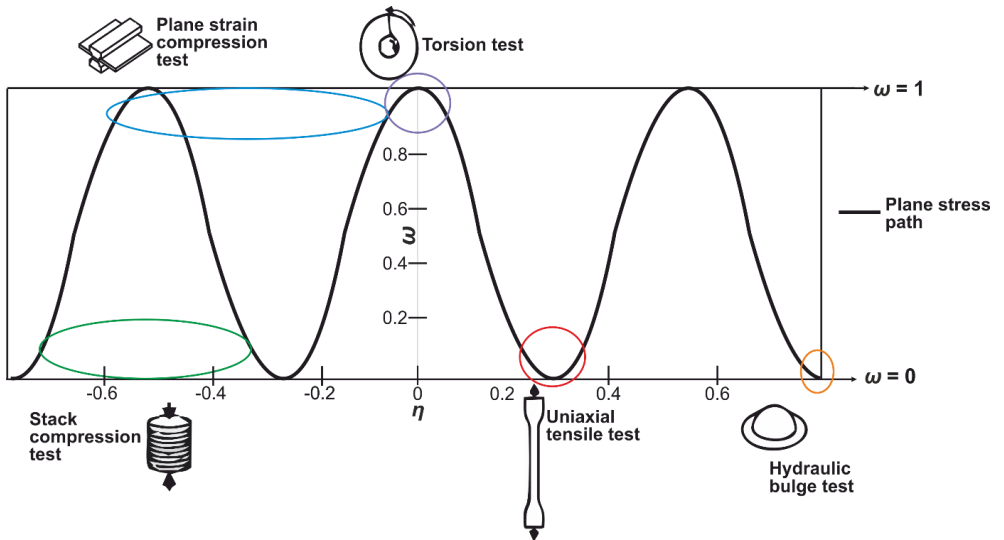


Figure 98: Plane stress path with stress state results of different mechanical tests. After [BON18]

## 9.6 Comparison of joining processes and material tests

From the results from the numerical analysis in chapter 9, the stress and strain state conditions of the joining methods SPR and clinching as well as the material tests can be compared. The summary of these investigations can be found in Figure 99. The average values of  $\eta$  and  $\omega$  are used to construct Figure 99. In addition, for SPR and Clinching the case DC04 in DC04 was used.

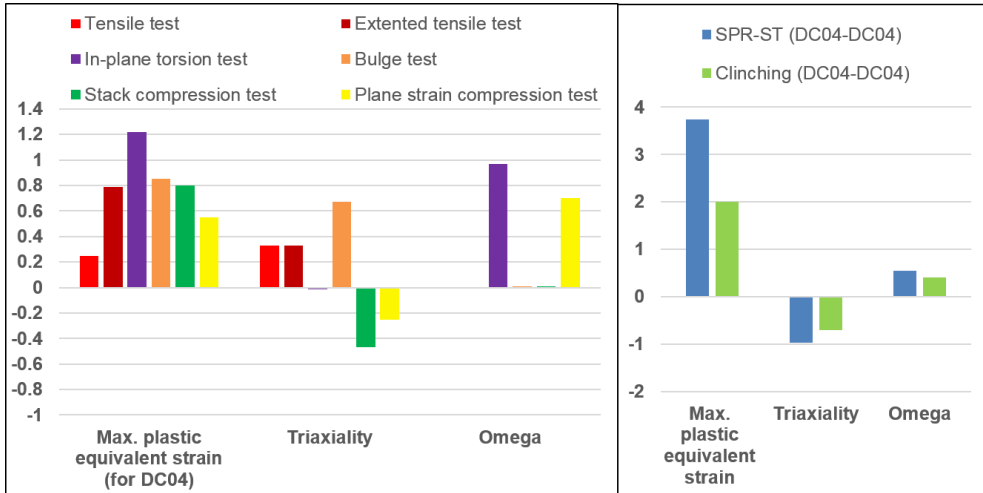


Figure 99: Comparison of the max. plastic strain, stress triaxiality and omega for the considered material tests and joining methods SPR and clinching

It can be stated that the maximum plastic strain in the joining methods are higher than in the material characterization methods. This is not necessarily a problem as was shown in section 7.2. In the tests performed here, the in-plane torsion test shows the highest achievable plastic strains. The IPTT is therefore very valuable to understand the strain hardening behaviour in the post-necking regime. Moreover, the IPTT enables to select an adequate hardening law. Although the IPTT is superior in terms of maximum attainable plastic strain, the considered materials tests are all deemed appropriate to identify the large strain flow curve in joining by forming.

In terms of stress state, Figure 99 clearly shows that the high compressive stresses or negative triaxialities during joining are beyond the range of the material tests. The stack compression test with  $\eta \approx -0.5$  has the best comparability with the joining methods, followed by the PSCT. When comparing the stress metric  $\omega$ , the plane strain compression test ( $\omega \approx 0.7$ ) has the best comparability with the joining methods ( $\omega \approx 0.4 - 0.7$ ). This analysis leads to the conclusion that there is no material test which is 100% comparable with the mechanical joining methods SPR and clinching for DC04 in DC04.

When resorting to the extended stress state analysis using the consumed plastic work, the dominating  $\omega$  equals 0 for clinching. In that case, the selection is driven by two constraints:

1. Select a test that enables to probe true plastic strains in the order of 0.7
2. Select a test with ( $\eta \approx -0.5$ ,  $\omega \approx 0$ )

This conclusion is then straightforward: the SCT is most optimal test here (i.e. clinching case DC04 in DC04). In order to validate the presented selection strategy (see chapter 13), all materials tests were conducted to determine the large strain flow curves of the considered

materials (see chapter 11). Given that the SCT is a promising material test for joining by forming, the following chapter embarks on a numerical and experimental study to optimize the SCT for the specific needs of joining by forming.

## 10 Experimental and numerical study of the stack compression test

### 10.1 Initial state and parameters of the stack compression test

In Figure 100 the occurring max. plastic strain, triaxiality and omega of SPR, clinching and the stack compression test (SCT) are compared.

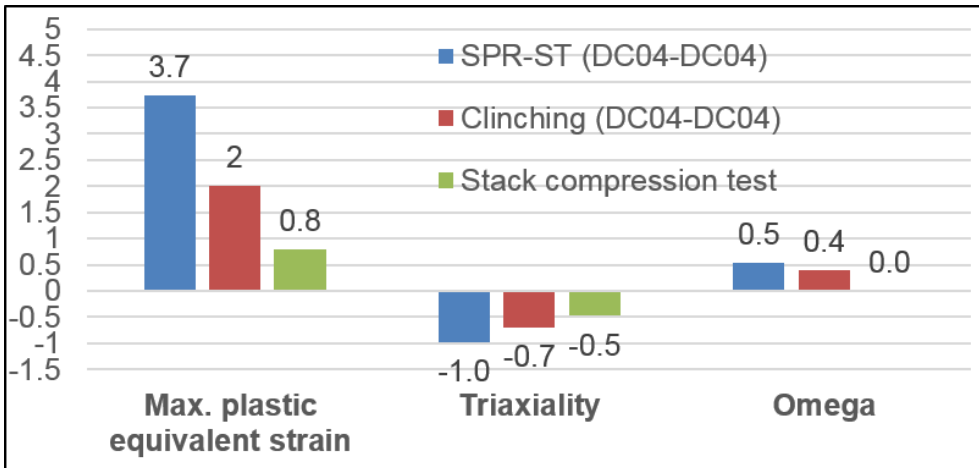


Figure 100: Comparison of simulated max. plastic strain, triaxiality and omega of SPR, clinching and the stack compression test

When comparing the results, it becomes clear that both higher achievable strain values and a reduction in triaxiality of the SCT would result in improved comparability with mechanical joining methods. This is the aim of the following investigations.

For this purpose the influenceable properties of the SCT (Figure 101) are analysed experimentally and numerically. The number and diameter of the discs are varied. In addition, the influence of the production process for manufacturing the discs and the friction between the discs and the tools are analysed.

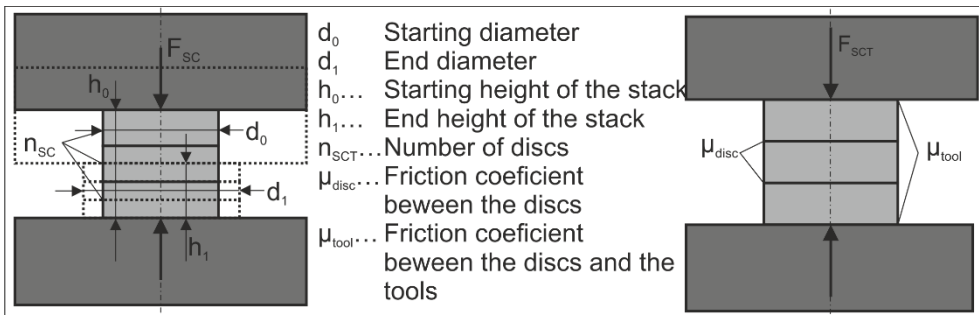


Figure 101: Characteristics of the stack compression test

## 10.2 Manufacturing process of the discs

The following criteria are important for the selection of the round blank manufacturing process:

1. The influence of the process on the surface layer of the disc
2. A heat affected zone near the edges must be avoided in order to maintain the homogeneity of the disc
3. Reproducibility
4. High dimensional accuracy in terms of cylindricity
5. Form deviations lead to measuring errors

As a result of these requirements and tests the eroding and turning processes are selected.

Another possible method is water jet cutting. However, this is a similar problem to that of punching the discs. Due to the characteristics of the process, a conical shape of the cut edges must be expected. This should be less than the deformation caused by punching.

The comparison of the manufacturing processes turning and eroding is done by comparing a steel or an aluminium material. Since the ratio of height and diameter is irrelevant for the selection of the process, the tests are carried out with a diameter of 9 mm and a stack height of between three and four discs.

Figure 102 shows the respective flow curves with DC04 and EN AW-5182. It should be noted that the production process plays a subordinate role in the compression tests with steel discs, as the flow curves obtained deviate only minimally. However, it is clearly visible in Figure 102 (right) that the turned specimens fail earlier in stack compression tests with aluminium alloy discs.

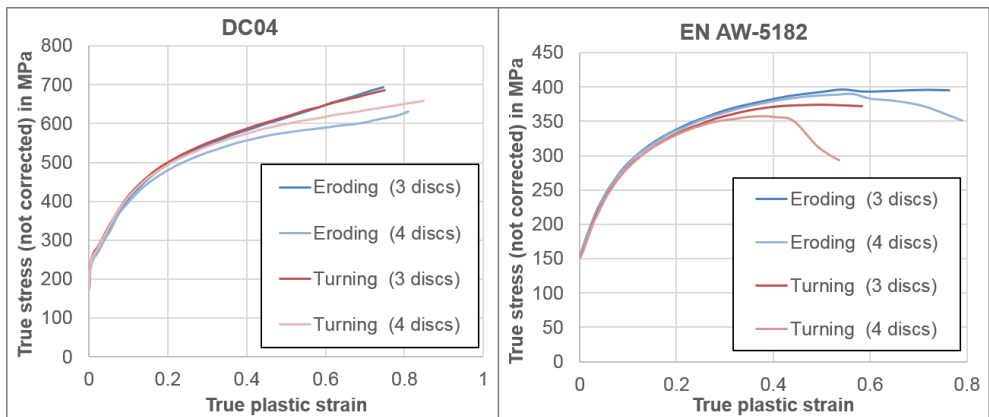


Figure 102: Influence of disc manufacturing process on flow curve quality from the stack compression test for DC04 and EN AW-5182

This observation can only be explained by the fact that the turned production of the discs may have produced tiny notches in the edge area, which lead to cracks due to the tangential tensile stresses generated in the test (see Figure 103).

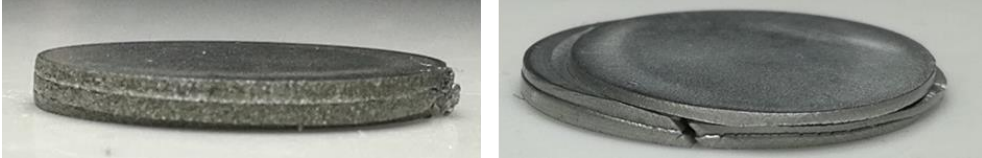


Figure 103: Comparison of eroded (left) and turned (right) discs from EN AW-5182

Also in a microscopic analysis by means of SEM (scanning electron microscope), no influence on the edge area could be determined by the manufacturing of the discs (Figure 104).

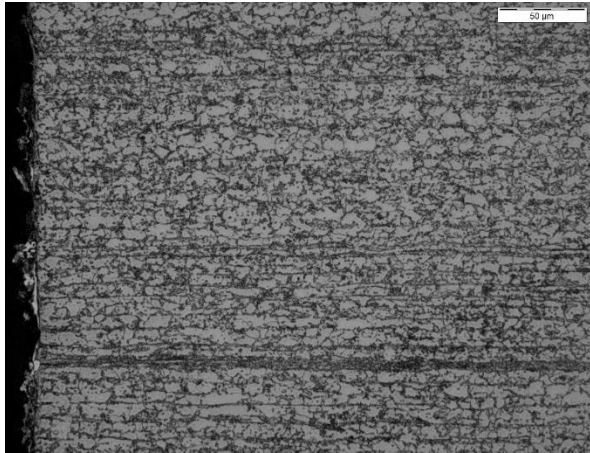


Figure 104: SEM image of the edge area of a CR330Y590 disc after eroding

### **10.3 Influence and correction of friction**

Due to the contact between tool and discs as well as between the discs themselves, a certain influence of friction cannot be avoided in SCT despite various technical approaches to friction reduction. In the following numerical studies, the individual influence of the different friction partners on the force curve in the compression test is analysed. The simulation model explained in chapter 9.5.2 was used for the calculations.

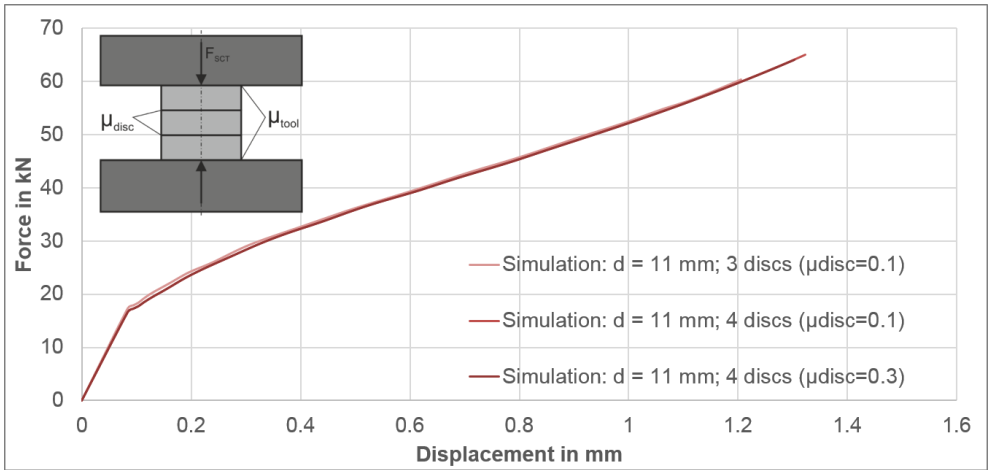


Figure 105: Comparison of simulated force-displacement curves of the SCT with varied conditions for disc to disc friction

In Figure 105, the coefficient of friction between the discs and the number of discs is numerically varied. No significant influence of the friction between the circular discs can be observed.

Figure 106 compares different disc diameters and coefficients of friction between tool and discs.

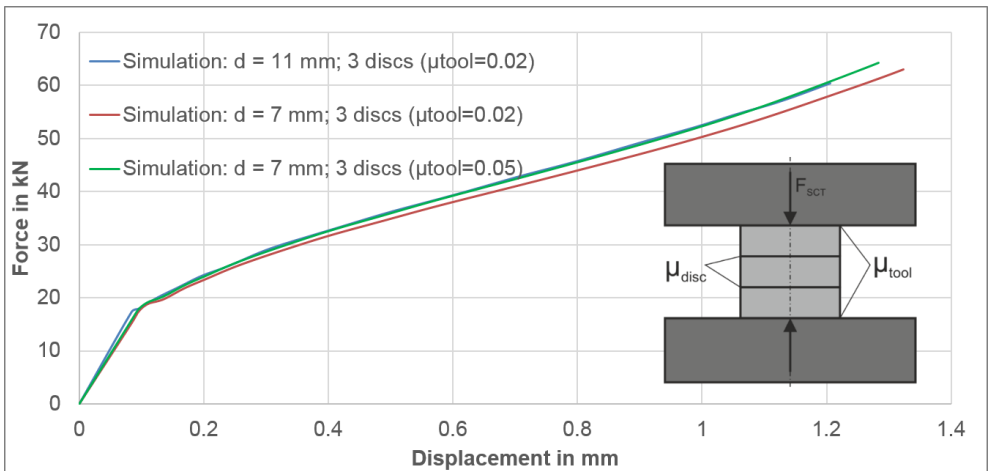


Figure 106: Comparison of simulated force-displacement curves of the SCT with varied conditions for tool to disc friction and varied disc diameters

It becomes apparent that the size of the contact surface (disc diameter) as well as the coefficient of friction have a significant influence on the force progression.

Overall it is assumed that the influence of friction at the SCT is assumed to be relatively small, but nevertheless the experimental values must be corrected for this. Since the influences of friction and hydrostatic pressure cannot be separated, it is not possible to determine the specific coefficients of friction without separate friction tests. For this reason, the values have been obtained from the literature. Following the friction correction according to Siebel with the listed coefficients of friction is used as shown in Figure 107.

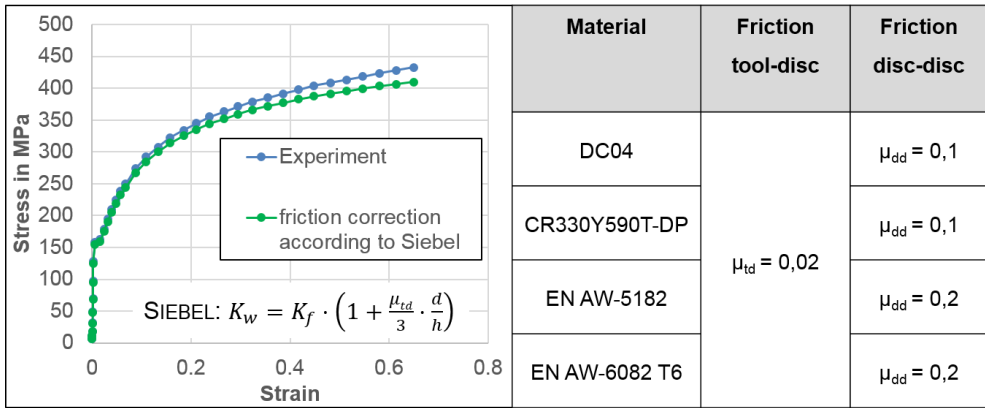


Figure 107: Friction correction of the flow curve from the SCT according to Siebel (left) and friction coefficients for the considered materials

### 10.4 Influence of diameter and number of discs

In the first step, a numerical study was carried out on the influence of the disc diameter and the number of discs on the triaxiality. The simulation model explained in 9.5.2 was used for this purpose.

Figure 108 shows the calculation results for the variation of the disc diameter with the same number of discs. It can be seen that the compressive stresses in the disc increase with increasing diameter. The average triaxiality decreases from  $\eta = -0.5$  with  $d_{sct} = 5$  mm to  $\eta = -0.8$  with  $d_{sct} = 15$  mm while the average omega does not change significantly.

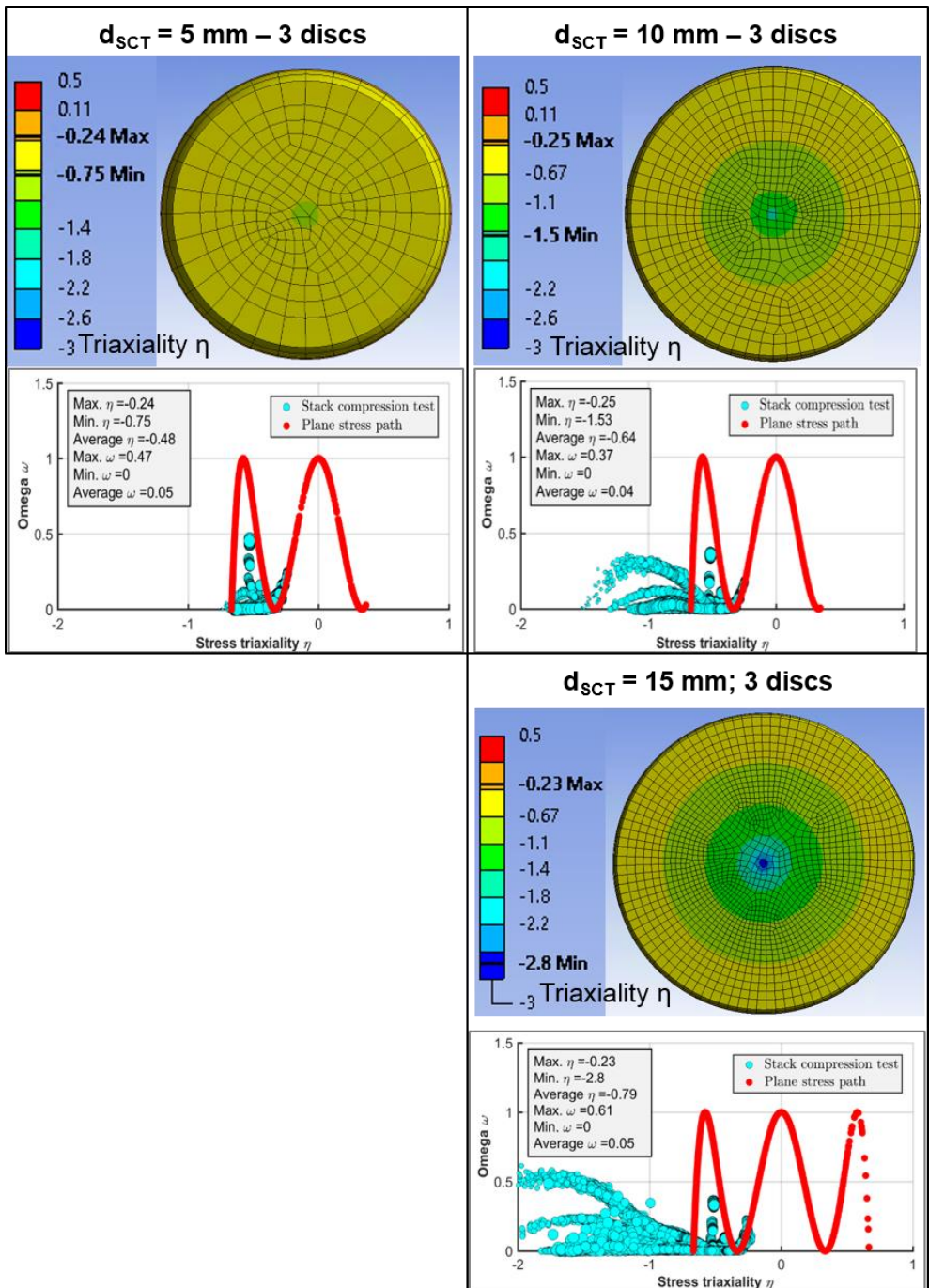


Figure 108: Influence of disc diameter on triaxiality and omega at the stack compression test of DC04 ( $h_1 = h_0/2$ )

Figure 109 summarizes the calculated average triaxialities for different disc diameters and numbers of discs. It can be seen that a larger disc diameter leads to a reduction in the triaxiality or to an increase in the compressive stress in the discs during the compression test. The use of a smaller number of discs has a comparable effect.

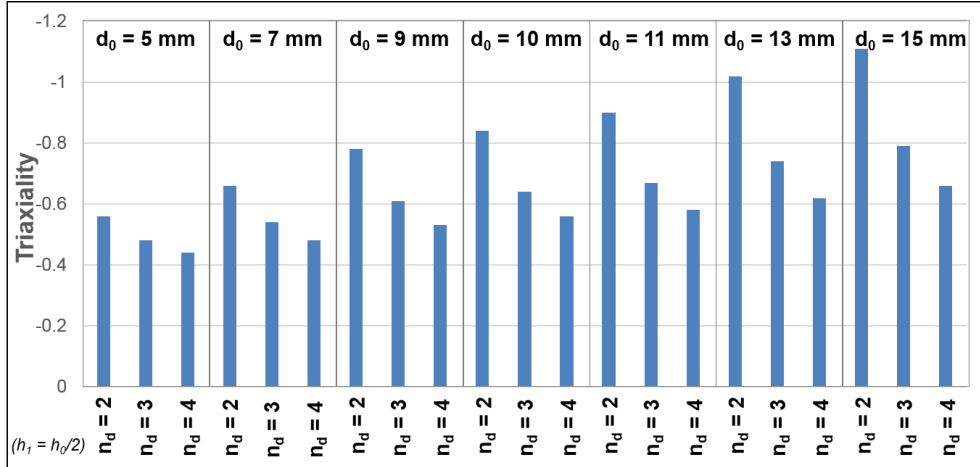


Figure 109: Influence of starting disc diameter ( $d_0$ ) and number of discs ( $n_d$ ) on calculated average triaxiality at the stack compression test

This numerical analysis shows that it is possible to reduce the triaxiality by adjusting the dimensions or number of discs in the SCT, to improve the comparability to the mechanical joining methods.

In the next step discs with different diameters were manufactured by eroding and SCT experiments were carried out. Figure 110 shows the resulting flow curves of this experiments for the CR330Y590T-DP. All flow curves were corrected for friction.

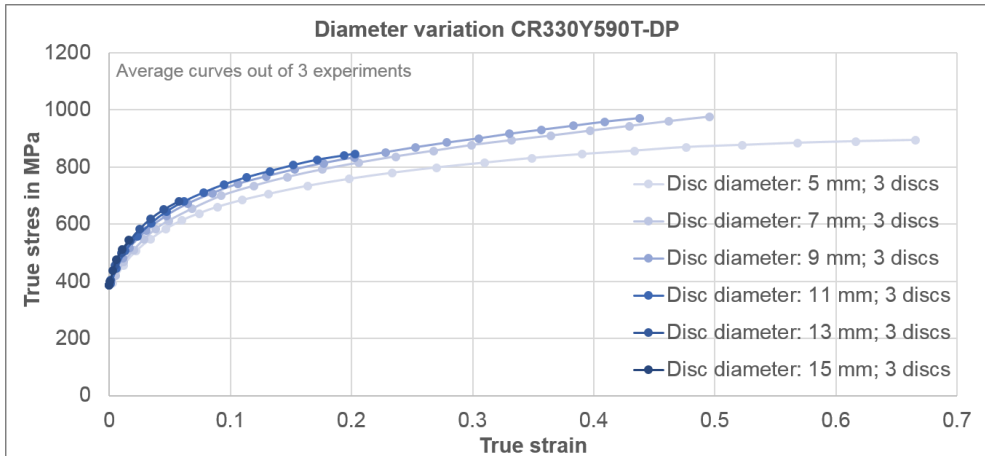


Figure 110: Flow curves for CR330Y590T-DP carried out by the SCT with varied disc diameters

For CR330Y590T-DP, the experimental results in Figure 110 correspond quite well with the simulation results in Figure 108 and Figure 109. Increasing diameter of the discs leads to

increasing true stress of the flow curves. The lower strain during the tests with the larger discs only results from the limited upsetting force of the press used of 100 kN.

Also for the compression tests of the CR330Y590T-DP where the number of discs was varied (Figure 111), the trend is confirmed by the results of the simulations.

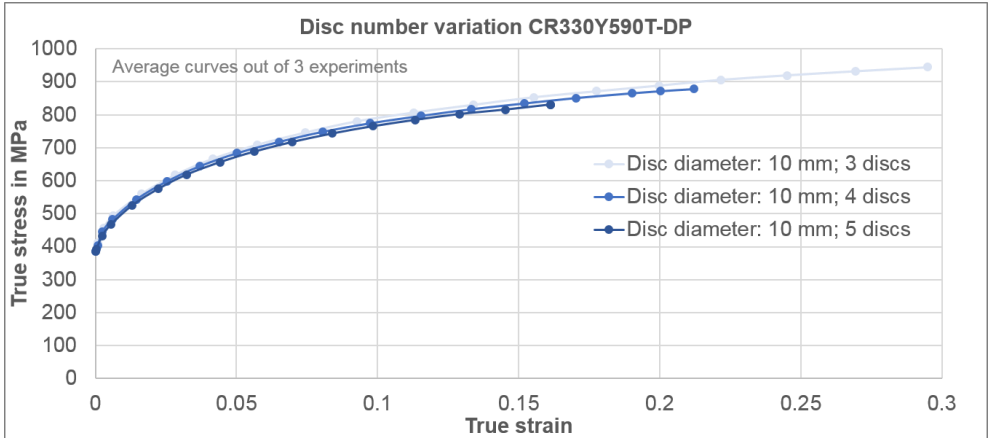


Figure 111: Flow curves for CR330Y590T-DP carried out by the SCT with varied number of discs

Also for the DC04 material the trend of increasing true stress with increasing diameter of the discs can be seen (Figure 112), albeit the influence is less than observed for CR330Y590T-DP.

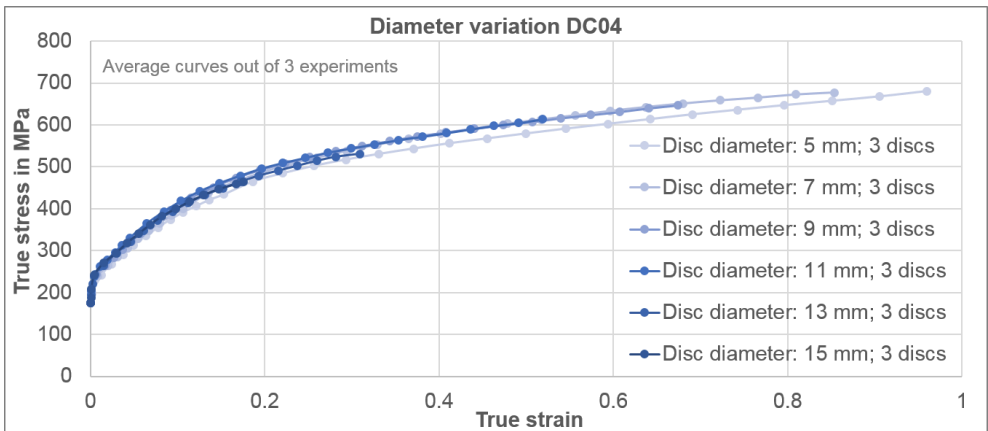


Figure 112: Flow curves for DC04 carried out by the SCT with varied discs diameters

However, the upsetting experiments also confirm that the influence of triaxiality on the yield stress is differently developed for different materials. This is shown, for example, by the experiments with EN AW-5182, in which no trend towards an increase in the flow stress with increasing disc diameter can be seen.

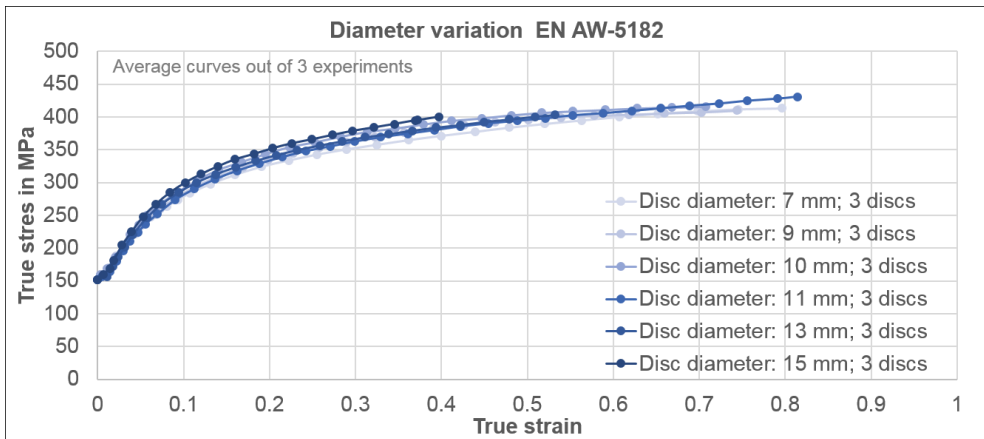


Figure 113: Flow curves for DC04 carried out by the SCT with varied discs diameters

A further evaluation criterion in the compression test is the scattering of the values over a test series. This was also investigated in the variation of the disc diameter and the number of discs. A comparison of the results for DC04 and EN AW-5182 is shown in Table 11. The table shows that the scatter of the flow stress over the test series decreases with an increase in the diameter of the disc or a more robust compression test is possible for both materials. The decrease of the maximum elongation is due to the maximum press force of 100 kN and could be comparable to higher press forces. However, this is of course also associated with higher costs for the equipment and the test set-up manufacturing.

Table 11: Comparison of scattering at SCT with different disc diameter and number of discs for DC04 and EN AW-5182

SCT parameter			DC04		EN AW-5182	
Number of discs ( $n_d$ )	Disc diameter $d_o$ in mm	$h_o/d_o$ -ratio	Max. strain	Scattering of the flow stress in % ( $n = 3$ )	Max. strain	Scatter of the flow stress in % ( $n = 3$ )
2	5	0.40	0.76	± 2.36 %	1.03	± 1.11 %
3	5	0.60	1.09	± 3.21 %		
5	5	1.00	0.60	± 3.85 %	0.54	± 1.27 %
1	7	0.14	0.29	± 0.14 %	0.86	± 0.94 %
2	7	0.29	0.71	± 1.00 %	1.06	± 4.66 %
3	7	0.43	0.86	± 1.00 %	0.93	± 1.95 %
4	7	0.57	0.87	± 3.08 %	0.65	± 0.10 %
5	7	0.71	0.83	± 1.09 %	0.65	± 2.66 %
1	9	0.11			0.58	± 0.18 %
2	9	0.22			0.91	± 0.70 %
3	9	0.33	0.84	± 6.35 %	0.79	± 4.35 %
4	9	0.44	0.70	± 1.08 %	0.76	± 3.56 %
5	9	0.56	0.72	± 2.93 %	0.58	± 2.14 %
3	10	0.30	0.60	± 1.26 %	0.71	± 0.62 %
4	10	0.40	0.63	± 1.40 %	0.54	± 1.66 %
5	10	0.50	0.53	± 1.43 %	0.42	± 1.94 %
1	11	0.09			0.72	± 2.18 %
2	11	0.18			0.65	± 0.11 %
3	11	0.27	0.55	± 0.78 %	0.82	± 0.40 %
4	11	0.36	0.55	± 0.69 %	0.63	± 0.21 %
5	11	0.45	0.70	± 0.31 %	0.50	± 0.07 %
3	13	0.23	0.32	± 0.50 %	0.53	± 0.62 %
4	13	0.31	0.32	± 0.72 %	0.42	± 0.16 %
5	13	0.38	0.31	± 0.12 %	0.34	± 1.07 %
3	15	0.20	0.18	± 0.11 %	0.40	± 0.57 %
4	15	0.27	0.19	± 0.14 %	0.36	± 0.64 %
5	15	0.33	0.19	± 0.13 %	0.29	± 0.44 %

Based on the results of the compression tests in Table 11, the question arises how high the maximum strain should be for a relatively secure flow curve approximation. Therefore, in Figure 114 the maximum strain of the experimental values as a basis for extrapolation according to Hockett-Sherby is varied and the influence on the total flow curve is shown.

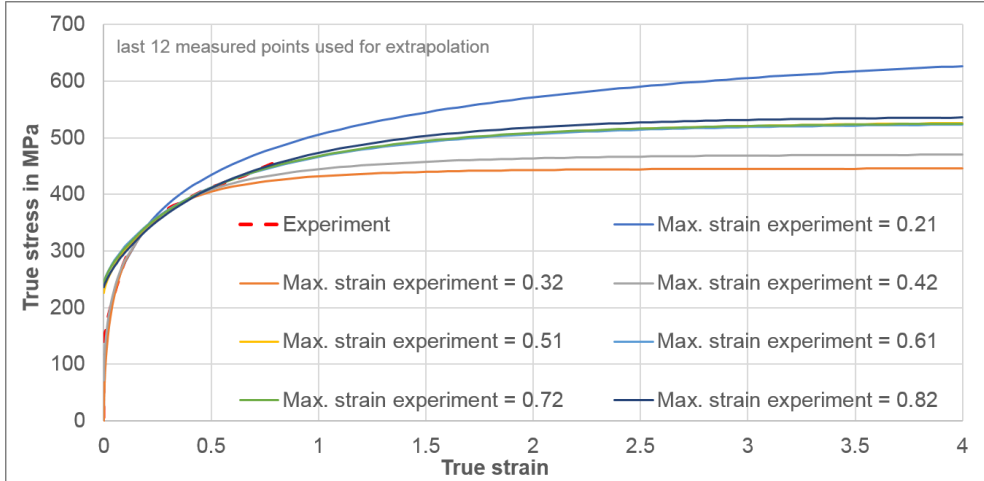


Figure 114: Influence of max. strain from the experiment on the Hockett-Sherby extrapolation

It can be noted that the extrapolated values vary significantly less when the experimental basis is values with strain above 0.5. The latter observation is in agreement with the conclusions drawn in section 7.4.

## 10.5 Influence of a shift in hydrostatic pressure

In Section 10.4 it is shown that for CR330Y590T-DP the SCT-flow curve depends on the magnitude of the triaxiality, see Figure 110. Variation of the triaxiality is achieved by changing the disc diameter. These results suggest a dependency of the flow stress in the hydrostatic stress. To further elaborate on this hypothesis, the focus is on the stack compression test (SCT) and the hydraulic bulge test (HBT). Both tests enable the determination of the large strain flow curve of sheet metal under an identical deformation mode. In terms of stress state, assuming that:

- plastic yielding is independent from the hydrostatic pressure, and
- friction in the SCT can be sufficiently reduced,

then the SCT is equivalent to the HBT, i.e. in-plane balanced biaxial tension. The SCT, also referred to as through-thickness compression test [STE14], layer compression test [MER09] or multi-layer upsetting test [CO12], enables to suppress plastic instabilities hence enabling to probe large plastic strains. The stack can consist of small circular discs or square specimens. A clear benefit in this regard is that the SCT requires only a small amount of test material, which can be locally removed to acquire the local flow behaviour. Friction between the stack and the compression tools is inevitable. A friction-hill analysis [AN05] shows that a small height to diameter (or width for bricks) ratio, referred to as aspect ratio in the remainder of this work, requires a correction for friction to obtain an accurate flow curve. The latter implies that the friction coefficient can be measured, and, more importantly, is constant during the SCT.

Indeed, friction conditions might vary as lubrication deteriorates due to thinning of the film and extension of the surface. With the aid of the ring compression test, An and Vegter [AN05] showed that oiled PTFE film yields a constant frictional behaviour. Coppieters [CO12] adopted the modified two specimen method [HAN02] to calibrate the coefficient of friction in the SCT of low carbon steel. Steglich et al. [STE14] and Merklein and Godel [MER09] did not correct for friction when subjecting magnesium alloys and steel sheets to the SCT, respectively. Despite this inconsistency with respect to the role of friction in the SCT, it is clear that the aspect ratio plays a crucial role in assessing the need for friction correction [AN05]. The lower the aspect ratio of the stack, the more pronounced the frictional effect and the need for friction correction. However, when targeting the large strain flow curve, a small aspect ratio is favoured for the stability of the stack deformation and mitigating preliminary stack defects such as disc localization. Moreover, frictional effects lead to a triaxial stress state which further complicates the determination of the flow curve. Obviously, friction is a disadvantage of the SCT. The crux of the problem is that one must be able to guarantee a strain range for which a constant frictional conditional friction prevails. In addition, correction of the flow curve requires a method to quantify the frictional condition. When a shearable film (e.g. TPE) is used, a correction can be made based on the shear strength of the film [AN05]. As opposed to the SCT, the HBT does not suffer from frictional effects but in turn lacks accuracy due to assumptions involved in the analytical treatment of the experimental data [MUL15a].

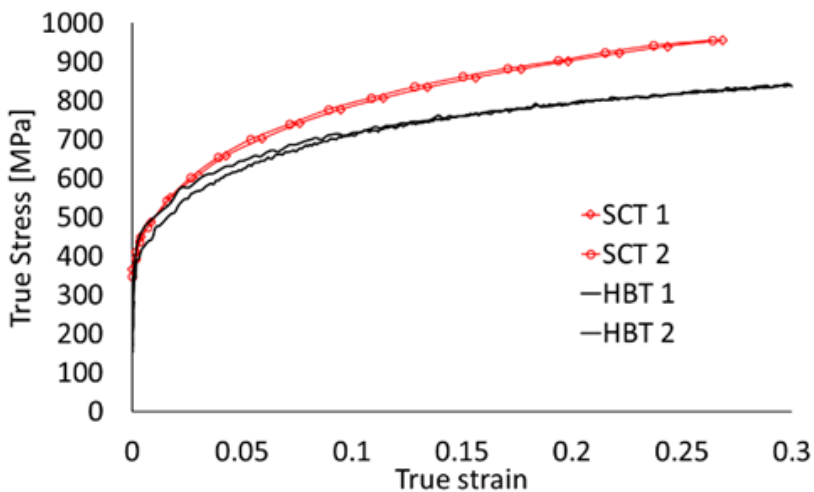


Figure 115: Flow curves obtained through SCT and HBT. Material: CR330Y590T-DP

In addition, it is well-known that the HBT is not accurate in determining the flow curve at moderately low plastic strains due to the uncertainty related to measuring the curvature of the dome apex. Given the identical deformation mode and stress condition, one would expect identical flow behaviour obtained through the SCT and HBT. Merklein and Godel [MER09] found a good agreement between the SCT and HBT for DC04 and DX56 steel sheet. Mulder et al. [MUL15] initially found a discrepancy between the SCT and the HBT for DC06. According to Mulder et al. [MUL15], the latter discrepancy could be attributed to strain rate and temperature effects in the HBT. Steglich et al. [STE14] found an excellent agreement between the SCT and HBT for magnesium alloys. The aim of this section is to further elaborate on the discrepancy between the SCT and the HBT found for CR330Y590T-DP steel sheet. The next section discusses the experimentally acquired flow behavior of CR330Y590T-DP determined

using the SCT and the HBT. To probe large plastic strains with the SCT, a low aspect ratio is chosen along with a strategy to correct for friction. Based on the work by Spitzig et al. [SPI84] and Spitzig and Richmond [SPI75], we embark on theoretical considerations regarding the role of the hydrostatic pressure shift on the flow stress. The latter findings are experimentally are then validated using the experimentally acquired flow behaviour.

### 10.5.1 Experimental

The SCT is conducted on an electro-mechanical press with a load capacity of 100 kN. The stack consisted of 3 discs with a diameter of 10 mm. Lubrication (oil) is applied to minimize the effect of friction. The red curves shown in Figure 115 are the experimentally acquired flow curves using the SCT calculated following:

$$\sigma_{avg}^c = \frac{F \cdot h}{\pi \cdot r_0^2 \cdot h_0}$$

where  $\sigma_{avg}^c$  is the average compressive true stress,  $F$  the measured force and  $h_0$ ,  $r_0$  the initial stack height and radius, respectively. The logarithmic true compressive strain is simply:

$$\varepsilon = \ln\left(\frac{h_0}{h}\right)$$

It can be inferred that the SCT yields a good repeatability up to a true plastic strain of 0.3. Beyond that point, lubricant depletion led to metallic contact and galling is observed. Figure 115 also shows the flow behaviour measured by the HBT. The HBT-flow stress is calculated as follows:

$$\sigma = \frac{\rho \cdot p}{2 \cdot t}$$

where  $\sigma$  and  $p$  are the true stress and fluid pressure, respectively. The logarithmic true strain is estimated as:

$$\varepsilon = -\varepsilon_1 - \varepsilon_2$$

which is valid assuming equal strain or equal stress at the specimen pole. The radius of curvature  $\rho$  and the principal strains  $\varepsilon_1, \varepsilon_2$  at the top of the bulged specimen are measured using a stereo DIC system. In this regard, ISO 16808 is followed and extended with a closed-loop strain rate control at the top of the dome. The average strain rates in the HBT and the SCT are both approximately  $10^{-4} \frac{1}{s}$ . It can be inferred from Figure 115 that the repeatability of the HBT beyond a true strain of 0.1 is excellent.

Given the low aspect ratio of the stack, it is required to compensate for friction. The friction-hill analysis of a homogenous compression of a single disc [DIE87] leads to:

$$\sigma = \frac{2 \cdot \sigma_{avg}^c}{\left(\frac{h}{\mu r}\right)^2 \cdot \left[e^{\frac{2\mu r}{h}} - \frac{2\mu r}{h} - 1\right]} \quad (5)$$

with  $h$ ,  $r$  the instantaneous height and radius of the stack, respectively. The height  $h$  of the stack is measured and  $r$  is derived assuming volume constancy. Eq.(5) is validated for the stack configuration (i.e. number of discs and diameter) adopted in this study using a FE model of the SCT. This means that Eq.(5) can be adopted to correct the SCT-flow curve shown in Figure 115 provided that the friction coefficient  $\mu$  is known. The modified two specimen method (MTSM) [HAN02] could be adopted to identify  $\mu$ . The fundamental hypothesis of the MTSM, however, is that the material behavior is independent of the stack configuration. Given that the hydrostatic stress component in the stack potentially depends on the stack configuration, the MTSM is not applied. Instead, the coefficient of friction is inversely calibrated using an FE model of the SCT. To this end, the SCT is simulated using a displacement-driven FE model assuming a constant friction coefficient and adopting the HBT-flow curve which is considered here as the ground-truth strain hardening. The left panel of Figure 116 shows the experimental cross section of the stack after compression, while the right panel shows the numerical simulation. A frictionless SCT would lead to a perfectly homogeneous experiment, instead some slight barreling can be observed in the left panel.

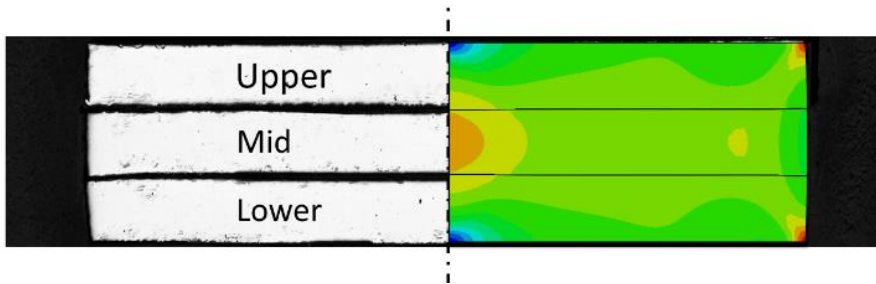


Figure 116: Cross-section compressed stack CR330Y590T-DP. Left: experimental. Right panel: FE simulation using HBT-flow curve and  $\mu=0.05$

Instead of assessing the homogeneity of the SCT by evaluating this barreling, one could also evaluate the thickness of each individual disc. Indeed, a frictionless experiment would lead to an identical thickness reduction of each disc in the stack. The red symbols in Figure 117 show the experimentally measured (average of 3 experiments) disc thicknesses at the center of each disc. It can be inferred that the mid disc is consistently thinner than the discs that are in contact with the compression platens. This observation is used to inversely tune the friction coefficient using the FE model. Figure 117 shows the numerically predicted thicknesses using three friction coefficients, namely  $\mu=0.1$ ,  $0.05$  and  $0.03$ . It can be seen that a friction coefficient of  $\mu=0.05$  enables to accurately reproduce the thickness individual disc. Indeed, a frictionless experiment would lead to an identical thickness reduction of each disc in the stack.

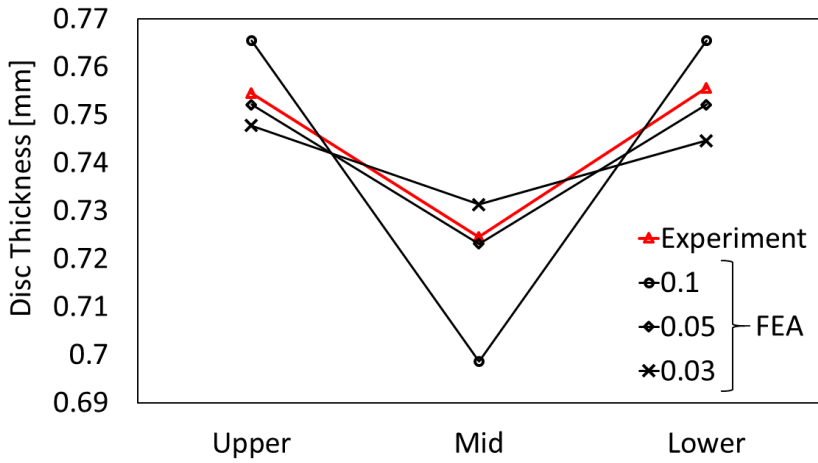


Figure 117: Thickness after compression measured at the centre of each individual disc. Material: CR330Y590T-DP

It must be noted that this is in line with the findings of Coppieters [COP12] using the MTSM. Figure 118 shows the SCT-flow curve corrected for friction using Eq.(5) with a constant friction coefficient of  $\mu=0.05$ . It can be seen that the corrected SCT-flow curve is bound between the raw SCT-flow curve and the lower bound HBT-flow curve.

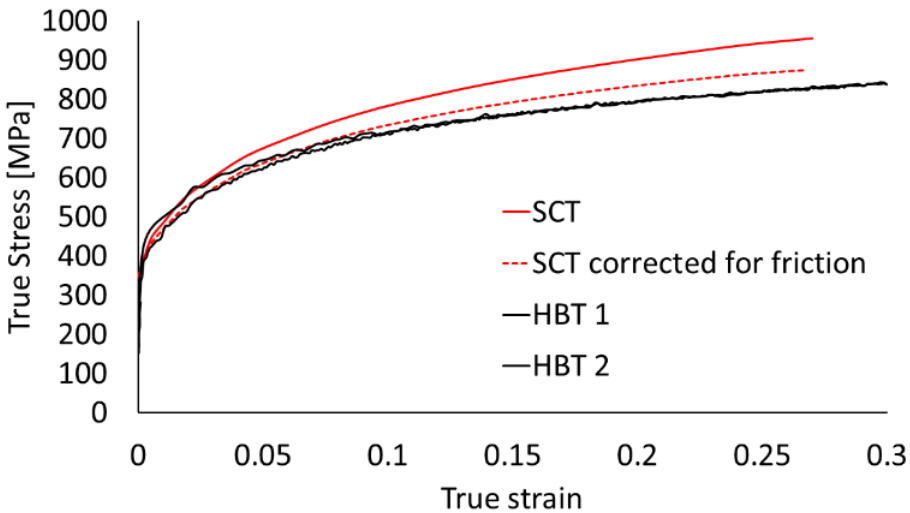


Figure 118: Flow curves obtained through SCT (with and without correction for friction) and HBT. Material: CR330Y590T-DP

### 10.5.2 Theoretical

Given that the HBT-flow curve lacks accuracy in the strain range  $0 \leq \varepsilon \leq 0.15$ , the focus here will be on the discrepancy of the flow behavior in the strain range  $0.15 \leq \varepsilon \leq 0.3$ . Note that this analysis is inherently assuming a correct compensation for friction in the SCT. In this section, we draw on the work of Spitzig et al. [SPI84, SPI75] regarding the effect of superimposed hydrostatic pressure on the tension and compression flow stress behavior of steels. They concluded that the hydrostatic pressure increases the yield strength and work hardening rate of steels. Richmond and Spitzig [SPI75] used a yield condition enabling to describe their experimental observations, namely:

$$I_2 = c - aI_1$$

where  $I_2$  is the von Mises effective stress and  $I_1$  the first stress tensor invariant. When the parameters  $a$  and  $c$  are constants, this yield condition is identical to that proposed by Drucker and Prager [DRU52]. However, Spitzig and Richmond [SPI75] revealed that  $a$  and  $c$  are strain dependent coefficients that can be determined from experiments. Additionally, they showed that the pressure coefficient  $\alpha$ , which reads as:

$$\alpha = \frac{a}{c}$$

is nearly constant and within the range of  $13 \leq \alpha \leq 23$  (TPa<sup>-1</sup>) for a number (about 10) of low and high strength steels. Since the yield condition enables the capture of the well-known strength differential effect (SDE), i.e. the difference between the flow stress under uniaxial tension and compression, this supports the idea that the SDE is driven by the interaction of pressure and the transient dilatancy of moving dislocations as demonstrated by Bulatov et al. [BUL99]. Given that the yield condition depends on the first stress tensor invariant, however, it is used here to understand the discrepancy in flow behavior between the SCT and the HBT. The stress states associated with the SCT and the HBT are  $\boldsymbol{\sigma}^{SCT}$  and  $\boldsymbol{\sigma}^{HBT}$ , respectively. Without a superimposed external pressure, the yield condition can be applied to a material that is subjected to the stress states  $\boldsymbol{\sigma}^{SCT}$  and  $\boldsymbol{\sigma}^{HBT}$ , respectively:

$$I_2(\boldsymbol{\sigma}^{SCT}) = c - aI_1(\boldsymbol{\sigma}^{SCT})$$

$$I_2(\boldsymbol{\sigma}^{HBT}) = c - aI_1(\boldsymbol{\sigma}^{HBT})$$

Subtracting both equations, yields:

$$I_2(\boldsymbol{\sigma}^{SCT}) - I_2(\boldsymbol{\sigma}^{HBT}) = -aI_1(\boldsymbol{\sigma}^{SCT}) + aI_1(\boldsymbol{\sigma}^{HBT})$$

Note that this approach with the von Mises effective stress  $I_2$  can be extended to any pressure independent effective stress  $\bar{\sigma}$ . The mean or hydrostatic stress  $\sigma_m$  is one third of the first stress tensor invariant yielding:

$$\bar{\sigma}(\boldsymbol{\sigma}^{SCT}) - \bar{\sigma}(\boldsymbol{\sigma}^{HBT}) = +3a [\sigma_m^{HBT} - \sigma_m^{SCT}]$$

The latter equation shows that the difference in the two effective stresses is proportional to the pressure shift between the two stress states  $\boldsymbol{\sigma}^{SCT}$  and  $\boldsymbol{\sigma}^{HBT}$ . Moreover, it shows that the difference in effective stress between the SCT and the HBT can be used to calibrate the parameter  $a$  of the yield condition:

$$a = \frac{\bar{\sigma}(\sigma^{SCT}) - \bar{\sigma}(\sigma^{HBT})}{3 \cdot [\sigma_m^{HBT} - \sigma_m^{SCT}]}$$

By substituting the mean stresses:

$$a = \frac{\bar{\sigma}(\sigma^{SCT}) - \bar{\sigma}(\sigma^{HBT})}{2\sigma^t + \sigma^c}$$

as  $\sigma^t = \bar{\sigma}(\sigma^{HBT})$  for an isotropic material with  $\sigma^t$  the uniaxial tensile stress. Given that for steels, half of the strength-differential effect can be written as [RIC80]:

$$\frac{\sigma^c - \sigma^t}{\sigma^c + \sigma^t} = a \ll 1$$

, the following relation between  $a$  and the difference in flow behaviour can be derived:

$$a = \frac{\bar{\sigma}(\sigma^{SCT}) - \bar{\sigma}(\sigma^{HBT})}{3 \cdot \bar{\sigma}(\sigma^{HBT})}$$

In other words, the flow curves measured with the aid of the SCT and the HBT can be exploited to identify the parameter  $a$  in the yield condition. It must be noted the expression for  $a$  must be evaluated at an instant when the same amount of plastic work per unit volume is consumed. Finally, the coefficient  $c$  can be calculated as:

$$c = \bar{\sigma}(\sigma^{HBT}) \cdot (1 + 2 \cdot a)$$

The difference in flow behavior shown in Figure 118 is used to calculate  $a$  and  $c$  in the strain range  $0.15 \leq \varepsilon \leq 0.3$ . In addition, the values of  $a$  and  $c$  can be used to calculate the pressure coefficient  $\alpha$ . For CR330Y590T-DP, it can be inferred from the figure below that  $\alpha$  is nearly constant (average  $\alpha = 20.5 \text{ TPa}^{-1}$ ) and within the range of  $13 \leq \alpha \leq 23 \text{ (TPa}^{-1})$ . The fact that  $\alpha$  is not perfectly constant might be due the assumed constant frictional condition, an assumption which is potentially violated as lubrication depletes as the deformation increases. Although friction probably introduces some uncertainty here, it seems that the current findings are consistent with the work of Spitzig and Richmond [SPI75] on high strength steels.

As opposed to the findings obtained through exploiting the difference in flow behavior between the SCT and the HBT, in-plane tension-compression experiments enable to accurately determine the pressure coefficient  $\alpha$  for sheet metal in the lower strain range, e.g.  $0 \leq \varepsilon \leq 0.1$ . Recently, Maeda et al. [MAE18] correlated the SDE effect with the pressure dependent yield condition for DP980 sheet. They calibrated the coefficients  $a$  and  $c$  for DP980 steel sheet using in-plane tension-compression experiments and found a pressure coefficient  $\alpha$  of  $24 \text{ TPa}^{-1}$  associated with a true plastic strain of  $\varepsilon = 0.08$ . Shirakami et al. [SHI17] measured the SDE effect of DP590 steel sheet and found that the compressive flow stress is higher than in tension by approximately 6% in the strain range  $0 \leq \varepsilon \leq 0.05$ . In this regard, shows that in the strain range  $0.15 \leq \varepsilon \leq 0.3$ , the SCT-flow stress of CR330Y590T-DP steel is consistently higher than the HBT-flow stress by approximately 6%. As such, the work of Maeda et al.

[MAE18] and Shirakami et al. [SHI17] for moderately small plastic strains seems to be in agreement with the findings here for larger plastic strain up to 0.3.

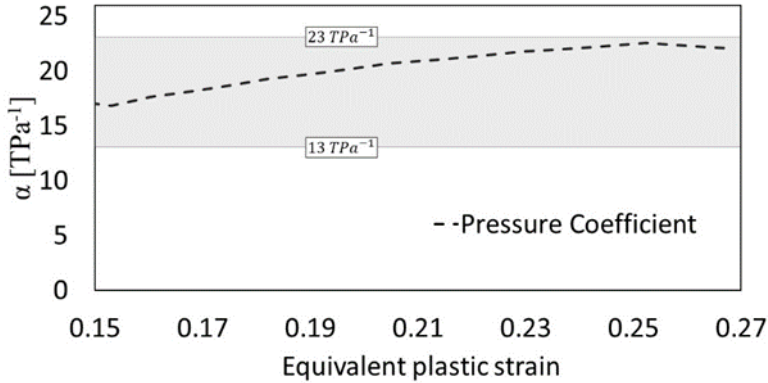


Figure 119: Pressure dependency as a function of the plastic equivalent strain (CR330Y590T-DP)

## 10.6 Round Robin test

In this section the aim is to subject the stack compression test to a Round Robin test. To this end, CR330Y590-DP was used. The batch of discs (diameter 10 mm) were produced by KUL using eroding. Each stack comprises 3 discs. Both labs subjected the stacks according to their internal test protocol under quasi-static conditions.

### 10.6.1 KUL experiments

Figure 120 shows the force-displacement curves of 6 SCT on CR330Y590-DP (3 discs, diameter 10 mm). It can be inferred that up to a stack reduction of 0.7 mm, the results show an excellent repeatability. Beyond that point (which corresponds to a load of approximately 100 kN) the results show significant scatter. The latter is caused by premature stack defects and lubricant depletion. Figure 121 shows the problem of disc localization: the plastic deformation localizes in a single disc leading to internal heterogeneous deformation of the stack. Figure 122 shows the problem of lubricant depletion. The KUL set up uses a mixture of tungsten disulphide and high-pressure grease. The lubricant is progressively dispersed, and, as deformation increases, leads to metallic contact and galling. Both effects limit the validity of the experiments on CR330Y590-DP to the green box shown in Figure 5. The associated true plastic strain is about 0.3. In order to mitigate this, interrupted SCT experiments were conducted enabling to replace the lubricant after a certain amount of stack reduction. Figure 124 shows the load-displacement curves obtained through interrupted testing. The SCT was interrupted 4 times to replace the lubricant. It can be inferred that interrupted testing yields and excellent repeatability. However, it comes with a large experimental effort. The cross section of the stack after interrupted testing is shown in Figure 123. It can be seen that the stack is not subjected to a perfectly homogeneous deformation. For this reason, and the fact that the maximum load capacity of the IWU set up is 100kN, we limit the analysis here to the green region shown in Figure 107.

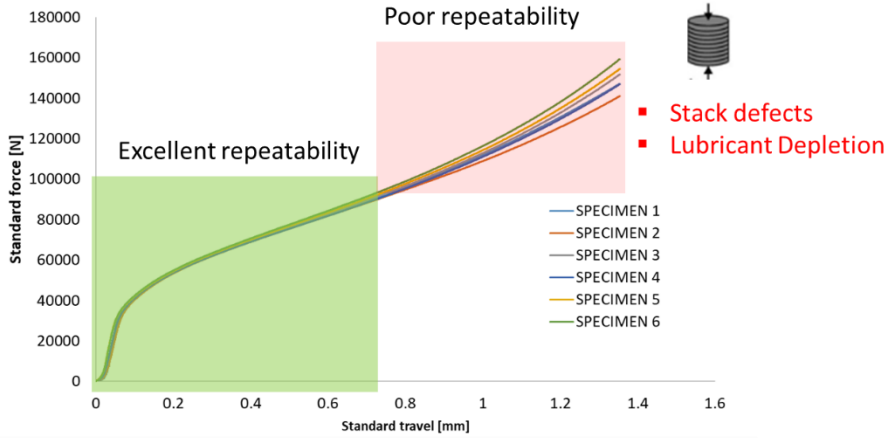


Figure 120: Force –displacement curves stack compression test for CR330Y590-DP (3 discs, diameter 10 mm)

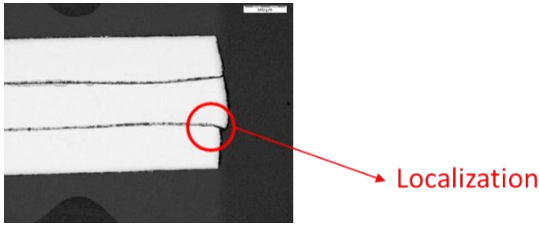


Figure 121: Disc localization CR330Y590-DP (3 discs, diameter 10 mm)

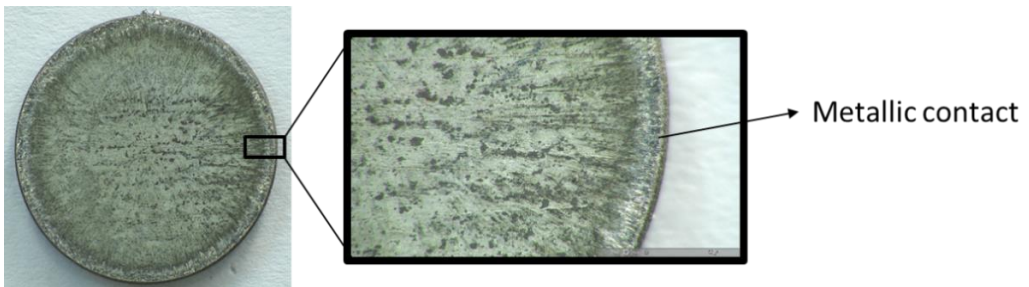


Figure 122: Lubricant Depletion CR330Y590-DP (3 discs, diameter 10 mm)

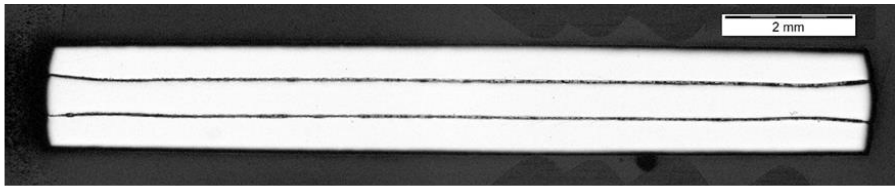


Figure 123: Cross section CR330Y590-DP (3 discs, diameter 10 mm) after interrupted SCT

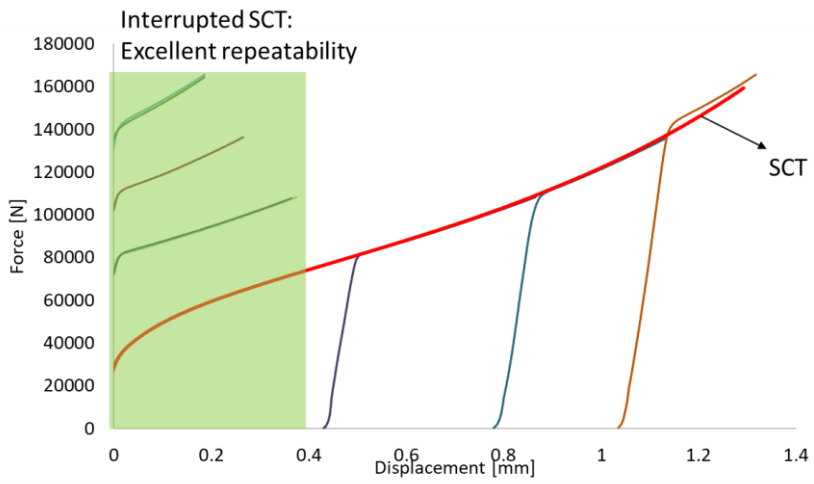


Figure 124: Interrupted SCT CR330Y590-DP (3 discs, diameter 10 mm)

### 10.6.2 Comparison of IWU and KUL experiments

Figure 125 shows the flow curves obtained by IWU. The figure shows the results of 6 experiments with an excellent repeatability. 3 experiments were conducted with the lubricant used by IWU (LUB\_IWU) and 3 experiments were conducted with the lubricant used by KUL (LUB\_KUL). It can be inferred that in the targeted strain range, the influence of the adopted lubricant can be safely ignored.

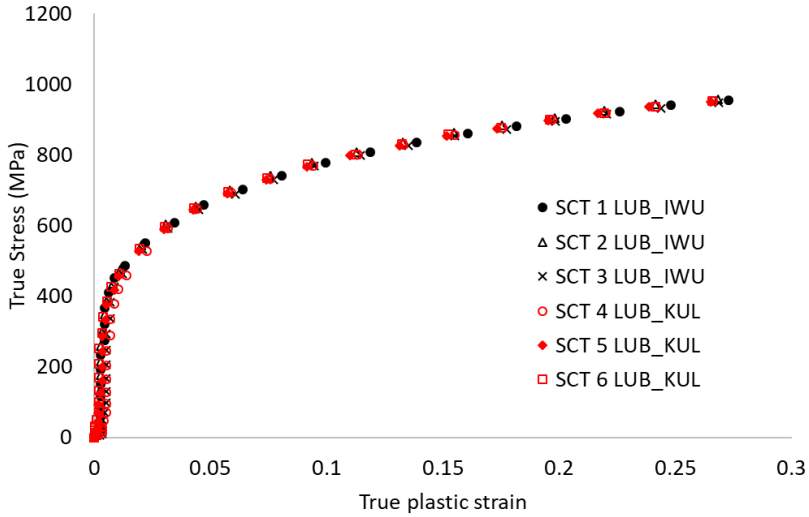


Figure 125: Influence of the lubricant CR330Y590-DP (3 discs, diameter 10 mm)

## 11 Evaluation of flow curves from considered material tests

### 11.1 Flow curve extrapolation

None of the material tests enables to probe plastic strains in the order of 3. However, the numerical simulation needs to be fed with strain hardening data in this strain range. The only possibility is to extrapolate the experimentally acquired data using a hardening law. The idea here is very simple: the adopted hardening law is fitted to the available experimental data using a cost function that reads as:

$$C(q) = \frac{1}{N} \sum_{i=1}^N \left( 1 - \frac{f(\varepsilon_{eq}^{pl, EXP}, q)}{\sigma_{eq}^{EXP, i}} \right)^2$$

With  $f$  the chosen hardening law,  $q$  the number of model parameters,  $N$  the number of experimentally acquired data points,  $\sigma_{eq}^{EXP}$  and  $\varepsilon_{eq}^{pl, EXP}$  the experimentally determined true stress and true plastic strain, respectively. It is well-known that commonly used hardening laws cannot accurately describe both the pre-necking and the post-necking strain hardening. Therefore, it is common practice to directly use the pre-necking data and enforce the hardening law to accurately describe the experimentally acquired data beyond the point of maximum uniform strain. Indeed, when using extrapolation it is deemed appropriate to accurately capture the strain hardening rate at the end of the available experimental data:

$$\theta = \frac{df}{d\varepsilon_{eq}^{pl}}$$

In other words, it is advised to use specific weighting in the fitting procedure. The adopted procedure in this work puts high weight to enable a good fit with respect to the strain hardening rate at the maximum strain that was probed in the experiment:

$$(\theta)_{\varepsilon_{eq, max}^{pl}} = \frac{df}{d\varepsilon_{eq}^{pl}}$$

Needless to say is that accuracy of the extrapolation increases with the maximum plastic strain probed in the experiment. Figure 126 shows an example of the procedure applied to DC04. The data used for fitting the hardening law is obtained through the SCT and is shown in Figure 126 as the black solid line. The strain hardening rate at the maximum plastic strain (about 0.7) is used in the fitting procedure. Different hardening laws are fitted and the results are shown in Figure 126. It can be inferred that up to a true plastic strain of 1 all hardening laws give a comparable result. Beyond that point, however, a clear distinction can be made power law and saturation type of hardening laws. Nevertheless, both the scatter within each family of hardening laws is limited. Therefore, we selected the Swift law and the Hockett-Sherby law as representative laws for power law and saturation type hardening laws in the remainder of this work.

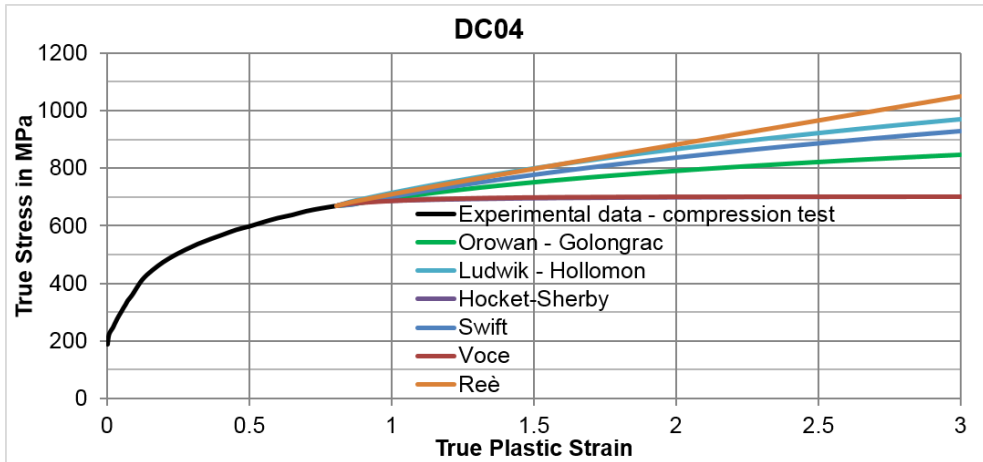


Figure 126: Extrapolation of SCT Data using commonly adopted hardening laws

## 11.2 Flow curve comparison

Figures 116-119 show the experimentally acquired (Upper panel) and extrapolated strain hardening behaviour for all materials. Assessing the experimentally acquired flow curves clearly shows that DC04 exhibits the largest deviation in flow curves. This is mainly due to the plastic anisotropy. The absolute stress level of the HBT-flow curve (not scaled here) is higher than the flow curve obtained through the tensile test. This difference can be expressed by the normalized yield stress, yielding a scalar  $k_b$  often used to convert the HBT-flow curve to the uniaxial tensile test:

$$k_b = \frac{\sigma_b}{\sigma_0}$$

With  $\sigma_b$  and  $\sigma_0$  the stresses associated with the HBT and the tensile test, respectively. This value as a function of the plastic equivalent strain. It can be inferred that initial yielding of DC04 is characterized by  $k_b \approx 1$ . As such, initial plastic yielding occurs isotropically. However, as plastic yielding continues,  $k_b$  increases quite rapidly suggesting deformation induced anisotropy. Indeed, the shape of the yield locus changes rapidly in the first 5 to 10 % plastic deformation for DC04. This is often referred to as differential work hardening, a well-known phenomenon exhibited by low carbon steels. It can also be seen that this effect seems to stabilize in the pre-necking region, for DC04 a stabilization of  $k_b \approx 1.2$  is observed. The latter explains the reason for the large discrepancy between the HBT and the other flow curves for DC04. For the other materials, the difference between the HBT and the uniaxial tensile test is relatively small. Indeed,  $k_b \approx 1$  for these materials. The value for EN AW 6082 T6 could not be determined as the HBT prematurely failed due to fracture in the draw bead.

Plastic anisotropy, however, is not responsible for the difference observed between the SCT and the HBT for CR330590-DP. The stack configuration used for the flow curves shown in Figures 2-5 consists of 3 discs with a diameter of 10 mm. The effect of pressure dependency was discussed in chapter 10 and applies for steels. It must be noted that the HBT flow curve for EN AW 5182 lies below the SCT-flow curve. The effect of pressure dependency for aluminum alloys should be further investigated.

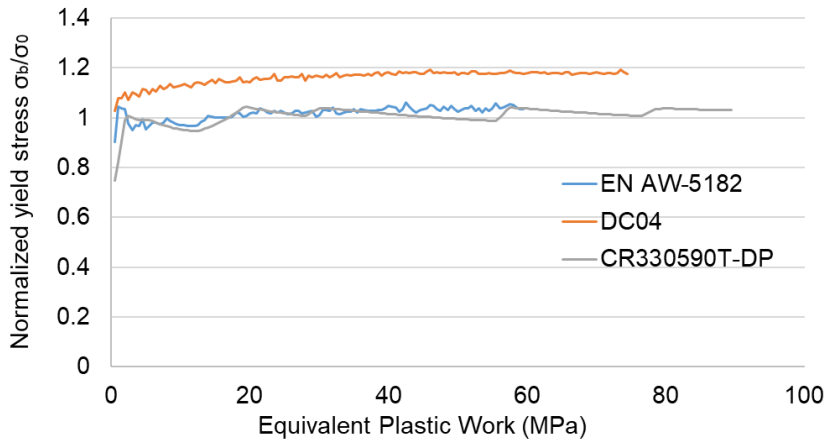


Figure 127: Normalized yield stress  $\sigma_b/\sigma_0$  as a function of the equivalent plastic work for EN AW-5182, DC04 and CR330590T-DP

In conclusion:

All material tests yield similar flow curves for plastically isotropic materials. This is also reflected in the extrapolation curves. If the material exhibits a large  $k_b$  value, deviation between the HBT and the other material tests can be expected. For steels, it is hypothesised that the difference between the SCT and the HBT is driven by the dependency of the flow stress on the hydrostatic pressure.

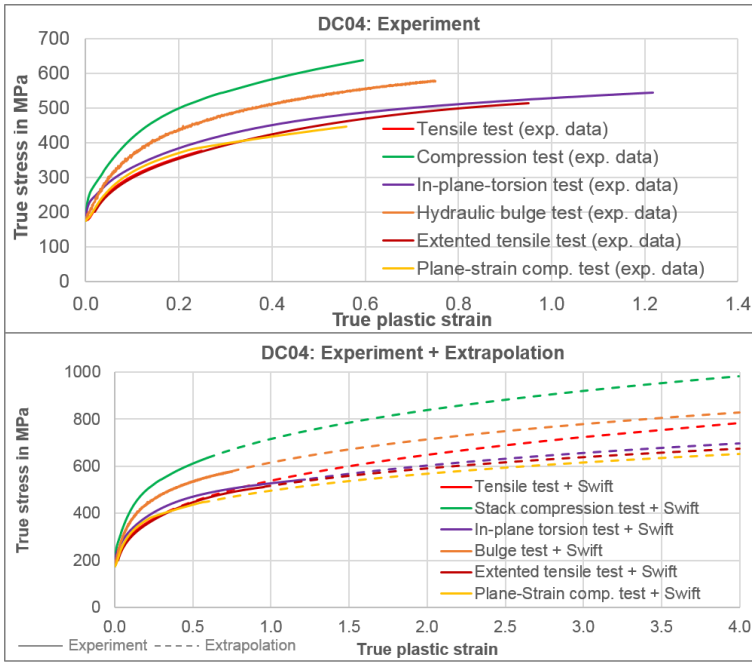


Figure 128: Flow curves from considered material tests for DC04

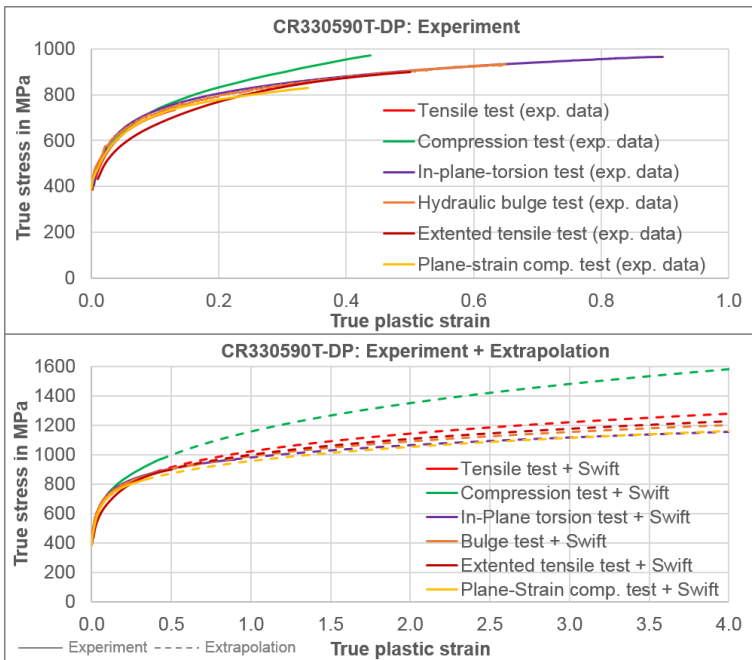


Figure 129: Flow curves from considered material tests for CR330Y590-DP

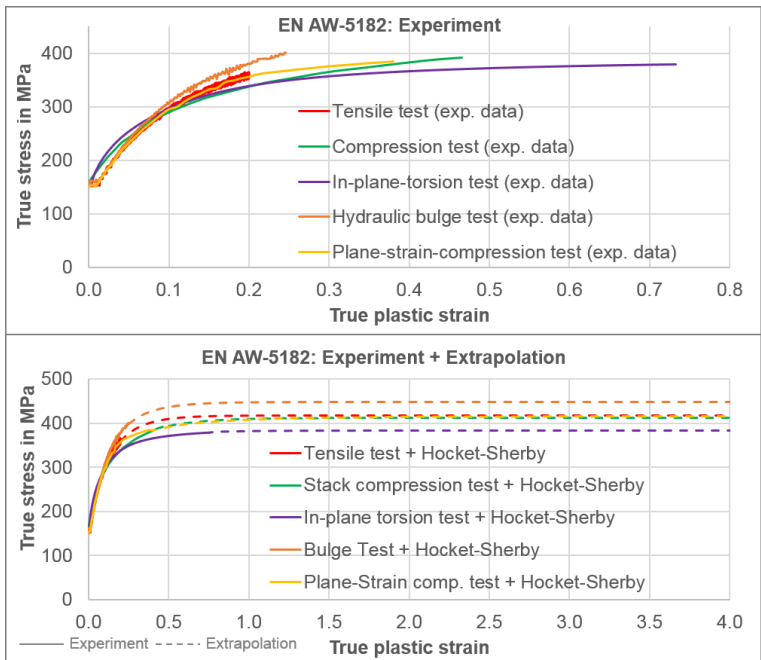


Figure 130: Flow curves from considered material tests for EN AW-5182

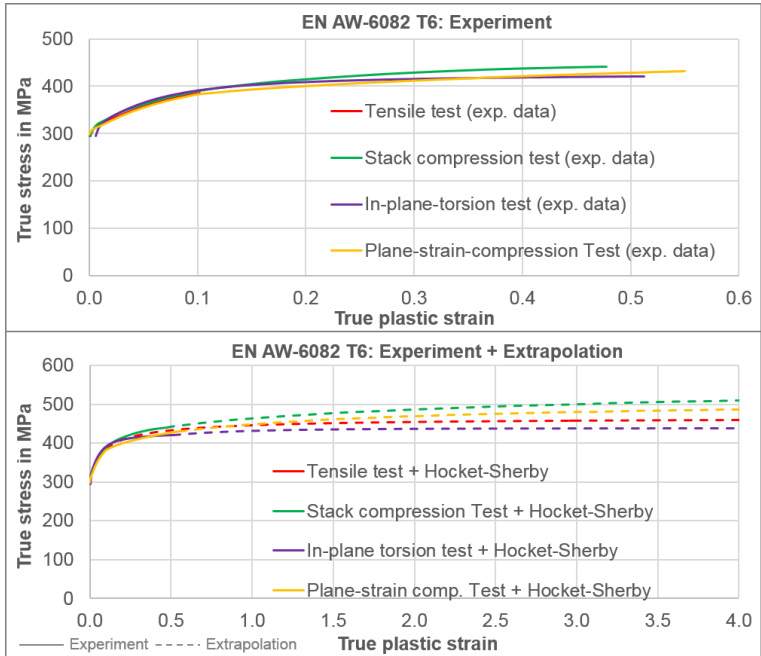


Figure 131: Flow curves from considered material tests for EN AW-6082 T6

## 12 Determination of flow curves for SPR-ST rivets

In the simulation of the SPR process, the flow curve of the rivets plays an elementary role in addition to friction conditions, mesh properties and flow curves of the sheets. The forming of the rivet takes place mainly in the rivet foot with degrees of deformation up to approx. 0.5 (Figure 132, left). With regard to triaxiality, both pressure and tension components occur (Figure 132, left).

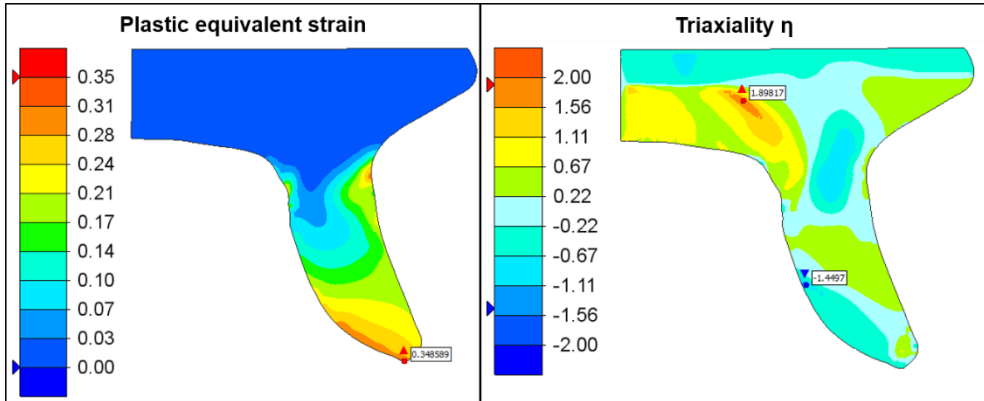


Figure 132: Plastic equivalent strain and triaxiality of the rivet at the end of the SPR process

SPR rivets are manufactured from a heat-treated steel according to DIN EN 10263-4 by forming and, depending on the desired rivet hardness and application, are subsequently heat-treated and coated.

Table 12: Hardness table for SPR rivets [DVS/EFB 3410]

Hardness class	Hardness in HV 10
H0	Supplier-specific
H1	280 ± 30
H2	410 ± 30
H3	450 ± 30
H4	480 ± 30
H5	500 ± 30
H6	555 ± 30
H7	575 ± 30

The rivets considered in the project described here have hardness class 4.

There are different approaches to the flow curve determination of the rivet. One variant is tensile or compression tests of the original bar material from which the rivets are manufactured. However, neither the history of the solid forming process nor the specific heat treatment of the rivet is taken into account. The second variant is to remove a ring from the rivet feet by means of erosion and then test it by means of an upsetting test. Following the tensile test of the base material is compared with the ring compression test of the rivet (Figure 133).

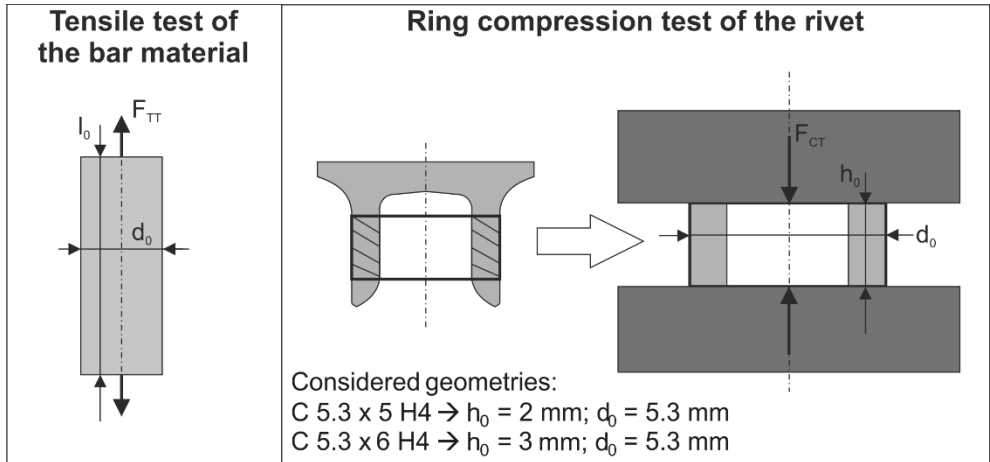


Figure 133: Characterization methods for rivet material

For the compression test, two different heights ( $h_0 = 2 / 3$  mm) of the rings are used for the tests, depending on the initial rivet length. In Figure 134 the uncorrected flow curves from the ring compression test with the different ring heights are shown. For the rings with an initial height of 3 mm, buckling of the ring is detected in the compression test, so that these flow curves cannot, of course, be used for further purposes. In the case of the rings with an initial height of 2 mm, buckling is not observed and degrees of deformation up to approx. 0.35 are achieved.

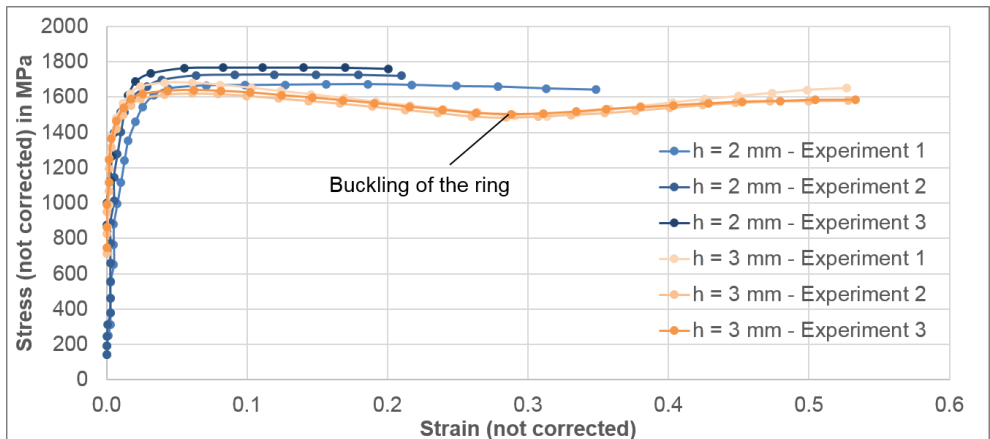


Figure 134: Flow curves (not corrected) from ring compression test with different ring heights of the rivet material with hardness class H4

Figure 135 flow curves from the tensile test of the base material are compared with the compression tests of the rings from the manufactured rivets. Due to the differences of the tested materials, a real comparability is not given, because batch fluctuations also play a role.

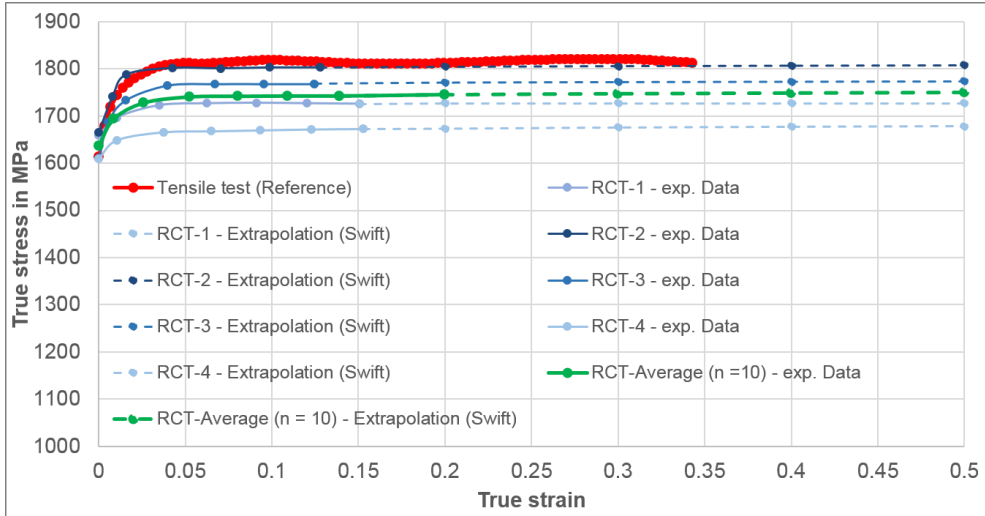


Figure 135: Comparison of the flow curves from the bar tensile test of the base material and the ring compression test for the rivet material for hardness class 4

In the investigations carried out here, the flow curves from the compression tests are slightly below the flow curve from the tensile test. Significant differences are found within the compression tests, which may be related to the strength fluctuations of the rivets. In the further numerical investigations for the SPR process, the average flow curve from the ring compression tests is used.

### 13 Numerical assessment of flow curves

In the following numerical investigations the in chapter 6 described simulation models and in chapter 11 shown flow curves are used to compare the simulated joining process results to the experimental results from chapter 5. For each material the individual differences from the flow curve determination methods and their influence on the numerically calculated joining result will be analysed.

#### 13.1 Flow curve comparison for self-pierce riveting

In Figure 136 a comparison of the simulated and experimental results in terms of contour, force-displacement curve and characteristics of the joint for the SPR process of DC04 in DC04 is shown.

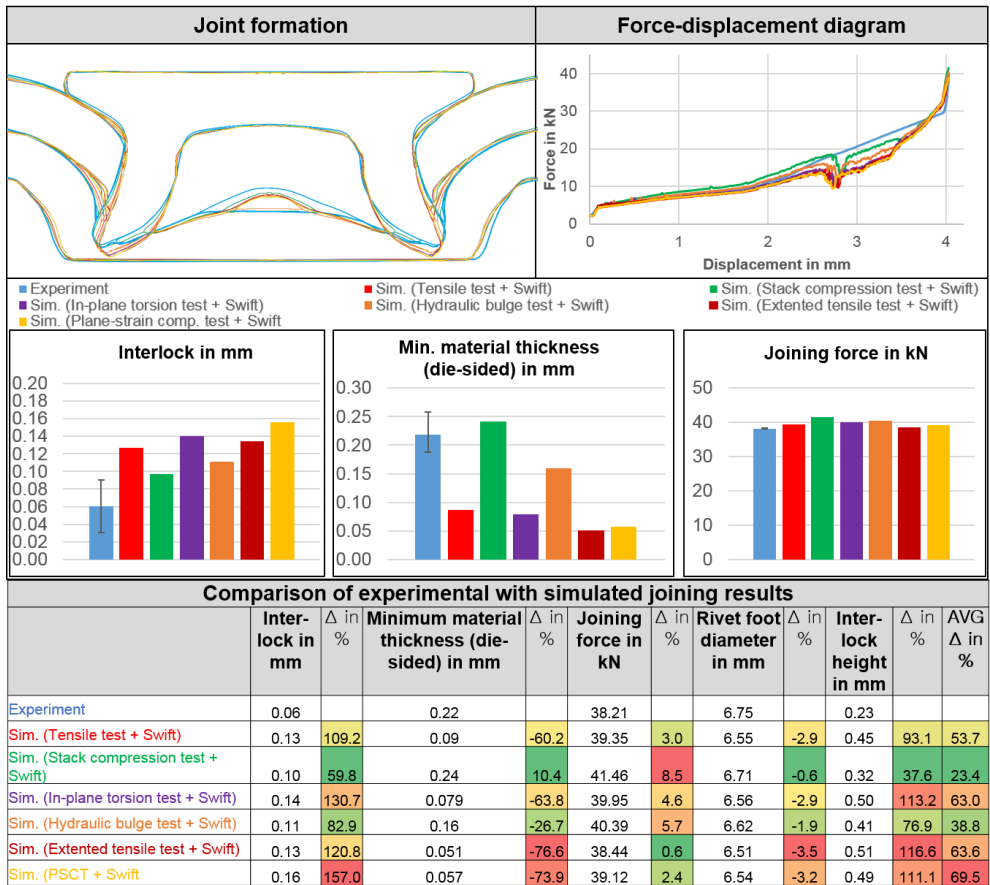


Figure 136: Comparison of simulation results with different flow curves for SPR of DC04 ( $t = 1.0$  mm) in DC04 ( $t = 1.0$  mm)

Analogous to the flow curves of the different material tests (Figure 128), the results of the process simulation of the SPR process also show significant differences by using the respective flow curves. This concerns both the contour and the force curve. In general, all simulation

models overestimate the interlock, which in this case is probably due to the use of the geometric damage model. When comparing all simulation results with the different flow curves, the simulation with the flow curve from the SCT shows the best agreement with the experiment. Due to the slightly higher flow curve from the SCT, the SPR process simulation provides an improved representation of the expansion behaviour of the rivet and thus a good prognosis of the material thickness below the rivet foot.

This result is in good agreement with the results of the stress analysis, since the materials are predominantly stressed in the compressive stress range in both the compression test and the SPR process.

In Figure 137 a comparison of the simulated and experimental results in terms of contour, force-displacement curve and characteristics of the joint for the SPR process of EN AW-5182 in EN AW-5182 is shown.

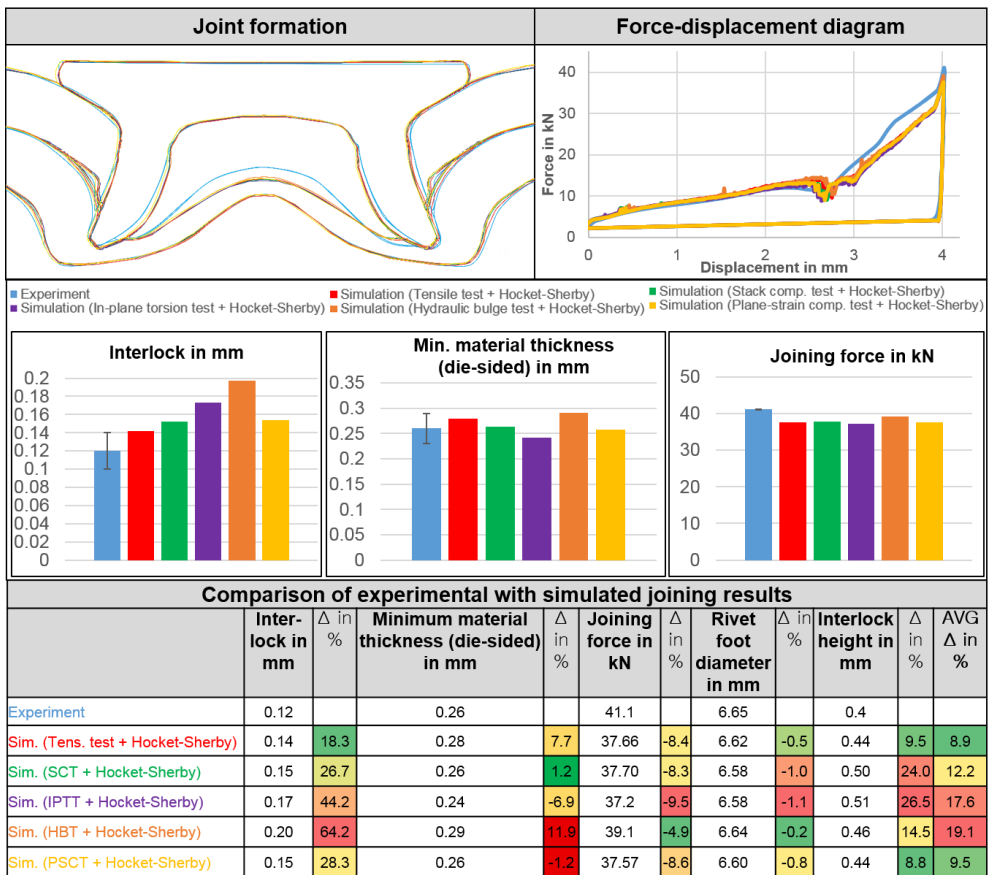


Figure 137: Comparison of simulation results with different flow curves for SPR of EN AW-5182 ( $t = 1.1$  mm) in EN AW-5182 ( $t = 1.1$  mm)

The results of the flow curve determination of the different material tests are also reflected here. Compared to the DC04 joint, the differences in contour and force progression are significantly smaller. Due to the differences in the area of the interlock, the most significant differences are found in interlock dimension. All in all, the influence of the material test on the

flow curve determination for this material combination is relatively small. With all methods considered, the joining experiment can be well represented in the simulation.

Comparable statements apply to the numerical results of the SPR simulations of the material combination CR330Y590 in EN-AW 5182 (Attachment 1) and EN AW-6082 T6 in EN AW-6082 T6 (Attachment 2).

### 13.2 Flow curve comparison for clinching

In Figure 138 the comparison of the simulated and experimental results in terms of contour, force-displacement curve and characteristics of the joint for the clinching process of DC04 in DC04 is shown.



Figure 138: Comparison of simulation results with different flow curves for Clinching of DC04 ( $t = 1.0$  mm) in DC04 ( $t = 1.0$  mm)

When clinching the material combination DC04 in DC04, it is not possible to detect such large differences with regard to the contour as with the SPR process. This is probably due to the additional rivet element at SPR. However, the differences between the simulations of the different material tests can be seen in the force progression. Here, the level of the process forces is analogous to the level of the determined flow curves for the DC04. Especially the simulation model with the flow curve from the SCT shows a good agreement with the experiment. With

regard to the geometric characteristics, all simulation models show good comparability with the experimental values. However, the simulation model with the flow curve from the SCT again shows on average the smallest deviation from the experimental values.

Figure 139 shows the comparison of experimental and numerical results for clinching of the two sheet combination with EN AW-5182.

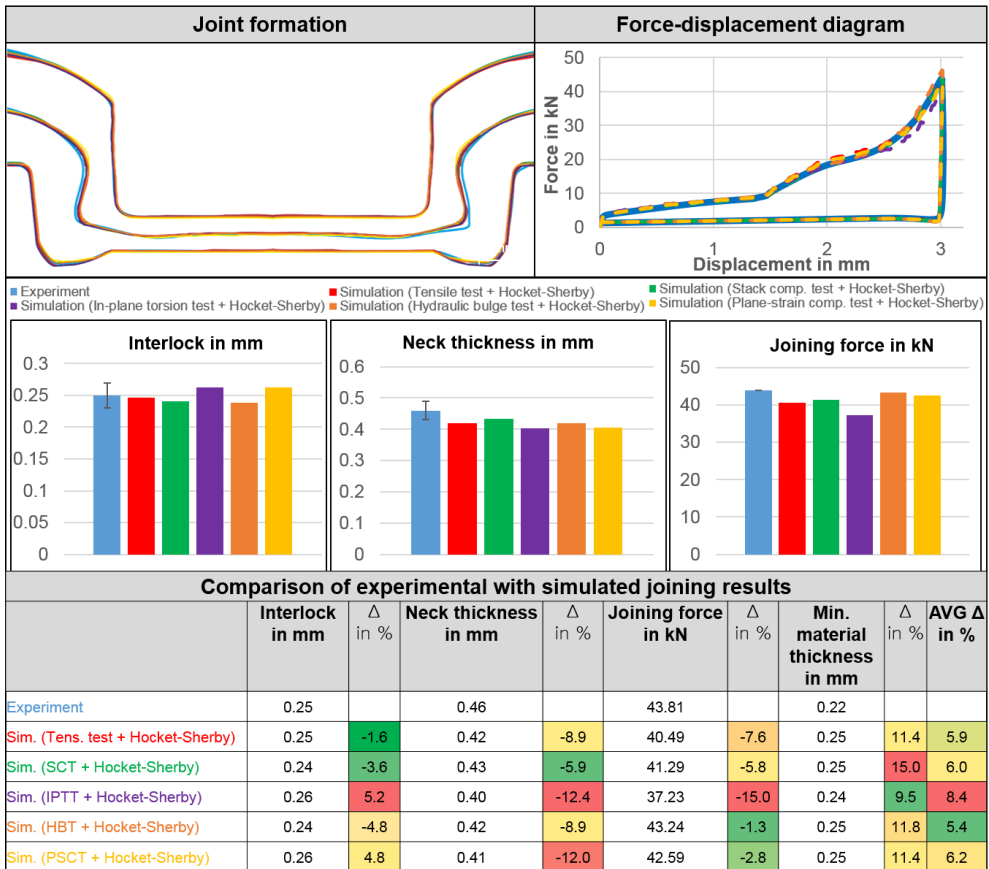


Figure 139: Comparison of simulation results with different flow curves for Clinching of EN AW-5182 ( $t = 1.1$  mm) in EN AW-5182 ( $t = 1.1$  mm)

Similar to the SPR results and analogous to the flow curves, the differences here are smaller, also in the influence on the process forces. Overall, all simulation models show a good comparability to the experiment. The results of the clinching simulations of the material combination CR330Y590 in EN-AW 5182 (Attachment 3) and EN AW-6082 T6 in EN AW-6082 T6 (Attachment 4) are comparable to the results of Figure 139.

## 14 Recommendations for flow curve determination for mechanical joining

**Fehler! Verweisquelle konnte nicht gefunden werden.** shows a flowchart that guides the selection for large strain flow curve identification in joining by forming. The selection is material –and process–informed. The first step in the selection is based on the degree of plastic anisotropy of the base material. If the plastically anisotropy of the material under investigation is weak, the material is assumed to be plastically isotropic. In that case, any material test enabling to probe large plastic strains is fine. In this regard, a lower limit of a true plastic strain of 0.5 is suggested. Some material tests are of limited usefulness depending on the ductility of the material. Therefore, an additional selection is based on the strain at maximum uniform strain. The PNTE, for example, requires clear occurrence of diffuse necking during the tensile test. The HBT is often conducted with the aid of a draw bead which requires sufficient ductility to form the draw bead. An additional selection attribute is the Size of the test sample. When only a small amount of material is available for testing, a small scale test such as the SCT might be preferable.

If the material, however, exhibits significant plastic anisotropy it is recommended to conduct a stress state analysis and extract the dominating stress state ( $\eta_{avg}$ ,  $\omega_{avg}$ ) to select the most appropriate material test. The following indicators of plastic anisotropy are suggested:

- Normal Anisotropy  $\bar{R} \gg 1$  indicating that i) the yield locus is stretched in the equibiaxial direction and ii) the material is stronger in the through-thickness direction;
- For steels: The average r-value  $r_{avg} > 1.5$  indicating that differential working hardening for equibiaxial tension is significant.

Once the large strain flow curve is obtained, it is recommended to select the most appropriate hardening law. This can be done by curve fitting using the experimentally acquired data beyond the point of maximum uniform strain. If a proper hardening law is found for a certain material, it might be of interest to simplify the testing procedure and return to the extrapolation of a simple tensile test.

In this project, DC04 is the only material that exhibits significant plastic anisotropy. For both the considered clinching and SPR processes, the stress state analysis led to the selection of the SCT as most appropriate material test. Given that the final stages of both joining processes are characterised by forging of the material, the result of the stress state analysis is line the engineering judgment or intuition. This is, however, not a general rule. Stress state analysis of clinching EN AW-6082 T6 in EN AW-6082 T6 revealed a shear-dominated stress state. Because EN AW-6082 T6 can be assumed plastically isotropic, however, the stress state analysis was not required. It is recommended to perform the stress state analysis for each joining case when dealing with anisotropic materials

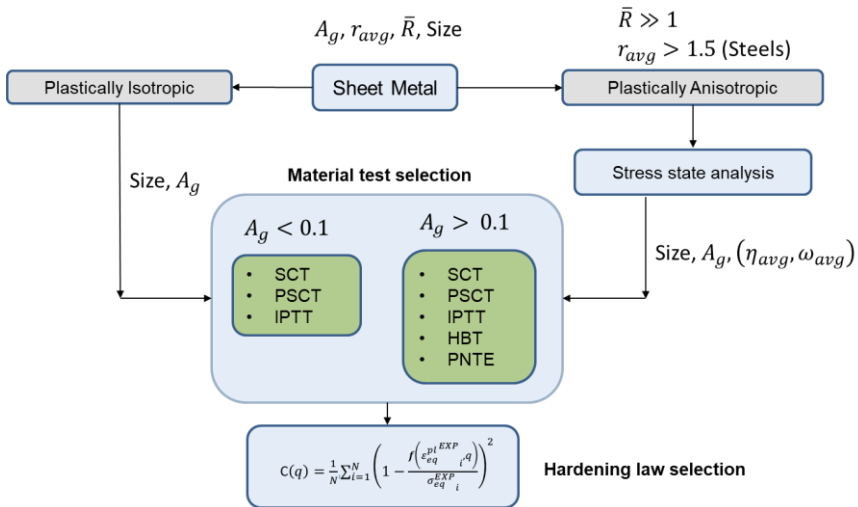


Figure 140 Flowchart process -and material-informed material test selection for flow curve determination in joining by forming.

---

## 15 Summary

In the here described project the flow curve determination for mechanical joining techniques like clinching and self-pierce riveting was investigated. Thereby a process-informed methodology for selecting the most appropriate material test for identifying the large strain flow curve of sheet metal was developed.

The selection procedure relies on a first order simulation for feeding the stress state analysis. The basic idea is to identify the dominating stress state in joining process. This information along with the average plastic strain is linked with the most appropriate material test for identifying the large strain flow curve. The methodology is applied and validated to the problem of clinch forming and self-pierce riveting. For plastically isotropic metals, the flow curve can be determined using any material test enabling to probe at least a true plastic strain of 0.5. If the material exhibits a diffuse neck, the extended tensile test is an industrially relevant material test. In terms of maximum attainable true plastic strain, the in-plane torsion test is superior to all other tests considered in this project.

For plastically anisotropic materials, the proposed selection strategy is proven to improve the simulation accuracy in joining by forming. DC04 exhibits significant plastic anisotropy. For clinching and self-pierce riveting DC04 in DC04, the process-informed selection method pointed in the direction of the stack compression test (SCT). It was experimentally validated that the SCT-flow curve indeed yields the most accurate simulation result thereby confirming the selection methodology proposed in this report.

Although the SCT gave the most accurate simulation results for the anisotropic material considered in this project, it must be noted that this conclusion is valid for the considered joining cases. For example, stress state analysis of clinching EN AW-6082 T6 in EN AW-6082 T6 resulted in a shear-dominated stress state. Given that EN AW-6082 T6 exhibits relatively weak plastic anisotropy, all considered material tests resulted in comparable flow curves. As such, we recommend to conduct a stress state analysis prior to select the material test to identify the large strain flow curve.

As opposed to all considered material tests, however, the SCT offers the possibility to be tailored with respect to a specific mechanical joining process. Indeed, it is shown that the stack configuration (i.e. the number of discs and the disc diameters) determines the stress state within the stack. As such, the configuration can be aligned with the requirements coming from the stress state analysis of the joining technique at hand.

To this end, the properties of the SCT were carefully examined with regard to individual optimization for mechanical joining. It is shown that a larger disc diameter increases the compressive stress component and thus an improved comparability to clinching and SPR is given. Furthermore, larger disc diameters have a positive effect on the robustness of the tests. In order to still achieve high degrees of deformation, very high press forces are required in some cases, depending on the material.

From a scientific point of view, an interesting observation was made during the optimization of the SCT for mechanical joining: the effect of the stack configuration on the flow curve turned out to be material depended. It was hypothesised that the hydrostatic pressure has an effect on the flow curve. This effect was most pronounced for the high strength steel (CR330590-DP) considered in this project. The difference in flow behaviour could be related to a hydrostatic pressure shift between the stress states.

## Dissemination plan

Dissemination plan			
During the project			
Time period	Activity	Objective	Done
Project start + 6 months	User committee meeting	Project progress and results	x
Project start + 12 months	User committee meeting	Project progress and results	x
Project start + 18 months	User committee meeting	Project progress and results	x
Project closure	User committee meeting	Final project results and conclusions	x
Project start + 12 months	Creation of a new website	Reaching a wide range of possible interested companies	
During the entire project	Visits of interested companies	Sensitisation of companies	x
2018, 2019	Workshop Simulation	Discuss results from the project	x
Dates not known yet	Publications in journals and periodicals.	Sensitisation of companies	x <sup>1</sup>
Dates not known yet	Reporting and feedback in EFB Working groups	Present results to EFB Members	x <sup>2</sup>
Dates not known yet	Presentation at seminars and colloquia	Results will be made available to the general public (e.g.: EFB-Kolloquium, ESAFORM, CIRP, Joining in car body manufacturing)	x <sup>3</sup>

x<sup>1</sup>: Large strain flow curve identification for joining by forming of sheet metal. Numiform 2018

x<sup>2</sup>: EFB Arbeitskreis Fügen 01-2019 and 01-2020.

x<sup>3</sup>: Large strain flow curve identification for sheet metal: Process-informed method selection. Forming Technology Forum 2019

<b>After the project</b>			
<b>Time period</b>	<b>Activity</b>	<b>Objective</b>	<b>Done</b>
Starting from project closure	General information through the BWI technology consultancy service	Increasing the awareness in the companies.	x
Dates not known yet	Publications in journals and periodicals.	Sensitisation of companies	x <sup>4, 5</sup>
Starting from project closure	Bilateral project: feasibility studies	Investigation of the feasibility of an industrial application	Planned for 3 <sup>rd</sup> quarter of 2020
Starting from project closure	Use of project results in educational activities	Dissemination of results to young engineers and increasing the awareness about the possibilities of the processes	x <sup>6</sup>
Starting from project closure	Annual report of the Fraunhofer IWU	Selected results will be published in the IWU's annual report	Planned for 4 <sup>th</sup> quarter of 2020
At project closure	Workshop: Determination of flow curves for mechanical joining	Dissemination of results to industry	Planned September 2020

x<sup>4</sup>: Process-oriented Flow Curve Determination at Mechanical joining. Esaform 2020

x<sup>5</sup>: Influence of a hydrostatic pressure shift on the flow stress in sheet metal. Esaform 2020

x<sup>6</sup>: Lecture: Overview of Current Challenges in Self-Pierce Riveting. HTW Dresden 05-2019

---

## List of Literature

- [ALV11] Alves, L.M, Nielsen, C. v., Martins, P.AF, 2011. Revisiting the Fundamentals and Capabilities of the Stack Compression Test. *Exp Mech*, vol. 51, 1565–1572.
- [AN05] An YG, Vegter H. Analytical and experimental study of frictional behavior in through-thickness compression test. *J Mater Process Technology* 2005;160:148-155.
- [AYD09] Aydin, M.-S.; Gerlach, J.; Keßler, L.: Verfahren zur Extrapolation der Fließkurve aus den Daten des Zugversuches jenseits der Gleichmaßdehnung. 8. LS-DYNA FORUM 2009, 12. November 2009, Filderstadt
- [BAI08] Bai Y., Wierzbicki, T.: A new model of metal plasticity and fracture w pressure and Lode dependence. *Int. J. Plas.* 24:1071-1096, 2008.
- [Beh16] Behrens B. et al. FEA of the clinching process of short fiber reinforced thermoplastic with an aluminum sheet using LS-DYNA. *Esaform* 2016, 27–29 April, Nantes, France
- [BON18] Bonora, N., Testa, G., Ruggiero, A., Iannitti, G., Gentile, D., 2018b. Modification of the Bonora Damage Model for shear failure. *Frattura ed Integrità Strutturale*, vol. 12, 140–150.
- [BRO11] Brosius, A.; Yin, Q.; Güner, A.; Tekkaya, A.E.: A New Shear Test for Sheet Metal Characterization. In *steel research international* 82 (2011) No. 4, DOI: 10.1002/srin.201000163
- [BRU14] Bruschi, S., Altan, T., Banabic, D., Bariani, P.F, Brosius, A., Cao, J., Ghiotti, A., Khra-isheh, M., Merklein, M., Tekkaya, A.E, 2014. Testing and modelling of material behaviour and formability in sheet metal forming. *CIRP Annals*, vol. 63, 727–749.
- [BUL99] Bulatov VV, Richmond O, Glazov MV. An atomistic dislocation mechanism of pressure-dependent plastic flow in aluminium. *Acta Mater* 1999; 47: 3507-3514
- [Bus11] Busse S. et al. Numerical and experimental investigations of an innovative clinching process. *Proc Techn of Plast*, 2011: 736–741.
- [CAM14] Campos, H.; Santos, A.D.; Martins, B.; Ito, K.; Mori, N.; Barlat, F.: Hydraulic bulge test for stress-strain curve determination and damage calibration for Ito-Goya model. 11th. World Congress on Computational Mechanics (WCCM XI), 20-25 July 2014 Barcelona
- [CAM14] Campos, H., Santos, A.D, Martins, B., Ito, K., Mori, N., Barlat, F., 2014. Hydraulic bulge test for stress-strain curve. Determination and damage calibration for ITO-GOYA model.
- [CHE20] Chermette, C., Unruh, K., Peshekhodov, I. et al. A new analytical method for determination of the flow curve for high-strength sheet steels using the plane strain compression test. *Int J Mater Form* 13, 269–292 (2020)
- [CO12] Coppieters, S., Numerical and Experimental study of clinched joints, PhD thesis, KU Leuven, 2012.
- [COP10] Coppieters, S.; Lava, P.; Sol, H.; Van Bael, A.; Van Houtte, P.; Debruyne, D.: Determination of flow stress and contact friction of sheet-metal in a multi-layered upsetting test. *Journal of Materials Processing Technology* 210 (2010) 1290 - 1296
- [COP10] Coppieters, S., Lava, P., Sol, H., van Bael, A., van Houtte, P., Debruyne, D., 2010. Determination of the flow stress and contact friction of sheet metal in a multi-layered upsetting test. *Journal of Materials Processing Technology*, vol. 210, 1290–1296

- 
- [COP11] Coppieters S., Cooreman S., Soly H., Van Houtte P., Debruyne D. (2011). Identification of the post-necking hardening behaviour of sheet metal by comparison of the internal and external work in the necking zone. *Journal of Materials Processing Technology*, 211 (3), 545-552.
- [COP12] Coppieters S., Lava P., Baes S., Sol H., Van Houtte P., Debruyne D. (2012). Analytical method to predict the pull-out strength of clinched connections. *Thin-Walled Structures*, 52, 42-52.
- [COP14a] Coppieters S., Cooreman S., Debruyne D., Kuwabara T. (2014). Advances in post-necking flow curve identification of sheet metal through standard tensile testing. *AIP Conf. Proc.*: Vol. 1567. Numisheet. Melbourne, 6-10 January 2014 (pp. 632-636). Belgium: AIP Conf. Proc..
- [COP14b] Coppieters, S.; Ichikawa, K.; Kuwabara, T.: Identifikation of strain hardening phenomena in sheet metal at large plastic strains. 11th International Conference on Technology of Plasticity, ICTP 2014, 19-24 October 2014, Nagoya Congress Center, Japan
- [COP14c] Coppieters S., Kuwabara T. (2014). Identification of Post-Necking Hardening Phenomena in Ductile Sheet Metal. *Experimental Mechanics* (54), 1355-1371.
- [COP18] Coppieters, S., Hakoyama, T., Eyckens, P., Nakano, H., Van Bael, A., Debruyne, D., Kuwabara, T. (2018). On the synergy between physical and virtual sheet metal testing: calibration of anisotropic yield functions using a microstructure-based plasticity model. *International Journal of Material Forming*, 12, 741-759. doi: 10.1007/s12289-018-1444-1
- [DEN16] Denys K., Coppieters S., Seefeldt M., Debruyne D. (2016). Multi-DIC setup for the identification of a 3D anisotropic yield surface of thick high strength steel using a double perforated specimen. *Mechanics of Materials*, 100, 96-108.
- [DIE87] Dieter GE. *Mechanical Metallurgy*. McGraw-Hill Book Company, 1987, London.
- [DIN14] *Metallic materials – Sheet and strip – Determination of biaxial stress-strain curve by means of bulge test with optical measuring systems*. (ISO 16808:2014); German version EN ISO 16808:2014
- [DIN16] *Testing of metallic materials – Compression test at room temperature*, DIN 50106:2016-11
- [DIN17] *Metallic materials – Tensile testing – Part 1: Method of test at room temperature* (ISO 6892-1:2016); German version EN ISO 6892-1:2017-2
- [DRO13] Drossel, W.-G.; Israel, M.: *Sensitivitätsanalyse und Robustheitsbewertung beim mechanischen Fügen*, EFB-Forschungsbericht Nr. 376, Europäische Forschungsgesellschaft für Blechverarbeitung e. V., ISBN 978-3-86776-419-3, Hannover, 2013
- [DRU52] Drucker DC, Prager W. *Soil mechanics and plastic analysis of limit design*. *Q Appl Math* 1952;10: 157-165
- [DVS2012] DVS Gemeinschaftsausschuss „Mechanisches Fügen“: *DVS/EFB Merkblatt 3420 Clinchen - Überblick*. Düsseldorf: DVS, 2012
- [DVS2014] DVS Gemeinschaftsausschuss „Mechanisches Fügen“: *DVS/EFB Merkblatt 3410 Stanznieten - Überblick*. Düsseldorf: DVS, 2014
- [ECK09] Eckstein, J.: *Numerische und experimentelle Erweiterung der Verfahrensgrenzen beim Halbhohlstanznietenhochfester Bleche*. Universität Stuttgart, Diss. 2009
- [Fal19] Falk T., Jäckel M. Increasing flexibility of self-pierce riveting using numerical and statistical methods. *Procedia Manufacturing*, 2019; 29: 264–270.

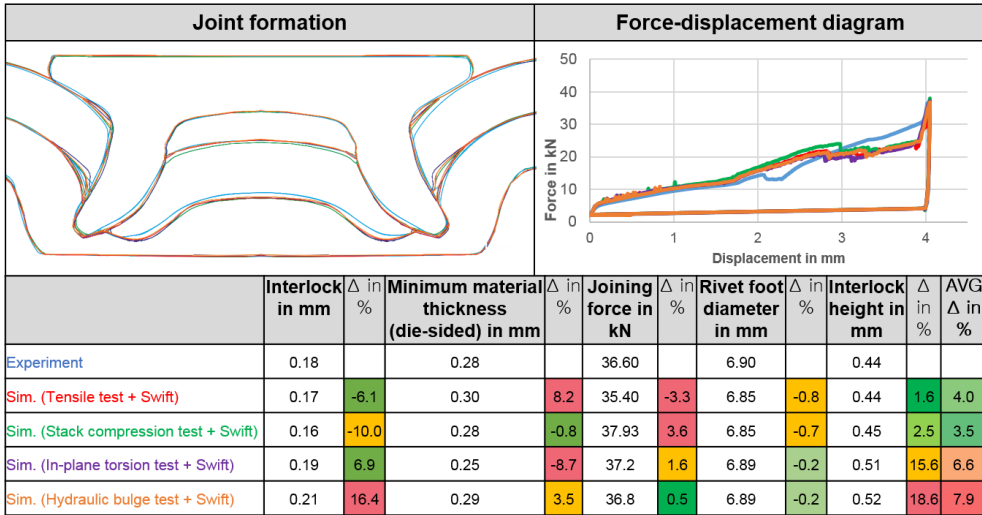
- [GEL14] Gelin JC, Ghouati O, Shahani R (1994) Modelling the plane strain compression test to obtain constitutive equations of aluminium alloys. *Int J Mech Sci* 36(9):773–796
- [HA20] J. Ha, S. Coppieters, Y. Korkolis, On the expansion of a circular hole in an orthotropic elastoplastic thin sheet, *international journal of mechanical sciences*, accepted for publication, April 2020
- [Hah01] Hahn, O. & Dölle, N., 2001. Numerische Simulation des Fügeprozesses beim Stanznieten mit Halbhohlmetall von duktilen Blechwerkstoffen, Aachen: Shaker.
- [HAH03] Hahn, O.; Schmidt, L.: PC-gestützte Auswahl, Auslegung und Dimensionierung von Clinchwerkzeugen. EFB-Forschungsbericht Nr. 201, Europäische Forschungsgesellschaft für Blechverarbeitung, ISBN 978-3-86776-157-4, Hannover 2003
- [HAK19] T. Hakoyama, S. Coppieters, T. Kuwabara, Effect of Strain Rate on Determining Post-necking Work Hardening of a Low-carbon Steel Sheet, *Proceedings NUMIFORM 2019*
- [HAN02] Han H. The validity of mechanical models evaluated by two-specimen method under the unknown coefficient of friction and flow stress. *J Mater Process Technol* 2002;122:386-396.
- [HAR17] S. Hartel, M. Graf, T. Gerstmann, B. Awiszus, Heat generation during mechanical joining processes- by the example of flat-clinching. *Procedia Engineering* 184 (2017) 251-265
- [HER10] Herzig, N.; Abdel-Malek, S.; Meyer, L. M.: Experimentelle Ermittlung und Modellierung dynamischer Fließortkurven an Blechwerkstoffen. 9. LS-DYNY Forum, Bamberg 2010
- [HÖN19] Hönsch F, Domitner J and Sommitsch C. Deformation behavior of high-strength steel rivets for self-piercing riveting applications. *Esaform 2019*, 8–10 May 2019, Vitoria-Gasteiz, Spain
- [IAD11] M.A. Iadicola, AIP conference proceedings, 1383, 742-749 (2011).
- [IND08] Projektpräsentation, IMU-GCFG 7, „Standardisierung der Fließkurvenaufnahme“, Industrieverband Massivumformung e.V., 03.09.2008
- [ISO 6892-1, 2009] Metallic materials - Tensile testing. Part 1: Method of test at room temperature, International Organization for Standardization, Genève.
- [KAI04] J. Kajberg, J.; Lindkvist, G.: Characterization of materials subjected to large plastic strains by inverse modelling based on in-plane displacement fields. *International Journal of Solids and Structures*, 41 (2004), pp. 3439-3459
- [KIM02] Kim, I.: Einfluss des Spannungszustandes während des hydraulischen Tiefungsversuchs auf das Umformverhalten von Blechwerkstoffen. Aachen: Shaker, 2002 (Berichte aus dem Institut für Eisenhüttenkunde ; Bd. 2002,9), ISBN 3-8322-0829-1
- [KIM13] J.-H. Kim, A. Serpantié, F. Barlat, F. Pierron, M.-G. Lee, Characterization of the post-necking hardening behavior using the virtual fields method, *Int. J. Solids Struct.* 50 (2013) 3829-3842
- [KNY17] Knysh, P., Korkolis, Y.P., 2017. Identification of the post-necking hardening response of rate- and temperature-dependent metals. *Int. J. Solids Struct.* 115–116. <https://doi.org/10.1016/j.ijsolstr.2017.03.012>
- [KOC76] U.F. Kocks (1976), *J. Eng. Mater. Technol. ASME Series H*, 98, 76

- 
- [LAR10] Larour, P.: Strain rate sensitivity of automotive sheet steels: influence of plastic strain, strain rate, temperature, microstructure, bake hardening and pre-strain. Diss. RWTH Aachen, in *Berichte aus dem Institut für Eisenhüttenkunde*, Bd. 1/2010, Shaker Verlag, Aachen
- [MAE18] Maeda T, Noma N, Kuwabara T, Barlat F, Korkolis YP. Measurement of the strength differential effect of DP980 steel sheet and experimental validation using pure bending test. *J Mater Process Technol* 2018; 265: 247-253.
- [MAR02] Marciniak, Z., Duncan, J.L., Hu, S.J., 2002. *Mechanics of Sheet Metal Forming*, Butterworth-Heinemann.
- [MAR17] Martínez, A., v. Miguel, Coello, J., Manjabacas, M.C, 2017. Determining stress distribution by tension and by compression applied to steel: Special analysis for TRIP steel sheets. *Materials & Design*, vol. 125, 11–25.
- [MEC16] CORNET project Mechanical Joining of Materials with Limited Ductility
- [MER09] Merklein, M., Kuppert, A., 2009. A method for the layer compression test considering the anisotropic material behavior. *Int J Mater Form*, vol. 2, 483–486.
- [MIN17] Min, J., Stoughton, T.B, Carsley, J.E, Carlson, B.E, Lin, J., Gao, X., 2017. Accurate characterization of biaxial stress-strain response of sheet metal from bulge testing. *International Journal of Plasticity*, vol. 94, 192–213.
- [MUE01] Mülders, B.: *Modellierung der Verfestigung technischer Aluminiumlegierungen*. Dissertation RWTH Aachen, 2001
- [MUL15] Mulder J, Vegter H, van den Boogaard AH. An engineering approach to strain rate and temperature compensation of the flow stress established by the hydraulic bulge test. *KEY ENG MATER* 2015;651-653:138-143.
- [MUL15a] Mulder J, Vegter H, Aretz H, Keller S, van den Boogaard AH. Accurate determination of flow curves using the bulge test with optical measuring systems. *J Mater Proc Technol* 2015; 226:169–187.
- [NEU10] Neugebauer, R.; Müller, R.; Gumbsch, P.; Butz, A.: *Beurteilung der Leistungsfähigkeit von Materialmodellen für die Blechumformsimulation*. EFB-Forschungsbericht Nr. 314, Europäische Forschungsgesellschaft für Blechverarbeitung, ISBN 978-3-86776-350-9, Hannover 2010
- [POU20] Poulin, C.M., Barrett, T.J., Knezevic, M., 2020. Inferring Post-Necking Strain Hardening Behavior of Sheets by a Combination of Continuous Bending Under Tension Testing and Finite Element Modeling. *Exp. Mech.* <https://doi.org/10.1007/s11340-019-00577->
- [REE12] Rees, D.WA, 2012. Plane strain compression of aluminium alloy sheets. *Materials & Design*, vol. 39, 495–503.
- [RIC80] Richmond O, Spitzig WA. Pressure dependence and dilatancy of plastic flow. *IUTAM Conference, Theoretical and Applied Mechanics, Proc. 15<sup>th</sup> International Congress on Theoretical and Applied Mechanics* 1980;377-386.
- [ROW77] Rowe, G.W, 1977. *Principles of Industrial Metalworking Processes*, Edward Arnold, London.
- [SAB08] Saberi, S., Enzinger, N., Vallant, R., Cerjak, H., Hinterdorfer, J., Rauch, R., Influence of plastic anisotropy on the mechanical behaviour of clinched joint of different coated thin steel. *International Journal of Materials Forming* Suppl.1 (2008) 273-276.

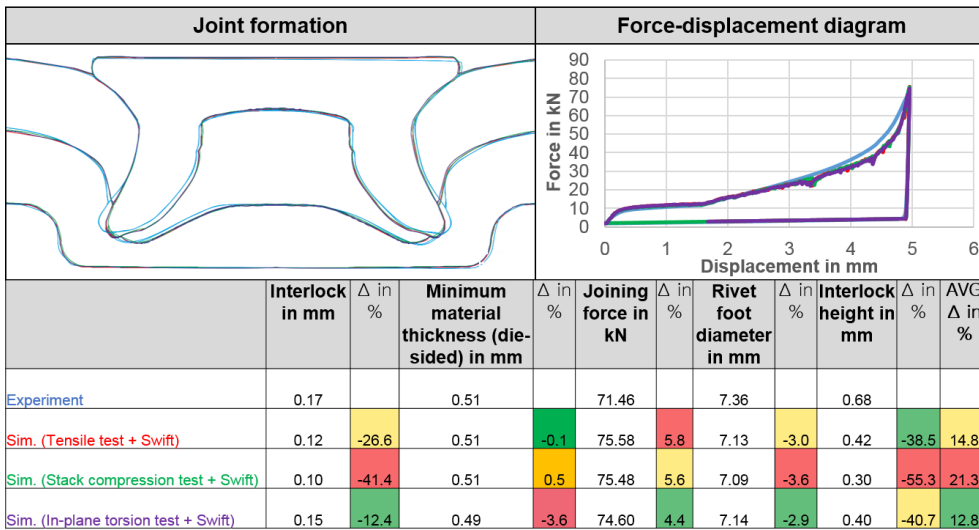
- [SEV80] J.G. Sevillano, P. Van Houtte, E. Aernoudt, Large strain work hardening and textures, *Progress in Materials Science*, Vol.25, pp 69-412, 1980
- [SHI17] Shirakami S, Kuwabara T, Tsuru E. Axial compressive deformation behavior and material modelling of steel pipe with bending deformation history. *J JSTP* 2017; 58: 692-698 (in Japanese).
- [SPI75] [Spitzig WA, Sober RJ, Richmond O. Pressure Dependence of yielding and associated volume expansion in tempered martensite. *Acta Metall* 1975; 23:885-893.
- [SPI84] Spitzig WA, Richmond O. The effect of pressure on the flow stress on metals. *Acta Metall* 1984;32:457-463.
- [STE14] Steglich D, Tian X, Bohlen J, Kuwabara T. Mechanical testing of thin sheet magnesium alloys in biaxial tension and uniaxial compression. *Exp Mech* 2014; 54:1447-1258.
- [SU15] Z.-M. Su, P.-C. Lin, W.-J. Lai, J. Pan, Fatigue analysis of self-piercing rivets and clinch joints in lap-shear specimens of aluminum sheets, *International Journal of Fatigue* 72 (2015) 53{65.
- [TAR12] Tardif, N., Kyriakides, S., 2012. Determination of anisotropy and material hardening for aluminum sheet metal, in: *International Journal of Solids and Structures*. Pergamon, pp. 3496–3506. <https://doi.org/10.1016/j.ijsolstr.2012.01.011>
- [TEK82] Tekkaya, A.E, Pöhlandt, K., Lange, K., 1982. Determining Stress-Strain Curves of Sheet Metal in the Plane Torsion Test. *CIRP Annals*, vol. 31, 171–174.
- [TOM02] Thoms, V.; Süße, D.: Methoden zur Kennwertermittlung für Blechwerkstoffe. EFB-Forschungsbericht 187, Europäische Forschungsgesellschaft für Blechverarbeitung e. V., ISBN 978-3-86776-087-4, Hannover, 2002
- [TRA18a] Traphöner, H., Clausmeyer, T., Tekkaya, A.E, 2018a. Material characterization for plane and curved sheets using the in-plane torsion test – An overview. *Journal of Materials Processing Technology*, vol. 257, 278–287.
- [TRA18b] Traphöner, H., Heibel, S., Clausmeyer, T., Tekkaya, A.E, 2018b. Influence of manufacturing processes on material characterization with the grooved in-plane torsion test. *International Journal of Mechanical Sciences*, 146-147, 544–555.
- [VAN16] Van de Velde, A., Coppieters, S., Denys, K., Maeyens, J., Debruyne, D., Reproducing the experimental torque-to-turn resistance of blind rivet nuts, *ESAFORM* 2016, accepted for publication.
- [VER11] Verleysen, Patricia, Jan Peirs, Joost Van Slyken, et al. "Effect of Strain Rate on the Forming Behaviour of Sheet Metals." *JOURNAL OF MATERIALS PROCESSING TECHNOLOGY* 211.8 (2011): 1457–1464. Print.
- [VOC48] E. Voce (1948) *J. Inst. Met.*, 74, 537
- [YAB14] Yabe, S., Terano, M., Yoshino, M., 2014. Plane Strain Compression Test and Simple Shear Test of Single Crystal Pure Iron. *Procedia Engineering*, vol. 81, 1342–1347.

- 
- [YAN12] Yanagaa, D., Kuwabarab, T., Uemac, N., Asanoc, M.: Material modeling of 6000 series aluminum alloy sheets with different density cube textures and effect on the accuracy of finite element simulation. *International Journal of Solids and Structures*, ISSN: 0020-7683, Vol: 49, Issue: 25, Page: 3488-3495. 2012
- [YIN14] Yin, Q.: *Verfestigungs- und Schädigungsverhalten von Blechwerkstoffen im ebenen Torsionsversuch*. D290 (Diss. Technische Universität Dortmund), ISBN 978-3-8440-2839-3, Shaker Verlag Aachen 2014
- [YIN14] Yin, Q., Zillmann, B., Suttner, S., Gerstein, G., Biasutti, M., Tekkaya, A.E, Wagner, M.F-X, Merklein, M., Schaper, M., Halle, T., Brosius, A., 2014. An experimental and numerical investigation of different shear test configurations for sheet metal characterization. *International Journal of Solids and Structures*, vol. 51, 1066–1074.
- [YIN15] Yin, Q., Soyarslan, C., Isik, K., Tekkaya, A.E, 2015. A grooved in-plane torsion test for the investigation of shear fracture in sheet materials. *International Journal of Solids and Structures*, vol. 66, 121–132.
- [YOO04] Yoon JW, Barlat F, Dick RE, Chung K, Kang TJ (2004) Plane stress yield function for aluminum alloy sheets-part II: FE formulation and its implementation. *Int J Plast* 20:495–522
- [ZHA99] Z.L. Zhang, M. Hauge, J. Odegard, C. Thaulow, *International Journal of Solids and Structures*, 36 3497-3516 (1999).
- AN05 An YG, Vegter H. Analytical and experimental study of frictional behavior in through-thickness compression test. *J Mater Process Technology* 2005;160:148-155.

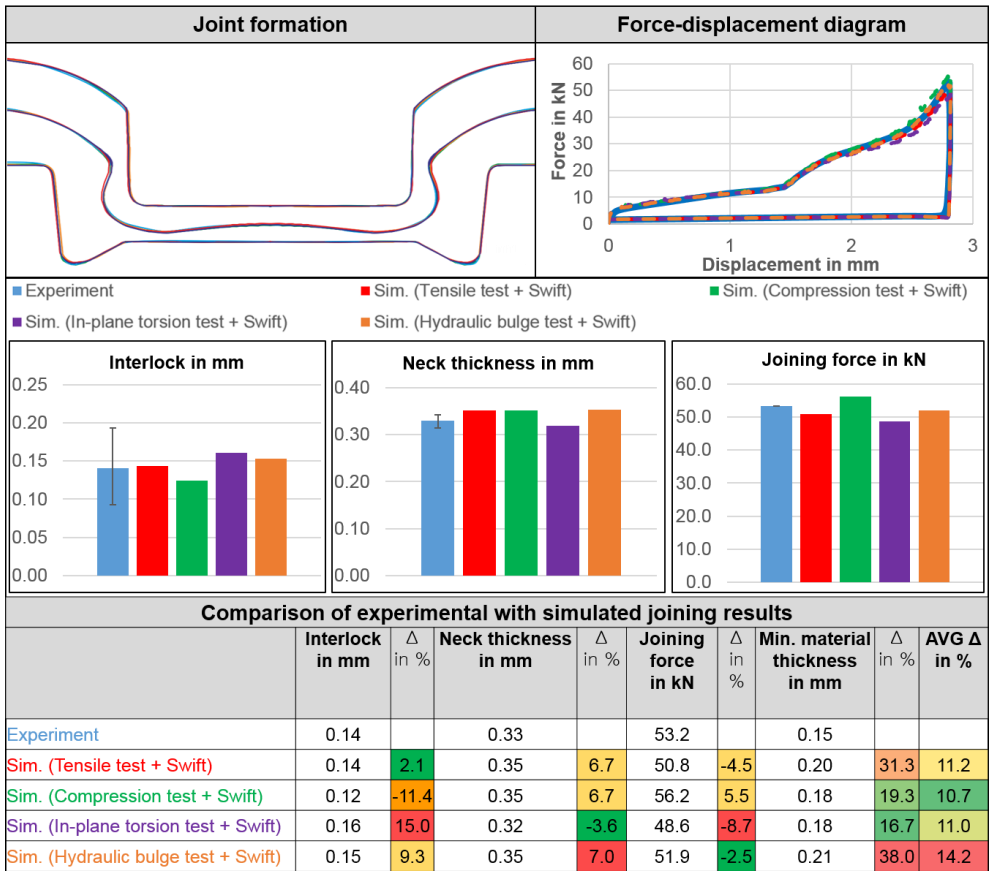
## Attachments



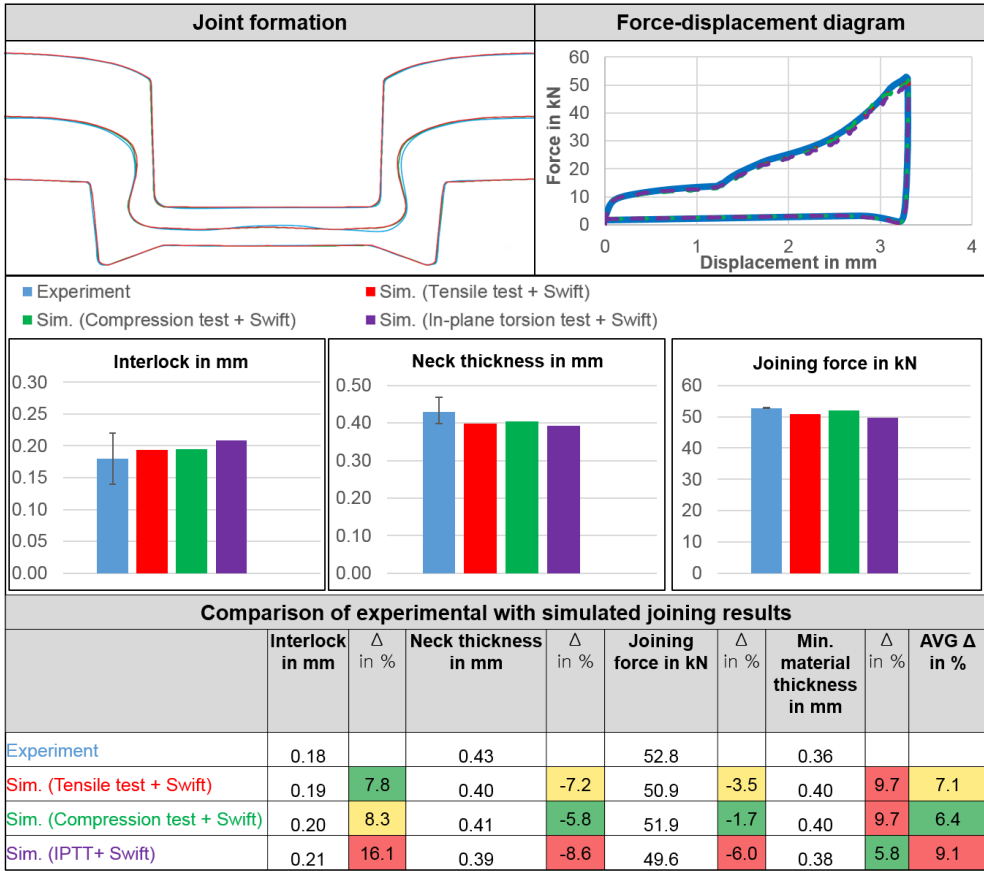
Attachment 1: Comparison of simulation results with different flow curves for SPR of CR330Y590-DP ( $t = 1.0$  mm) in EN AW-5182 ( $t = 1.1$  mm)



Attachment 2: Comparison of simulation results with different flow curves for SPR of EN AW-6082 T6 ( $t = 1.5$  mm) in EN AW-6082 T6 ( $t = 1.5$  mm)



Attachment 3: Comparison of simulation results with different flow curves for Clinching of CR330Y590-DP ( $t = 1.0$  mm) in EN AW-5182 ( $t = 1.1$  mm)



Attachment 4: Comparison of simulation results with different flow curves for Clinching of EN AW 6082 T6 ( $t = 1.5$  mm) in EN AW 6082 T6 ( $t = 1.5$  mm)